UNVEILING EARTHQUAKE LEGACY EFFECTS ON HILLSLOPES USING InSAR

NITHESHNIRMAL SADHASIVAM

August 2022

SUPERVISORS:
Dr. Ling Chang
Dr. Hakan Tanyaș

ADVISOR:
Prof.Dr. Cees Van Westen

THESIS ASSESSMENT BOARD:
Prof.Dr.Ir. Alfred Stein (Chair)
Dr. Mario Floris (External Examiner, University of Padua)

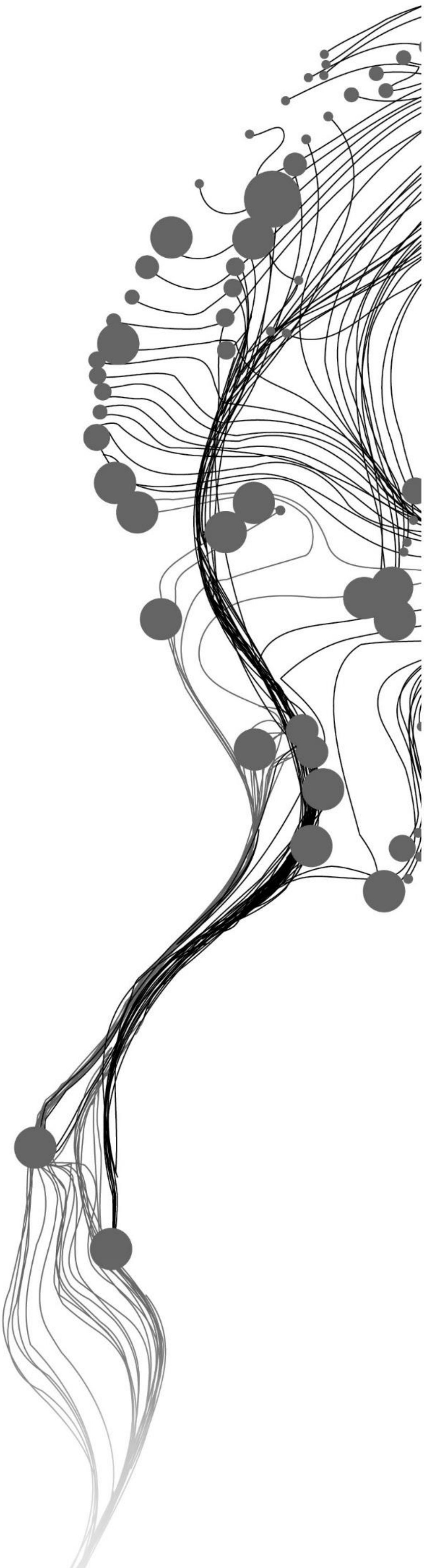

UNVEILING EARTHQUAKE LEGACY EFFECTS ON HILLSLOPES USING InSAR

NITHESHNIRMAL SADHASIVAM
Enschede, The Netherlands, AUGUST 2022

Thesis submitted to the Faculty of Geo-Information Science and Earth Observation of the University of Twente in partial fulfilment of the requirements for the degree of Master of Science in Geo-information Science and Earth Observation.

Specialization: Natural Hazards and Disaster Risk Reduction

SUPERVISORS:
Dr. Ling Chang
Dr. Hakan Tanyaș

ADVISOR:
Prof.Dr. Cees Van Westen

THESIS ASSESSMENT BOARD:
Prof.Dr.Ir. Alfred Stein (Chair)
Dr. Mario Floris (External Examiner, University of Padua)

This work is dedicated to M. Kamaraj
A loving father and uncle who wasn't here to witness the completion of this study.

Wherever you are in those stars.

ABSTRACT

Landslides, driven by seismic activities, have caused numerous fatalities and huge socio-economic losses globally. Many studies have suggested that intense seismic shaking not only triggers landslides co-seismically but also amplifies the post-seismic landslide activity, which is likely due to the decrease in shear strength of slope materials and/or disturbed hillslope geometry/hydrology. As a consequence, an elevated landslide susceptibility is observed in post-seismic periods. This practically means that a rainfall event with a given intensity and duration that does not trigger any landslides in pre-seismic periods becomes more effective after an earthquake and triggers landslides, which could be expressed as an increase in overall landslide susceptibility level of a given landscape. This concept is defined as earthquake legacy effect, which has been largely investigated merely by mapping inventories of rapidly failed slopes during the post-seismic phase. However, the increased post-seismic landslide activity has not been investigated in terms of deformation rates of slow-moving hillslopes, which exhibit for instance, millimeter-level deformation rate over time. In addition, understanding the evolution of hillslopes affected by intense seismic shaking helps to better evaluate post-seismic hazards and risks, as well as plan management and mitigation measures.

This study aims to develop a novel systematic approach for detecting extremely slow-moving and very slow-moving hillslopes before and after the 2016 Mw 7.8 Kaikōura earthquake and monitoring their sub-meter evolution. In this research, I used freely available C-band Sentinel-1 Single Look Complex (SLC) Interferometric Wide (IW) mode dataset having a spatial resolution 5×20 m and polarisation of VV for Synthetic Aperture Radar Interferometry (InSAR) processing and deformation measurements extraction. Specifically, I examined 27 Sentinel-1 SAR scenes sensed before the earthquake and 63 images sensed following the event separately for extracting the deformation measurements in an area of about 2300 km2 using Persistent Scatterer Interferometry (PSI) approach. The analysis period of pre-Kaikōura phase is between 28 October 2014 and 10 November 2016, while the time window of post-earthquake phase is right after the earthquake mainshock from 16 November 2016 till 24 December 2018. A critical stability threshold value of ± 10 mm/yr is defined on the extracted line-of-sight deformation velocity (VLOS) to detect active PS, which is further categorised into extremely slow-moving (± 10 mm/yr $\geqslant$ VLOS $<$ ± 16 mm/yr) and very slow-moving (VLOS $\geqslant$ $\pm$ 16 mm/yr) hillslopes. Also, for the first time, I used Slope Units (SUs), which are terrain partitions associated with similar hydrological and geomorphological conditions, for the aggregation of active PS to identify extremely slow-moving and very slow-moving hillslopes. I then explored the dataset further and proposed a hillslope activity matrix for understanding the hillslope evolution after the impact of 2016 Kaikōura earthquake. Ultimately, I examined each category I defined in the proposed matrix via corresponding deformation time series in relation to daily precipitation.

The results shows that in general there is an 130% absolute increase in the mean LOS deformation velocity during the post-Kaikōura phase compared to its pre-seismic counterpart. The regions that experienced higher ground shaking during the 2016 Kaikōura earthquake are observed to have larger deformations during the post-seismic period. In addition, most of the large negative deformations are observed to be associated with hillslope processes while high positive deformations are largely linked to the fluvial processes happening the study area. Comparing the pre-Kaikōura phase, there is a significant increase in the very slow-moving hillslopes, which chiefly concentrate around the rupture zone.

Overall, I captured nine and 141 extremely slow-moving hillslopes during pre- and post- seismic phases, respectively. During the post- seismic phase I also identified 102 hillslopes showing very slow-movement. Based on these observations, this study proposed a hillslope activity matrix pointing out four hillslope evolution types: (i) inactive hillslope becoming active (Type I: SA), (ii) active hillslope remaining unaffected with changes in dynamics (Type II: AA), (iii) active hillslope that have become inactive (Type III: AS) and (iv) those hillslopes that are stable prior and following the earthquake (Type IV: SS). The hillslope activity matrix could be applied to other earthquake-affected areas to systematically and consistently examine hillslope evolution processes in post-seismic periods.

Keywords: Earthquake legacy effect, hillslope evolution, InSAR, actively deforming hillslopes, Sentinel-1, Persistent Scatterer Interferometry, hillslope activity matrix.

ACKNOWLEDGEMENTS

This work is not complete without acknowledging all those who guided, helped, and supported me throughout this whole period of MSc research at ITC. This section is the easiest for me to write as everything came straight from the heart and doesn't necessarily require a revision.

First, I am fortunate to have two of the best researchers, Dr. Ling Chang and Dr. Hakan Tanyaş, as my supervisors, who constantly supported and mentored me during this entire MSc research period. Without your guidance and motivation, I could not have finished this study.

I still remember the time when I was searching for an MSc research idea and found the topic put forth by Ling, which got my interest (actually, it was a different title that eventually evolved to the current one). Thanks, Ling, for proposing such a fantastic research idea and guiding me throughout this phase. When I started this research, I had no idea if I could do it as I had no previous experience working with InSAR. But you were very supportive and kind towards me during this whole time. Taking your radar remote sensing course helped me immensely and improved my basic understanding of the subject. Your guidance and support on the InSAR part are invaluable, and I will be ever indebted. My invaluable thanks go to my second supervisor and excellent mentor, Dr. Hakan Tanyaş, for his innovative ideas, valuable critical comments, and feedback. Hakan, thanks for being my "daily" supervisor for the past couple of months. Your research ideas have helped me immensely in this work (such as your idea to work on earthquake-affected hillslopes). I hope our collaboration continues for a long time. Every time I talk to you, I felt more confident and optimistic about what I was doing. Thanks for being there to encourage and motivate me whenever I was not doing well. I am deeply indebted to you for all your support.

I would like to extend my gratitude to Professor Dr. Cees Van Westen, my advisor, for all his constructive comments and feedback that I got for this work. It's an honor to be your student. Your critical comments helped me in improving this work. My special thanks go to Dr. Luigi Lombardo, who incredibly motivated and supported me during this research phase. The credits for this wonderful research title which I have now for this work, go to you. I would also like to thank Dr. Islam Fadel for his tremendous support in introducing me to InSAR processing in CRIB.

The processing of Sentinel-1 images ere completely performed in the Geospatial Computing Platform of the Center of Expertise in Big Geodata Science (CRIB). I thank Dr. Serkan Girgin for all his support in providing the necessary computing infrastructure. ITC Excellence Scholarship made it possible for me to attend ITC, and I am very grateful to ITC Faculty.

I would like to express my gratitude to my buddies, Sahara Sedhain, Biman Biswas, Enzo Campomanes V, Lynette Dias, Binita Khanal, Sachita Shahi, and Diana Collazos Cortez from studio 5-036 of ITC for all of the beautiful moments we shared which I will cherish forever. Thanks, guys, for all the fun and enjoyment. Also, thanks to my friends, Sowmeya, Athithya, Abbas, Mahesh, Praneeth, and Darshana, for being my pillar of support and encouragement outside ITC.

I thank my family. I owe everything to you, mom and dad. I know you both will be delighted for me to get this degree. I also thank Nii's mom and brother for their support. Even though we don't interact much, you have always been there for me, my brother (Gokul).

Lastly, I have a very important person to acknowledge for everything so far in my life; thank you, Nivedita Priyadarshini (Nii), for always being my biggest supporter and motivator.

TABLE OF CONTENTS

LIST OF FIGURES

LIST OF TABLES

ACRONYMS

USD	United States Dollar
GPS	Global Positioning System
LIDAR	Light Detection and Ranging
SAR	Synthetic Aperture Radar
LOS	Line Of Sight
InSAR	SAR Interferometry
GB-InSAR	Ground-Based InSAR
D-InSAR	Differential InSAR
CPT	Coherence Pixel Technique
MT-InSAR	Multi-Temporal InSAR
PSI	Persistent Scatterer Interferometry
IPTA	Interferometric Point Target Analysis
SBAS	Small BAseline Subset
RAR	Real Aperture Radar
StaMPS	Stanford Method for Persistent Scatterers
TOPS	Terrain Observation with Progressive Scans SAR
SLC	Single Look Complex
PS	Persistent Scatterer
DS	Distributed Scatterer
ADI	Amplitude Dispersal Index
ERS-1 & 2	European Remote Sensing satellite -1 & 2
ENVISAT	Environmental Satellite
ALOS PALSAR-1	Advanced Land Observing Satellite Phased Array type L-band Synthetic Aperture Radar
RADARSAT	Radar Satellite
UTC	Coordinated Universal Time
PGA	Peak Ground Acceleration
USGS	United States Geological Survey
MFZ	Marlborough Fault Zone
CHIRPS	Climate Hazards Group InfraRed Precipitation with Station
GPM	Global Precipitation Measurement
SNAP	Sentinel Application Platform
ESD	Enhanced Spectral Diversity
SRTM	Shuttle Radar Topography Mission
IW	Interferometric Wide
ASF	Alaska Satellite Facility
GACOS	Generic Atmospheric Correction Online Service
ECMWF	European Centre for Medium-Range Weather Forecasts
ZTD	Zenith Tropospheric Delay
TRMM	Tropical Rainfall Measuring Mission
GPT	Graph Processing Tool
IDE	Integrated Development Environment
Ifg	Interferogram
Coreg	Co-registration
SCLA	Spatially-Correlated Look Angle
CLAP	Combined Low-pass and Adaptive Phase filter
TRAIN	Toolbox for Reducing Atmospheric InSAR Noise
$\mathbf{V_{LOS}}$	Line of Sight velocity
$\mathbf{V_{Slope}}$	Downslope velocity

GEE	Google Earth Engine
ESM	Extremely Slow Moving
VSM	Very Slow Moving
ESMH	Extremely Slow Moving Hillslope
VSMH	Very Slow Moving Hillslope
SU	Slope Unit
ADH	Actively Deforming Hillslope

1. INTRODUCTION

The overall research notion of this study, associated with the general background and justification that inspires addressing the prevailing research gaps in the literature, are communicated in this chapter. This chapter incorporates (1) *background and justification*, (2) *research gap and scientific contribution*, (4) *research objectives/questions*, and (5*) research design and thesis structure*.

1.1. Background and justification

In general, landslides are natural processes that involve downslope displacement of different slope materials (Cruden and Varnes, 1996). Landslides are considered one of the disastrous natural hazards that cause numerous fatalities and huge socio-economic losses globally, especially in mountainous regions where the development of infrastructure and population are increasing (Dowling and Santi, 2014; Badoux et al., 2016; Froude and Petley, 2018; Herrera et al., 2018; Haque et al., 2019). Apart from affecting the people and economy, landslides severely impact the environment in different ways, including destroying forests (Geertsema et al., 2009), deposition of sediment in streams (Booth et al., 2013), decreasing agriculture yield, and degrading water quality (Geertsema and Pojar, 2007). Various factors, such as rainfall, seismic shaking, snow melting, changes in temperature, groundwater level, volcanic activity, and anthropogenic activities, individually or combinedly control the stability of a hillslope (Gariano and Guzzetti, 2016). The landslides are the geomorphic response to these causative factors. Indication from recent studies suggests that the occurrence of landslides in mountainous terrain can increase multifold in the near future owing to the changing intensity of precipitation, temperature, and snowmelt (Huggel et al., 2012; Patton et al., 2019).

As per records, earthquake and rainfall-triggered landslides have caused large casualties and huge economic damages. Specifically, most catastrophic disasters that happened due to landslides after the 20th century had a seismic cause, even though rainfall-induced landslides are more frequent (Froude and Petley, 2018). Approximately 200,000 casualties were recorded between 1811 and 2016 due to earthquake-triggered landslides (Nowicki Jessee et al., 2020). In addition to the huge death toll, the world repairs damages worth billions of USD caused by earthquake-triggered landslides each year (Haque et al., 2019). Unlike rainfall-triggered landslides, which have the antecedent effect of rainfall, earthquake-triggered landslides occur all of a sudden on top of any active slope mechanism (Fan et al., 2019). Furthermore, damage triggered by strong ground shaking during an earthquake can produce cascading geohazards during the post-seismic phase and even years after the event (Fan et al., 2019). Identifying and monitoring the evolution of earthquake-triggered geohazards in post-seismic phase is essential for disaster prevention, loss mitigation, and for understanding how seismic activity impacts the regional geological situation (Cai et al., 2022).

Failure of hillslopes is one of the most common secondary geohazards associated with strong and moderate earthquakes (Mw[1] > 4) (Keefer, 1984). Slope failures that are immediately generated within minutes due to the intense seismic shaking are known as co-seismic landslides, whereas those slopes that fail subsequently are described as post-seismic landslides (Fan et al., 2019). In spite of increasing research related to co- and post- seismic catastrophic landsliding, our knowledge of sub-meter evolution of active hillslopes during post-seismic phase is considerably lesser. The geoscientific literature shows that severe ground shaking during an earthquake decreases the shear resistance of hillslope materials and leads to an elevated landslide susceptibility in post-seismic periods across hillslopes (Brain et al., 2017; Parker et al., 2015), which could

[1] Earthquake moment magnitude

be manifested by new or reactivated landslides (Figure 1). Specifically, ground shaking during earthquakes could create widespread fissures/tension cracks on the hillslope surface (see Figure 1), which decreases the hillslope strength and influences slow movement that displays no indication of rapid slope failure (Petley et al., 2010). A number of studies confirm this observation and show that strong seismic shaking not only triggers co-seismic landslides but also exacerbates hillslope stability in the post-seismic periods, which corresponds to the concept of earthquake legacy effect (Fan et al., 2019; Tang et al., 2016; Tanyaş et al., 2021a). However, no studies have focused on such incipient slow-moving landslides triggered by the earthquake shaking so far, except for some interpretations. For instance, Rosser et al. (2021) observed such cracks after the 2015 Gorkha earthquake and hinted about the possible development of slow-moving landslides triggered by the earthquake.

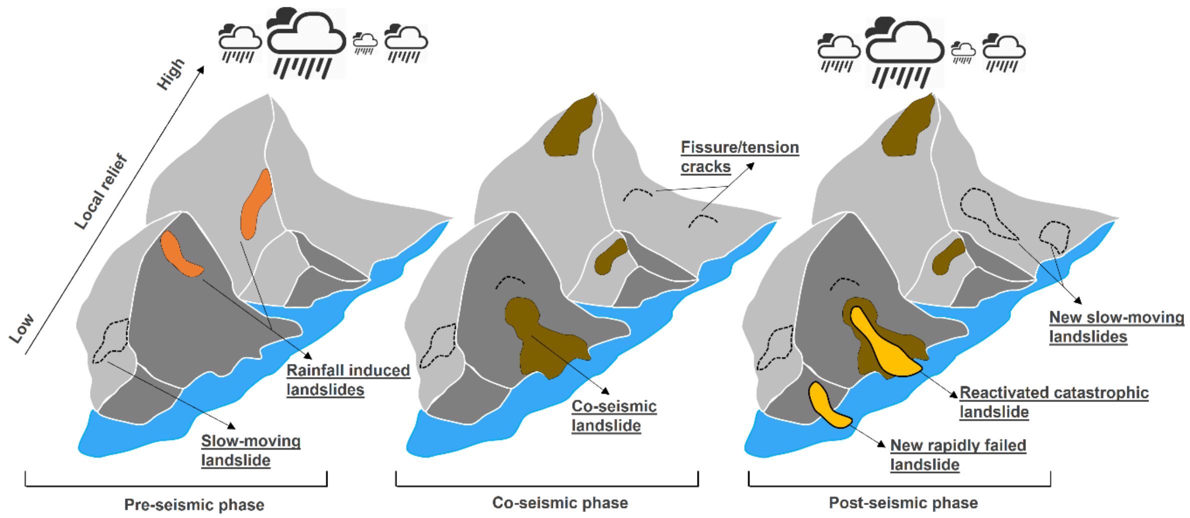

Figure 1. Graphic diagram of pre-, co-, and post-seismic landslide activity (adapted and modified from Tanyaş et al., 2021b).

So far, our understanding of earthquake legacy effect on post-seismic landsliding and their recovery time is mainly based on the examination of rapidly failed slope inventory, while the same has not been yet elaboratively analysed by identifying, mapping, and monitoring dynamics of slow-moving hillslopes. In fact, variations in surface deformation movements during pre- and post-seismic phases provide a more comprehensive picture of the earthquake legacy effect and its evolution over time than multi-temporal landslide inventories because surface deformation could exist regardless of landslide occurrences. Moreover, understanding how landslides originate/evolve after a common triggering event such as an earthquake can help us assess the post-seismic landslide hazard in a more robust way to plan preventive measures and reduce the risk from rapid catastrophic failure. This is an essential research question, in particular, for slow-moving hillslopes, which could lead to catastrophic failures (Palmer, 2017; Intrieri et al., 2018).

Any hillslope that exhibits millimeters to meters of downslope movement per annum is regarded as active or slow-moving landslide (Hungr et al., 2014). Generally, slow-moving landslides are widely present in seismically active parts of the world having weak soil and are mostly driven by seasonal rainfall (Handwerger et al., 2015). They have a significant influence on the evolution of landforms in such mountainous terrain (Booth et al., 2013). Deformation rate of an active hillslope displays different deformation episodes that are disconnected by a brief or extended period of dormancy (Lacroix et al., 2020). Many creeping, active hillslopes that display a millimeter to centimeter range of velocity per annum are considered as a major natural hazard as they go unnoticed and are only observed after the progressive rapid failure (Palmer, 2017).

Although the deformation rate in landslides having slow movement seldom accelerates, episodic or seasonal triggering events such as ground shaking (Lacroix et al., 2015), snowmelt, and rainfall (Handwerger et al., 2019; Bontemps et al., 2020) can increase the deformation rates. Specifically, earthquakes could influence the dynamics of active landslides in three different ways: (i) genesis/development of an active hillslope, (ii) reactivation of a dormant body constituting a new slow-moving hillslope (Martino et al., 2022), and (iii) acceleration or deacceleration of an actively deforming hillslope (Bontemps et al., 2020; Cheaib et al., 2022; Lacroix et al., 2022, 2015; Bekaert et al., 2020). However, there has been very limited research carried out particularly on the first two points mentioned above.

Monitoring of slope deformation in the range of millimeters was traditionally implemented by installing devices, such as GPS (Moss, 2000; Li et al., 2017), tiltmeter (García et al., 2010), extensometer (Corominas et al., 2000), crack meters (Tofani et al., 2014), total station (Artese and Perrelli, 2018), and inclinometer (Simeoni and Mongiovì, 2007) at certain places on the slope. Such instruments can provide precise point measurements of deformation, yet they lack high spatial density and are costly, time-consuming, and sometimes not viable to install the devices on steep slopes and over large regions (Royán et al., 2013). Hence, other alternative aerial and terrestrial remote sensors such as Light Detection and Ranging (LiDAR) were utilized to monitor the slope deformation. Even though LiDAR measurements deliver spatially high-density deformation information, it is rarely available for large areas. It also lacks temporal resolution due to the high cost of acquiring and handling the instrument (Stumpf et al., 2015). All the above-mentioned instruments lacked high spatial distribution or temporal resolution, which is essential for long-term monitoring of landslide deformation. Thus, researchers started employing satellite-based optical, multi-spectral, and microwave data for acquiring continuous deformation measurements with high temporal resolution over a wide spatial area. Both freely available multi-spectral and commercial optical datasets (Pléiades) have been used for identifying the deformation of landslides based on cross image correlation technique (Debella-Gilo and Kääb, 2012; Stumpf et al., 2017, 2014; Lacroix et al., 2018, 2015; Desrues et al., 2019; Xiong et al., 2020; Ding et al., 2021). However, the use of optical and multi-spectral data becomes limited in mountainous regions with a predominant cloud presence (Lacroix et al., 2018).

Surface deformation measurements can also be extracted using both amplitude and phase information of active coherent microwave data i.e., Synthetic Aperture Radar (SAR) data, which can retrieve deformation measurements in all weather conditions (Li et al., 2019). The amplitude information of SAR data can be used only for measuring rapid and large deformations ranging more than one meter in slant range and azimuth direction by employing Pixel/Feature Offset Tracking (Strozzi et al., 2002; Li et al., 2019). The phase measurement-based SAR interferometry (InSAR) derived from complex-valued SAR data can be utilized for retrieving deformations up to millimeters over large areas in the satellite line-of-sight (LOS) direction, which offers a vast opportunity for monitoring earth surface deformation due to human-induced (Chang et al., 2017) and natural processes such as an earthquake (Wright et al., 2004), land subsidence (Chaussard et al., 2014), landslide (Schlögel et al., 2015), volcano (Hooper et al., 2004) and sinkhole (Chang and Hanssen, 2014; Malinowska et al., 2019). Lately, there has been a rise in the number of studies that monitor the surface deformation from different processes due to the increase in the availability of SAR data compared to the past. It is also important to mention that ground-based InSAR (GB-InSAR) techniques are also utilized for surface deformation monitoring, providing spatially and temporally high-resolution deformation measurements for local slope regions but lacking applicability over large regions due to its high cost for installation and handling (Bardi et al., 2017; Ferrigno et al., 2017).

The use of spaceborne SAR data for landslide observation and modelling began way back in the middle of the 1990s (Fruneau et al., 1996), but only at the beginning of the 21st century did InSAR become famous for monitoring landslide deformations (Ferretti et al., 2001; Berardino et al., 2002; Hooper et al., 2004; Hooper, 2008; Meisina et al., 2006). Initially, Differential InSAR (DInSAR) was utilised for analysing landslide deformation. However, because of the limitations of DInSAR in geometrical and temporal decorrelation and atmospheric effects, multi-temporal InSAR (MT-InSAR) techniques, such as Persistent Scatterer Interferometry (PSI, Ferretti et al., 2001), SqueeSAR (Ferretti et al., 2011), Coherent Pixel Technique (CPT, Blanco-Sànchez et al., 2008), Interferometric Point Target Analysis (IPTA, Werner et al., 2003), and Small BAseline Subset (SBAS, Berardino et al., 2002) were employed for better monitoring of landslide deformation. There have been multiple studies ever since the development of the MT-InSAR technique that applied the method for detecting and monitoring slow-moving landslides and also understanding the process of slope deformation in remote areas of the globe (Bayer et al., 2017; Colesanti et al., 2003; Colesanti and Wasowski, 2006; Handwerger et al., 2015; Hilley et al., 2004; Wasowski and Bovenga, 2014). Among all MT-InSAR approaches, PSI and SBAS are the most frequently applied techniques for landslide deformation analysis (Bayer et al., 2017; Tantianuparp et al., 2013; Zhao et al., 2018). The MT-InSAR applications largely transformed the process of landslide monitoring and hugely aided researchers in understanding the evolution of slowly deforming hillslopes. It can be used to unveil the smallest of displacements that are happening within a slope. However, owing to the high computational requirement of MT-InSAR techniques, most of the research is performed in monitoring individual slopes rather than carrying out a region scale analysis.

Monitoring of hillslope deformation is extremely challenging in highly vegetated and mountainous terrain due to the growth of flora, which results in surged noise levels and decorrelation (Bekaert et al., 2020). In addition, geometric distortions in hilly terrain because of SAR sensors' side-looking imaging geometry increase the difficulty in quantifying and monitoring the deformation in slopes. In such circumstances, permanent scatterers are limited to manmade features and bare rocks in hilly terrain owing to low temporal decoherence. Furthermore, atmospheric phase delay that occurs especially in mountainous regions owing to elevation variations and clouds, rainfall, and snowfall in different seasons introduces noise in the acquired signal and affects the quality of extracted deformation measurements. Thus, temporal decorrelation and atmospheric effects are yet a critical challenge that has to be addressed in highly vegetated hilly terrain with low or no urban features, which mainly impedes the monitoring of deformation in slopes across the globe. Moreover, rapid progressive deformation that exceeds the deformation monitoring level of SAR products can also make deformation monitoring challenging. In such cases, SAR products having a minimal temporal baseline are appropriate for decreasing the temporal decorrelation by generating a perfect interferogram (Squarzoni et al., 2020). Currently, Sentinel-1A and 1B satellite sensors operating in C-band wavelength of 5.6 cm from 2014 and 2016, respectively, provide single or dual polarized SAR images with minimal temporal baseline (6-12 days). Therefore, this research attempts to use freely available and frequently acquired C-band SAR data from Sentinel-1A and 1B sensors with a short spatio-temporal baseline to monitor the hillslope deformations using the MT-InSAR technique, which confirms the extraction of spatiotemporally continuous deformation time-series.

1.2. Research gap and scientific contribution

First-ever time-series documentation of landslide reactivation owing to strong ground motion from an earthquake was accomplished by Lacroix et al. (2014). Based on the GPS time-series measurements, post-seismic displacement was measured to be larger than that of the co-seismic response of landslides to ground shaking. This research was significant as it marked the starting point for studies that investigate post-seismic landslide activity with a special focus on identifying slow-moving hillslopes that were activated and/or reactivated based on deformation time series. In support of this argument, Lacroix et al. (2015) identified nine active slow-moving hillslopes that were accelerated by an earthquake of magnitude six and the level of groundwater using high-resolution optical remote sensing images. Bekaert et al. (2020) identified six slow-moving hillslopes in a region affected by the 2015 Gorkha earthquake (Mw =7.8), using the MT-InSAR technique, that was displaying analogous slow deformation rates before (2014-2015) and following (2016-2017) the event. The authors examined the pre-and post-Gorkha deformations time series separately but did not explore the dynamics of active or reactivated hillslopes in post-seismic periods.

The most recent developments in analysing slow-moving hillslopes using InSAR time series in relation to earthquakes were published during the course of this work and are discussed as follows. Lacroix et al. (2022) addressed this gap and revealed the lagged initiations and post-seismic relaxations of slow-moving landslides in the area hit by the 2015 Gorkha earthquake using Sentinel-1 data. During this post-seismic relaxation phase, slow-moving hillslopes were found to have accelerating deformation mainly because of the groundwater transmission. Also, Martino et al. (2022) showed slow activations and reactivations of landslides following a small magnitude (Mw = 5.1) earthquake in Italy with the help of the D-InSAR technique. Lately, Cheaib et al. (2022) uncovered three distinct post-seismic deformation pattern hillslopes affected by ground motion from the 2017 Sarpol Zahab earthquake (Mw = 7.3): a) post-seismic motion identical to pre-seismic level, b) steady increase in the post-seismic deformation velocity, and c) temporary increase in post-seismic velocity, which recovers to pre-seismic level in some time after the earthquake. Very recently, Cai et al. (2022) identified 16 slowly moving landslides that were developed after an earthquake of magnitude 7, which occurred on 8 August 2017 in Sichuan Province of China, with the help of SBAS and LiDAR techniques. The latest preprint from Cao et al. (2022) identified multiple slow-moving landslides that were generated from the intense ground shaking during the 2016 Kaikōura earthquake. The authors of this research used a phase gradient-based InSAR approach that is different from that of MT-InSAR techniques.
This growing number of recent publications in the course of this research affirms that there is a growing interest in the geoscientific community for unveiling the dynamics of incipient slow-moving hillslopes that are triggered by large magnitude earthquakes. This study will contribute to this notion and lead to inspiring many new findings in this prospective research direction.

To our knowledge, by going through the published literature so far, a) there has not been much work performed on identifying, mapping, and studying the sub-meter evolution of hillslopes that are primarily caused by the intense seismic shaking and driven by its legacy effect. It is also important to note that all the above mentioned studies except the last one use the computational intensive SBAS approach in regions (smaller than 1500 km^2) affected by the earthquake for identifying and studying the evolution of slow-moving hillslopes. There are quite a few studies that employ the PSI approach for detecting active movements of slopes in mountainous areas, but to my knowledge, no study has yet utilised the approach for investigating hillslopes affected by intense seismic shaking (Aslan et al., 2020; Lu et al., 2019, 2011). Thus, in this research, a new systematic PSI-based approach is designed by integrating various pre- and post-processing steps to detect and study the sub-meter evolution of active hillslopes that existed before and those that are generated after a large magnitude earthquake using the freely available Sentinel-1 dataset.

This research is among the first to use slope units (SUs) for identifying those hillslopes that are slowly moving instead of commonly used pixel clustering methods (Bekaert et al., 2020). Most of the MT-InSAR works focus on single slope failures and rarely address the dynamics of hillslopes affected by a single large triggering event like an earthquake. Examining the sub-meter level post-seismic evolution of hillslopes gives much information for us to assess post-seismic landslide hazards and risks. This research will focus on the hillslopes affected by a single triggering event and reveal new insights on their dynamics and evolution with the help of surface deformation extracted using the PSI approach.

In addition, a modest post-seismic hillslope deformation scheme is proposed in this work based on the findings of this study which can be applied in mountainous regions affected by the earthquake to classify a different kind of sub-meter hillslope deformation activity before and following the earthquake. Unlike the complex landslide activity matrix suggested by Cigna et al. (2013), which requires pre-existing inventory, the one proposed in this study doesn't require a pre-existing inventory and is less intricate to understand and for applying in an earthquake-impacted hillslopes.

1.3. Research objectives

1.3.1. General objective

The main objective of this research is to reveal the impact of intense seismic shaking from a large magnitude earthquake on the sub-meter dynamics of hillslopes using Sentinel-1 SAR (Synthetic Aperture Radar) images.

1.3.2. Sub-objectives and research questions

Based on the overall objectives, four sub-objectives and associated research questions are described as follows:

1. **To extract the pre- and post-seismic LOS deformation of hillslopes using Sentinel-1 SLC IW mode images employing the PSI approach.**
2. **To analyse the distribution of deformation measurements over different landscape characteristics.**
3. **To develop a systematic approach to identify and map the actively deforming hillslopes during pre- and post-seismic phases.**
4. **To develop a post-seismic hillslope deformation scheme for describing different hillslope evolution.**

The following are the research questions associated with the sub-objectives defined above:

i. What optimum configuring parameters for the PSI approach to retrieve the LOS deformation measurements of (constantly) coherent radar scatterers? (sub-objective 1)
ii. What are the differences between pre- and post-seismic mean annual LOS deformation velocity? (sub-objective 1)
iii. How does deformation measurement change across basic morphometric variables such as elevation and slope steepness during the pre- and post-seismic phases? (sub-objective 2)
iv. How does deformation measurement change across places experiencing different PGA during the post-seismic phase? (sub-objective 2)
v. What are the different landforms and lithologies that control the active deformations? (sub-objective 2)
vi. What is the best critical stability threshold that can be defined to detect and characterise the active PS? (sub-objective 3)
vii. What are the different types of post-seismic sub-meter hillslope evolution captured in this study? (sub-objective 4)

1.4. Research design and thesis structure

Figure 2 displays all the steps followed in this work order to address the research objectives and questions, including the qualitative part of the literature review. Extraction of LOS deformation measurements from Sentinel-1 images using the PSI approach helps in answering sub-objective 1, while analysing the distribution of PS over different landscape characteristics aids in addressing sub-objective 2. The identification of actively deforming hillslopes during pre- and post- seismic phases addresses sub-objective 3, and the detection of different types of sub-meter hillslope evolution after the impact of the earthquake with the help of the proposed post-seismic hillslope deformation scheme aids in resolving sub-objective 4.

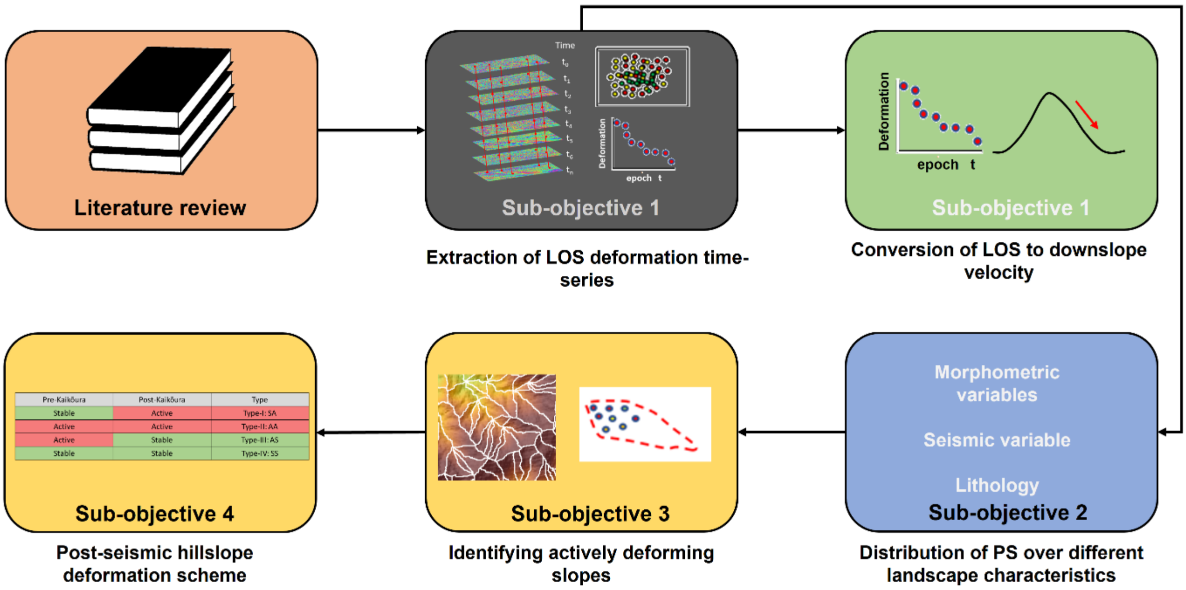

Figure 2. Design of this research work.

This work is structured in a traditional way with six chapters. Chapter 1 discusses the general motivation, research gap, and problem in the study that is undertaken, while Chapter 2 provides a detailed overview of fundamental concepts and a comprehensive review of articles related to the research carried out in this work. Chapter 3 describes the study area's locational, tectonic, geologic and climatic setting and the datasets used. Chapter 4 provides information on the methodology. Chapter 5 presents the results of this work which will be discussed in Chapter 6. The conclusion and recommendation of this work will be given in Chapter 7.

2. LITERATURE REVIEW

This chapter provides information on the fundamental concepts essential for understanding this research work. Theoretical overview of imaging radar (SAR) and radar interferometry (InSAR) is presented in Section 2.1 and Section 2.2, respectively; the basics of PSI technique is discussed in Section 2.3, and a comprehensive literature review of PSI applications related to slope deformation is examined in Section 2.4.

2.1. Imaging radar (SAR, Synthetic Aperture Radar)

Radio detection and ranging, abbreviated as Radar, signifies both an approach and device which is utilised to identify, locate, and track an object by emitting and recording the reflected microwave and radio electromagnetic waves in its line-of-sight (LOS) either using the same antenna (monostatic) or with different antennas (Bistatic) (Skolnik, 1962). Detection of an object was ascertained by calculating the two-way travel period of the pulses. Physical properties of the detected object, such as size, orientation, and surface roughness, can be inferred from the reflected pulses. Radar can be used in all weather conditions and during any time of the day and night as it doesn't require any natural light sources (Hanssen, 2001).

Initially, Real Aperture Radar (RAR), a particular group of side-looking incoherent imaging radars having long antennas that are mounted to an airborne or space-borne vehicle, were used to acquire images of the Earth's surface. Owing to the issues in having a long antenna both in space and air resulted in images with very coarse resolution. This difficulty was overcome by using a coherent imaging radar system called SAR, which uses an artificially large antenna. This advancement helped in increasing the azimuth resolution drastically. In addition, both amplitude and fractional phase information from the sensed objects are retained. Side looking geometry of a SAR system is represented in Figure 3.

The amplitude A measured by the SAR sensor signifies the strength of reflection coming back from an object, while the phase is the tiny proportion of the entire wave cycle reflected to the sensor. Any difference in two consecutive signals results in a phase change which is represented as follows (Hanssen, 2001);

$$\phi_s = \frac{2\pi}{\lambda} 2r = \frac{4\pi}{\lambda} r \quad (1)$$

Where, ϕ_s refers to phase change, 2r is the two-way travel distance of the radiation, which is inversely proportional to the transmitted wavelength λ. The difference in phase can only be quantified between [-π, π), or (-π, π].

Both amplitude and fractional phase ψ measurement reflected from the objects on the Earth's surface is stored combinedly as a complex phasor P for every individual pixel in the two-dimensional image.

$$P = Aexp(i\psi) \quad (2)$$

Here i is the imaginary unit.

Thus, every pixel shows distinct scattering characteristics based on the reflections from different objects having various scattering properties. There can be two furthermost cases, where the presence of a strong scatterer within a pixel can result in a high signal-to-noise ratio, and in another case, a pixel can be a distributed scatterer where scattering from all the objects within the pixel contribute.

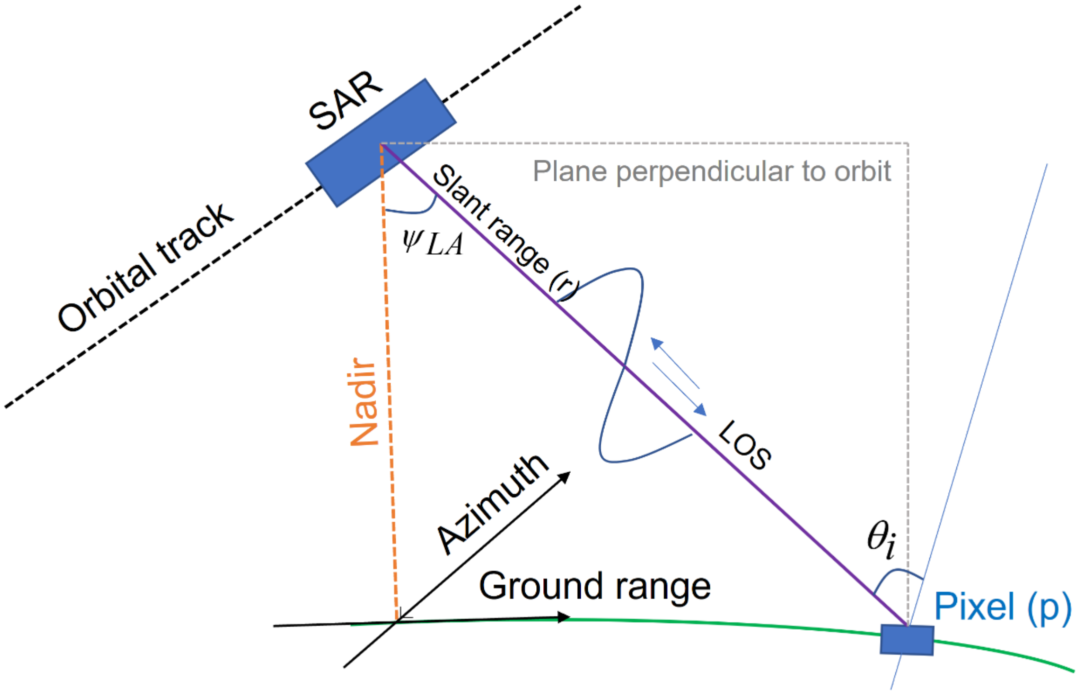

Figure 3. Right-facing geometry of SAR system, where ψ_{LA} is the look angle and θ_i is local incidence angle.

It is not feasible for the imaging radar to distinguish two distinct objects that lie in the same range to the radar system owing to its major drawback in determining angles. This problem led to the formation of interferograms by merging to complex SAR images, which aided in acquiring phase variance that helped in overcoming the above limitation. This procedure is popularly known as the InSAR technique, in which the complex phase of the reference image (R) is multiplied with the complex conjugate (S*) of the secondary image[2] (Hanssen, 2001).

$$I = R \times S^* \tag{3}$$

The Single Look Complex (SLC) images are used for generating interferograms, where the complex phase of the SLC product can be given as follows (Hanssen, 2001):

$$\psi_{SLC}^{uw} = -2\pi k + \psi_{range} + \psi_{atmos} + \psi_{scat} + \psi_{noise} \tag{4}$$

Where, k is the uncertainty of phase, which is introduced because of complete phase cycles that varies between $(-\pi, \pi)$, whereas other components of the equation signify the phase component introduced by range dependency ψ_{range}, atmosphere ψ_{atmos}, scattering ψ_{scat}, and noise ψ_{noise}. The superscript uw indicated the unwrapped phase. More on the InSAR technique is elaborated in the following Section 2.2.

2.2. Radar interferometry (InSAR, Interferometric SAR)

InSAR is one of the most robust and widely accepted remote sensing-based techniques for acquiring millimeter-level deformation signals of Earth's surface. Deformation is retrieved using interferograms generated with phase differences from complex-valued SAR images, acquired over the same geographical

[2] The term "master" and "slave" images have been replaced as "reference" and "secondary" images in this work. This change of terms was initiated by WInSAR and COMET committee, which is supported by InSAR scientific community around the world.

location at a different time with identical sensor characteristics (Bamler and Hartl, 1998). The images are co-registered on a coordinate system in which the introduction of phase owing to topographic inaccuracy, and orbit error is adjusted (Bamler and Hartl, 1998; Gabriel et al., 1989; Rosen, 2000). The targeted deformation phase φ_{Defo} is among the components of the unwrapped differential interferogram phase $\varphi_{D-Interferogram}$ which comprises a flat-earth phase φ_{flat}, atmospheric phase φ_{Atm}, topographic variance error φ_{Topo}, orbital inaccuracy φ_{Orbit}, phase noise φ_{Noise}, scattering phase φ_{scat} and phase ambiguity (k) due to wrapped characteristics (π) of differential interferogram phase (Hanssen, 2001). The unwrapped differential interferogram phase can be represented as follows (Hanssen, 2001):

$$\varphi_{D-Interferogram} = W\{\varphi_{D-Interferogram}\} + 2k\pi = \varphi_{flat} + \varphi_{Topo} + \varphi_{Defo} + \varphi_{Atm} + \varphi_{Noise} + \varphi_{scat} + \varphi_{Orbit}. \quad (5)$$

The important aim of the D-InSAR technique, as aforementioned, is to extract φ_{Defo} from $\varphi_{D-Interferogram}$ excluding other phase elements of Equation 5. $W\{.\}$ is the wrapping operator. Each term of the interferometric phase will be detailed in the following paragraphs.

Flat Earth phase (φ_{flat}) implies the phase contributed because of a reference surface, which is ellipsoid in the instance of Earth. By presuming that both reference and secondary antennas are parallel, the flat Earth phase at a location can be represented as follows:

$$\varphi_{flat} = \frac{4\pi}{\lambda} B_{\parallel} \quad (6)$$

B_{II} signifies the parallel baseline.

Topographic phase φ_{Topo} represents the phase contribution of the elevation, while the deformation phase φ_{Defo} consists of phase contribution due to changes in earth surface between reference and secondary image. The deformation phase φ_{Defo} can be formulated as follows:

$$\varphi_{Defo} = -\frac{4\pi}{\lambda} defo_{LOS} \quad (7)$$

Where $defo_{LOS}$ refers to the line of sight deformation, and it comprises deformation in both horizontal and vertical directions.

The difference in atmospheric contents between reference and secondary images could create atmospheric delay (φ_{Atm}), which mainly comprises tropospheric and ionospheric delay. The orbital issues of a SAR system can give rise to orbit errors (φ_{Orbit}). Variation in the surface conditions between reference and secondary acquisitions introduces the scattering phase (φ_{scat}), which is the main reason behind decoherence. Finally, the noise from all sources, including the thermal noise of the SAR system, creates noise in interferograms.

The conventional D-InSAR technique is not suitable for handling the geometrical and temporal decorrelation and atmospheric effects, which inhibit the technique from analyzing the deformation of the Earth's surface over a long time. Such limitation of the D-InSAR technique gave rise to the development and deployment of different MT-InSAR techniques, which uses a stack of multiple interferograms to extract deformation along the LOS direction by analyzing a subset of pixels rather than examining the whole interferogram, that is less affected by temporal decorrelation. Permanent/Persistent Scatterer (PS) and Distributed Scatterer (DS) targets affirm this condition of having low temporal decorrelation and φ_{Noise}.

As the name suggests, PS are those objects that have a stable dominant reflection to radar signal over time, whereas the reflection to radar signal in the case of DS is from various spatially-homogenous scattering objects within a resolution cell that are (temporally) stable (Crosetto et al., 2016). In this way, the MT-InSAR techniques can be categorized into three types: a) techniques that analyse PS targets (Ferretti et al., 2001, 2000; Hooper et al., 2004), b) techniques that analyse DS targets (Berardino et al., 2002; Lanari et al., 2004), and c) the last type is a hybrid technique that uses a combination of both PS and DS (PSDS) (Ferretti et al., 2011; Hooper, 2008) for extracting long term time-series deformation measurements. Interferogram network, conditions for choosing coherent pixels (either PS or DS), the model utilised for deformation, and other unwrapping techniques are some of the different properties that differentiate one MT-InSAR approach from another (Minh et al., 2020). The techniques that use PS targets for deformation extraction are generally known as PSI (Persistent Scatterer Interferometry), whereas those that utilise DS targets are called SBAS (Hooper, 2008). The terminology of these techniques is inconsistent as PSI refers to the pixels chosen for the analysis while SBAS (Small Baseline Subset) implies the interferogram generation process. The following section elaborates on the PSI technique.

2.3. Persistent Scatterer Interferometry (PSI)

The approach was primarily known as the permanent scatterers approach (Ferretti et al., 2001), but now it's been called PSI. Unlike D-InSAR, which utilizes two complex-valued SAR images to generate interferogram pairs, PSI uses a huge quantity of complex-valued SAR images along with appropriate parameter configuration, data administering, and analysis to retrieve the deformation time series of the Earth's surface. This method makes use of the stable PS pixels, which were chosen initially based on only the amplitude stability (also known as Amplitude Dispersion Index, ADI) (Ferretti et al., 2001). In urban regions, PS targets were high compared to the natural terrains. However, there were some limitations to the amplitude stability-based selection of PS targets in the non-urban regions, so Hooper et al. (2007) introduced the phase stability-based PS candidate selection, which produced dense PS points in non-urban terrains. There are numerous approaches currently available that utilize the usefulness of PS targets for overcoming the issue of decorrelation owing to atmospheric phase, geometric and temporal incoherence with a slightly different approach in selecting PS targets and deformation modelling (Minh et al., 2020). All these approaches perform PSI based on the single prime interferogram stack.

The Stanford Method for Persistent Scatterers (StaMPS, Hooper et al., 2012; Hooper, 2008) is a widely used tool for MT-InSAR processing. During the PSI processing with the help of StaMPS, filtering and multi-looking are ignored to preserve the quality of deformation estimation (Hooper et al., 2012). Co-registered reference and secondary images and the stack of single reference[3] time-series topography corrected interferogram along with elevation and orthorectified latitude and longitude bands are required to process PSI in StaMPS. Some of the important characteristics of StaMPS include the selection of PS targets considering both amplitude stability and estimated phase stability. Initially, a certain ADI threshold is fixed during amplitude stability analysis for selecting a subset of PS targets. The ADI can be written as follows (Ferretti et al., 2001):

$$ADI = \frac{\sigma_A}{\mu_A} \tag{8}$$

Where, σ_A represent the standard variance of amplitude and μ_A refers to the average amplitude of SAR images. Hooper et al. (2007) used a high value of *ADI*, resulting in a low number of PS pixel selections

[3] Single-master interferogram is replaced as single-prime interferogram

during the initial amplitude stability analysis. Subsequently, phase stability analysis is carried out with the help of estimated phase stability, which ignores the non-PS targets and only selects those dominant PS pixels in all interferograms over time. After the PS selection, further procedures such as unwrapping of phase and removal of atmospheric phase are performed for extracting the deformation values.

2.4. Application of PSI technique in the context of slope deformation

In recent years, the PSI technique has been applied in many slope deformation studies (Solari et al., 2020b), including pre- and post-failure analysis (Xia et al., 2022), detection, characterization, and monitoring of extremely slow and very slow deformation of slopes (Aslan et al., 2020), and its inventory mapping (Rosi et al., 2018). The following paragraphs discuss in detail the above-mentioned individual applications of the PSI technique related to slope deformation.

A literature review carried out based on the keywords of landslides and PSI in the Scopus database showed that 100 peer-reviewed articles were published from 2006 till the present (Figure 4). In order to draw a comparison between the number of articles published each year with the keywords landslides and InSAR is displayed in Figure 4, which sums to 516 articles from 2000 till now. In parallel to the increasing number of papers published on landslides, InSAR-based landslide analyses have also been gaining popularity in the geoscientific community. However, InSAR-based analyses still constitute only a small portion of landslide-related scientific contributions. This is to say that InSAR-based analyses can still be implemented in various research questions evolving around the landslide topic.

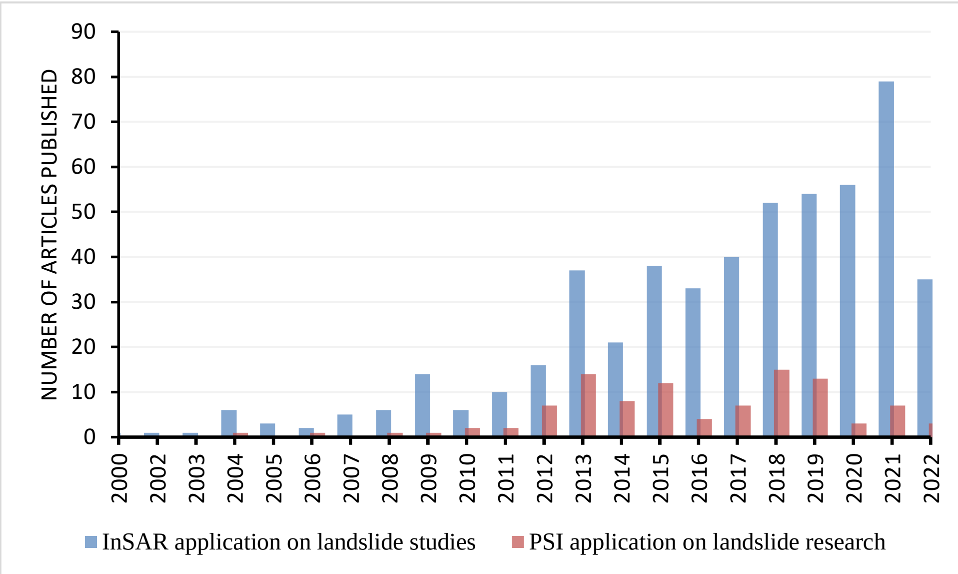

Figure 4. Peer-reviewed articles in Scopus database[4]. Brown bars represent the temporal distribution of articles that use PSI for the application of landslides and blue bars represent the list of published articles that employed InSAR for landslide studies.

Intrieri et al. (2018) studied the pre-failure deformation of the Maoxian landslide, situated in the Sichuan province of China, which failed on 24 June 2017, using the PSI technique (CPT) by analysing 45 Sentinel-1 SAR images that were acquired before the slope failure. The deformation time series of this popular study revealed precursory signs of failure on the scarp region of the slope. The authors of this study speculate that

[4] It should be noted that there can be other published articles which are not included in the Scopus database but uses PSI or InSAR for landslide studies. This list is taken only from Scopus database.

strong seismic ground motion could have led to slope instability. Xia et al. (2022) studied precursory deformation of a landslide (Aniangzhaire activated in 2020) located in the same province of China as the previous study, by employing the PSI and SBAS technique separately. In this study, Sentinel-1 descending data was only utilised, and time series analysis was split into two periods, one from 2014 to 2017 and another between 2018 and 2020, to overcome the temporal decorrelation limitation. The deformation results show precursory signs of reactivation starting from 2018. Shankar et al. (2022) investigated the precursory deformation of rainfall-triggered slope failure, which occurred on 30 July 2021, sited in the Sirmaur region of Himachal Pradesh by analysing ascending and descending Sentinel-1 images between July 2019 and July 2021. Examining the time series of Sentinel-1images revealed accelerating deformation of slope, which was unnoticed before the failure. Most of these studies analysing pre-failure deformation time series used the inverse velocity method to predict the time to slope failure (Carlà et al., 2019; Roy et al., 2022; Shankar et al., 2022). However, it is not applicable in all studies, and the limitation to forecast slope failure has been elaborately discussed in Moretto et al. (2021). Moreover, back analysis is widely performed for single slope failures and rarely for significant large events.

The post-failure deformation monitoring of slopes is necessary as studies suggest that reactivation and new activation of slopes can be possible following the failure event (Martino et al., 2022; Wang et al., 2022). Greif and Vlcko (2012) studied the post-failure deformation of a rainfall-triggered landslide (Lubietova) in Slovakia using ERS 1,2 and ENVISAT satellite images. The results indicated that the Lubietova landslide followed creeping movements in its post-failure phase. A limited number of studies have examined the earthquake-driven acceleration of slopes in the post-seismic phase (Lacroix et al., 2015), but the PSI technique hasn't been employed in such works.

2.4.1. Data availability

For performing a pre- and post-failure deformation analysis with the InSAR technique, it is really important to have enough SAR data before and following the event. The freely available SAR dataset examples are ERS[5]-1 and 2, ENVISAT[6], ALOS-PALSAR[7]-1, and Sentinel-1 (Table 1). In addition, some Radarsat[8]-1 data is also freely available.

Table 1. SAR dataset examples that are available for deformation analysis. Availability of ascending and descending images can be different.

SAR Dataset	Band	Availability	Repeat time (days)
ERS-1	C	1991 - 1997	35
ERS-2	C	1995 - 2011	35
ENVISAT	C	2002 - 2012	35
ALOS PALSAR-1	L	2006 - 2011	46
Sentinel-1	C	2014 - Ongoing	6 - 12

Over the years, the MT-InSAR technique has become popular for identification, monitoring, and inventory mapping of slowly deforming hillslopes, and a few case studies have been presented in Table 2.

[5] European Remote Sensing (ERS)
[6] Environment Satellite (ENVISAT)
[7] Advanced Land Observing Satellite Phased Array type L-band Synthetic Aperture Radar (ALOS PALSAR)
[8] Radar Satellite (RADARSAT)

Table 2. Literatures published on the PSI application of landslide studies. ENV, SNT, CSK, and ALOS refers to ENVISAT, Sentinel-1, COSMO-SkyMed, ALOS PALSAR.

Application	Case of study	Data source	Findings	References
Dynamics monitoring	Berkeley vicinity, Eastern San Franisco Bay area	ERS-1/2 (1992 – 2001)	Discovery of non-linear relationship between rainfall and slope kinematics.	(Hilley et al., 2004)
Updating landslide inventory	Bologna province, Italy	ERS-1/2 (1992 – 2001), ENV A & D (2003 – 2008)	Updating already available landslide inventory was carried out.	(Sara et al., 2014)
Detection, characterisation & inventory mapping	Palos Verdes Peninsula, California	ENV D (2005 - 2010), CSK D (2012 - 2014)	263 slow-moving landslides have been mapped and classified into 4 categories.	(Fiaschi et al., 2017)
Detection & monitoring	Veneto Region, Italy	SNT-1A A (2014 - 2016), D (2015 - 2016)	Assessing the potential of SNT in detecting and monitoring reactivation of past landslides.	(Bouali et al., 2018)
Inventory mapping	French Alps	SNT A (2016 - 2019) and D (2015 - 2019)	Over 100 actively deforming slopes were mapped	(Aslan et al., 2020)
Active deforming areas detection	Valle d'Aosta area in Alpine region	SNT (2015 – 2018)	Potential risk map was generated using active deforming slopes for the region.	(Solari et al., 2020a)
Activity mapping	Polish Carpathians	ALOS A (2008 - 2010), SNT A (2014 - 2017) & D (2014 – 2017)	43 actively moving slopes which could potentially affect infrastructures were mapped.	(Pawluszek-Filipiak et al., 2021)

3. STUDY AREA AND DATASET

This chapter focuses on the locational setting of the study area along with its tectonic and geologic characteristics in Section 3.1 and 3.2, respectively. Information regarding the climatic setting of the region under examination is provided in Section 3.3, while details on the dataset utilised for this research are provided in Section 3.4.

3.1. Geographic setting

In order to address the research objectives and questions, we chose to focus on hillslopes in a region affected by the 7.8 Mw Kaikōura earthquake, which hit the north-eastern region of New Zealand's Southern Island on 14 November 2016 at local time 12:03 am (as per UTC, the earthquake occurred on 13 November 2016). Earthquake hypocentre was located at 15.1 km depth, and rupture originated from 173.02° longitude and -42.69° latitude (Duputel and Rivera, 2017). Even though, an earthquake was not surprising given the historic seismicity of the region, still, the 2016 Kaikōura Earthquake displayed a more complex rupturing mechanism involving more than 11 fault planes. Earthquakes are commonly assumed to occur owing to the rupture of single fault, which makes the 2016 Kaikōura earthquake to be the most complex earthquake ever recorded (Hamling et al., 2017). There has been no such large magnitude earthquake documented in the history of New Zealand for over 100 years (Ulrich et al., 2019). Entire New Zealand felt the powerful ground shaking while widespread destruction was recorded to the north of Southern Island. The losses attributed to the event was around 3 to 8 billion New Zealand Dollars, which is around 1.8 to 4.9 billion Euros based on the exchange rate in 2022. The study area chosen for this project extends from the southern latitude of 41° 45' 20.57" to 42° 22' 42.50", and between eastern longitudes of 173° 23' 4.86" and 174° 10' 43.94", covering an area of about 2300 km^2 (Figure 5). The elevation of the study area ranges between 0 and 2855 m above mean sea level.

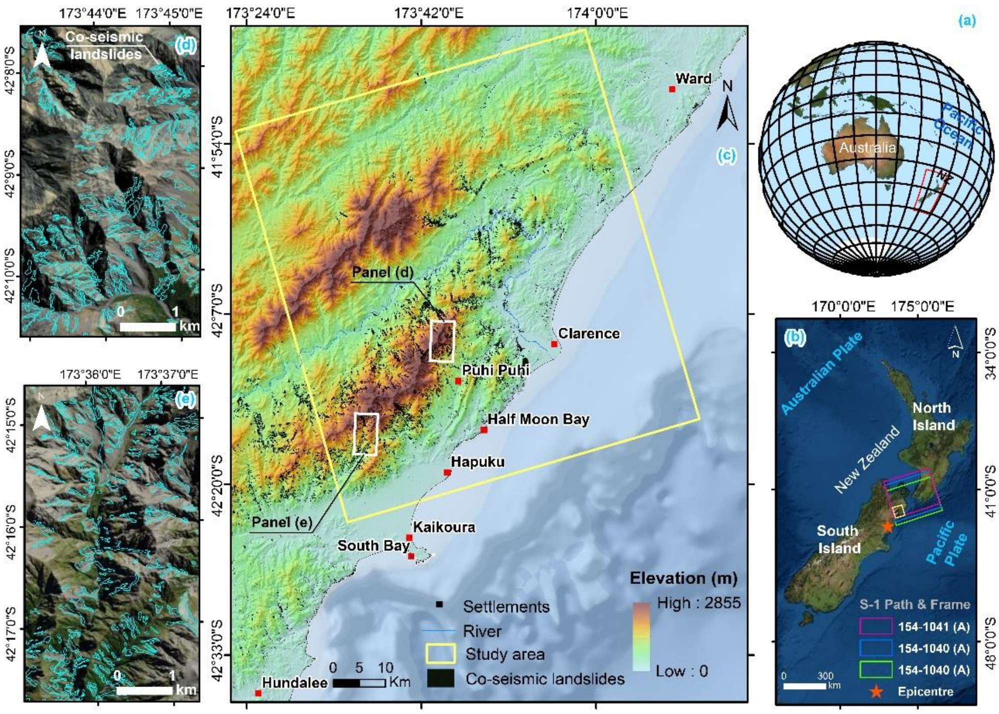

Figure 5. Study area. (a) Insert map shows the geographical situation of New Zealand in the world map, (b) The location of study area in New Zealand along with the Sentinel-1 frames covering the study area,

and (c) physiographical setting and co-seismic landslide distribution of the study area affected by the 2016 Kaikōura earthquake (Mw = 7.8). A in the legend of insert map (b) signifies ascending images. Co-seismic landslide polygons that occurred during the 2016 event mapped by Tanyaş et al. (2022a) are displayed (d-e).

Displacements over 8 meters are observed in some Southern Island regions(Hamling et al., 2017). The event generated more than 14,000 co-seismic landslides, according to the recent open dataset published by Tanyaş et al. (2022a).

Among the wide area affected by the 2016 Kaikōura earthquake, the particular region investigated in this work is chosen mainly i) to exploit available Sentinel 1 image and ii) to examine the area hosting a large number of co-seismic landslides as a result of strong ground shaking induced by the Kaikōura earthquake.

During the 2016 Kaikōura earthquake, the area under consideration was exposed to high Peak Ground Acceleration (PGA) ranging between 0.06g and 1.02g (Figure 6). Based on the scales followed by USGS, four different classes of PGA occurred within the study area, namely Very Strong (18 – 34 %g), Severe (34 – 65 %g), and Violent (65 - 124 %g). The Kekerengu fault, Jordan fault, and a part of Fidget fault experienced violent PGA. Most of the co-seismic landslides that occurred during the event happened in regions affected by severe and violent PGA.

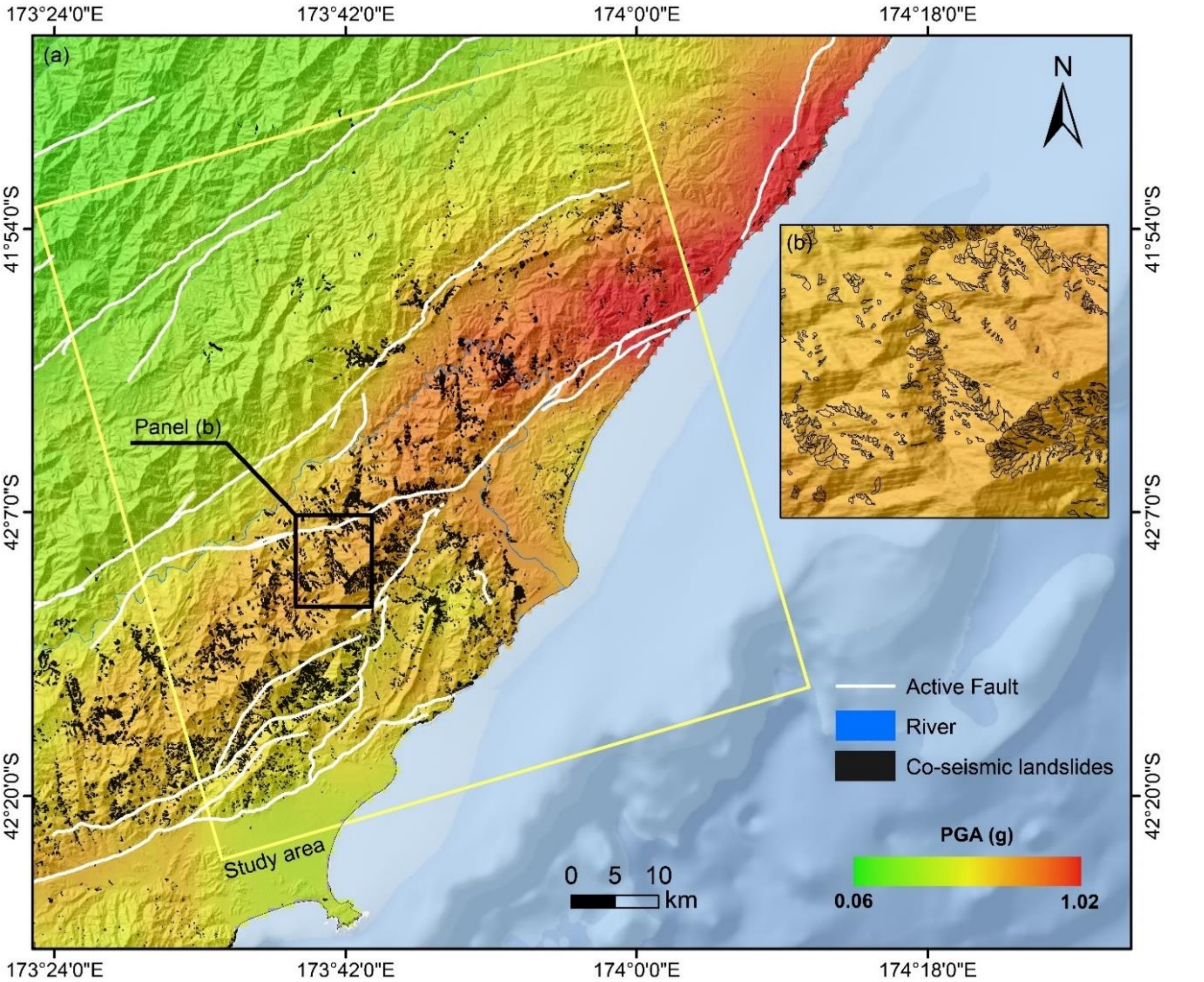

Figure 6. PGA of the study area given in gravity. Co-seismic landslides (grey polygons) and active fault (white lines) are overlaid upon PGA to understand their distribution. Panel (b) shows PGA overlaid with co-seismic landslides.

3.2. Tectonic and earthquake characteristics

The tectonics of New Zealand is controlled by the converging and transforming of Australian and Pacific plates. The Australian plate is located to the north and Pacific plate to the south of New Zealand (Ristau, 2008). Subduction of Pacific plate below Australian plate happens along the northern island of New Zealand while vice versa happens along the southern part of southern island of New Zealand. The first subduction zone mentioned above is called as Hikurangi Subduction Zone, while the latter one is known as Puysegur Subduction Zone (see Figure 7). The motion of the Puysegur Subduction Zone is about 35 mm/yr, and that of Hikurangi Subduction Zone is about 45 mm/yr (Howell et al., 2020). Alpine transform fault zone is located in the middle western coastline of New Zealand's southern island, which splays into Marlborough Fault Zone (MFZ) in the north-eastern part of southern island (see Figure 7). Important splay faults near the epicentre of the 2016 Kaikōura earthquake include Waihopai, Awatere, Clarence, Fidget, Kekerengu, Jordan, Uwerau, Kowhai, and Hope fault from north to south. The slip rate is high at Hope fault, which decreases with the splay faults situated towards the north of it (Vermeer et al., 2021).

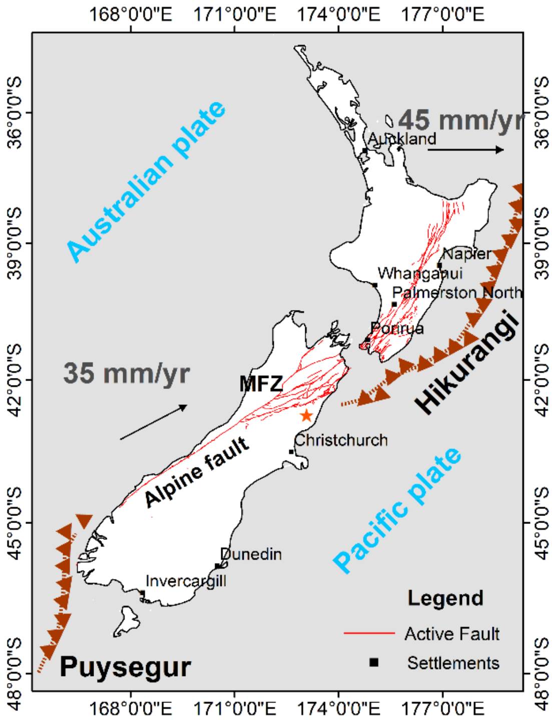

Figure 7. General tectonic setting of New Zealand. Significant faults are represented with red line and the movement of Australian plate proportional to Pacific plate is marked with black arrows.

The 2016 Kaikoura earthquake happened in the complex MFZ fault system which connects Hikurangi Subduction Zone and Alphine fault (Wang et al., 2018). The initiation of earthquake was from Humps fault rather than from Hope fault which has the largest slip rate among the splay faults near the epicentre (Kaiser et al., 2017). Strating from Humps fault, the fault rupture propagated to Papatea fault and Kekerengu fault rather than to Hope fault. First shock of earthquake lasted for about 2 minutes which was followed more intense one (Guo et al., 2019). Multiple aftershocks were also recorded in the region hit by the earthquake in 2016. Unforeseen motion of various faults cannot be explained based on normal fault mechanism. In the case of Jordan fault, both walls of the fault raised wherein hanging wall got uplifted above foot wall (Wang et al., 2018). Along with other cascading geohazards, the earthquake also triggered a tsunami of 5m even though the depth of occurrence is approximately about 15 km subsurface (Lane et al., 2017).

3.3. Geological setting

The examined area mainly consists of four geological units (Figure 8). Among which Lower Cretaceous Torlesse (basement rocks) are the predominant and oldest rock in the region, and Quaternary silt, lime and sandstones are the youngest rock. Greywacke is the predominant basement rock type found in Kaikōura and the whole of New Zealand.

Greywacke has its origin from sediment present in underwater trench of Gondwana continent, which dates back to hundred million years. Transformation from sediment to sandstone occurred because of the tension from tectonic activities. Even though Greywacke is a hard rock, it can be weak and unsteady, especially along the fault systems. Other than the above-mentioned geological units, the region comprises of Late Cretaceous to Paleogene sedimentary rocks and Neogene sedimentary rocks (Massey et al., 2018a).

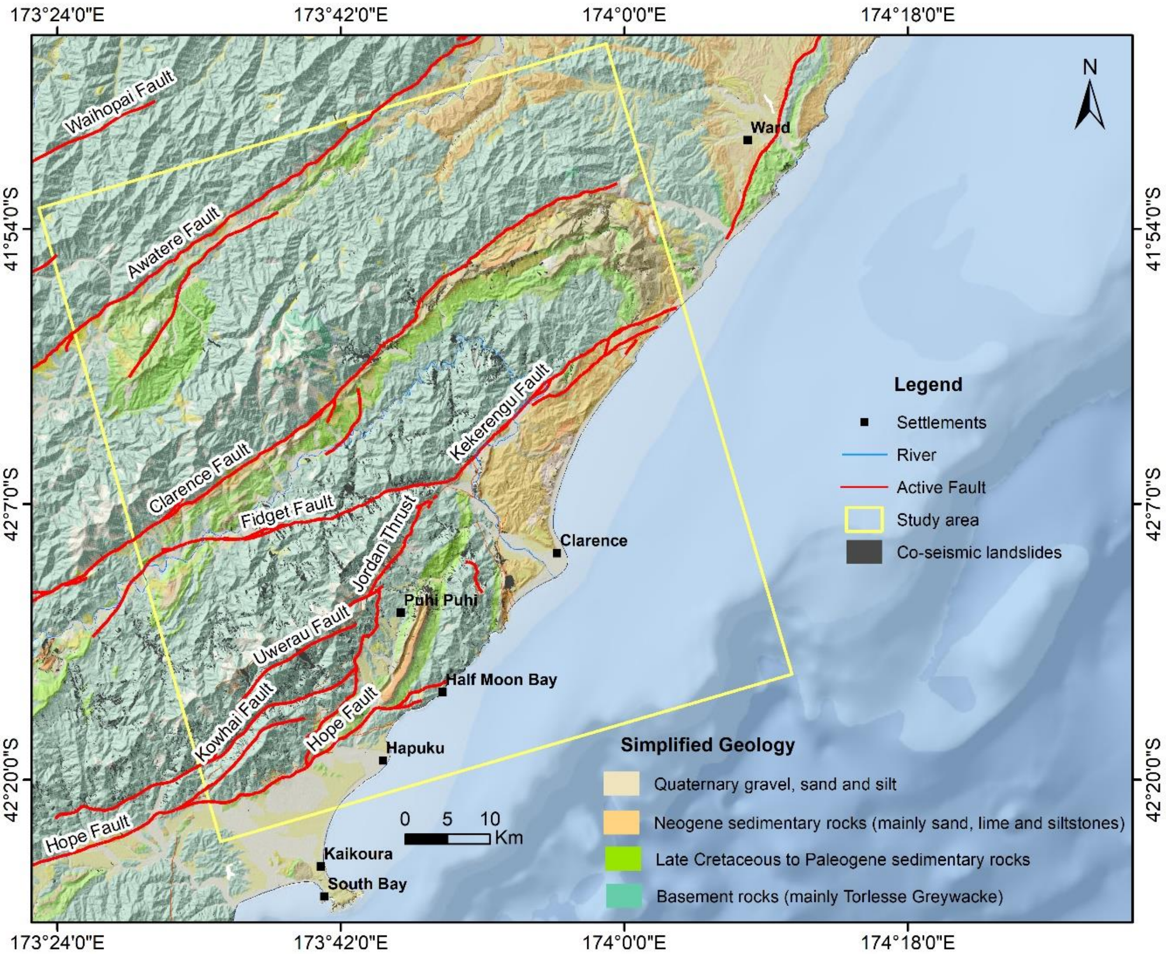

Figure 8. Simplified geology of the region investigated. Co-seismic landslide polygons are overlayed above the geological units.

3.4. Climatic setting

As per Koppen-Geiger classification, the region of study comes under the Marine West Coast climate with moderate winter and summer accompanied by copious yearly rainfall (Beck et al., 2018). The climate of this region is largely influenced by the Southern Alps mountain range. The average rainfall of the study area is about 838 mm/yr based on an analysis of 41 years of CHIRPS[9] Pentad data (Figure 9).

[9] Climate Hazards Group InfraRed Precipitation With Station Data (Version 2.0 Final)

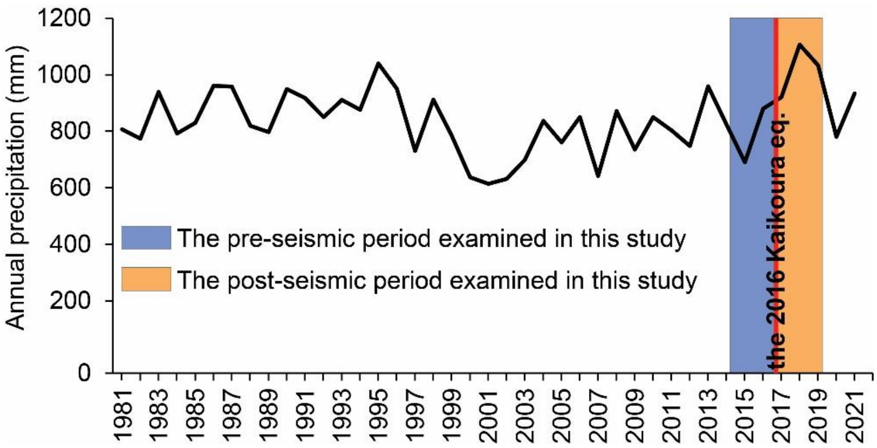

Figure 9. Total annual rainfall data between 1981 and 2021. From this graph, it can be observed that 2018 had the maximum amount of annual rainfall in last 30 years.

January is the warmest month of a year, while June, July and September are the coldest month owing to the snowfall. Figure 10 present the monthly average precipitation of the study area from 2014 to 2018 calculated using GPM[10] product.

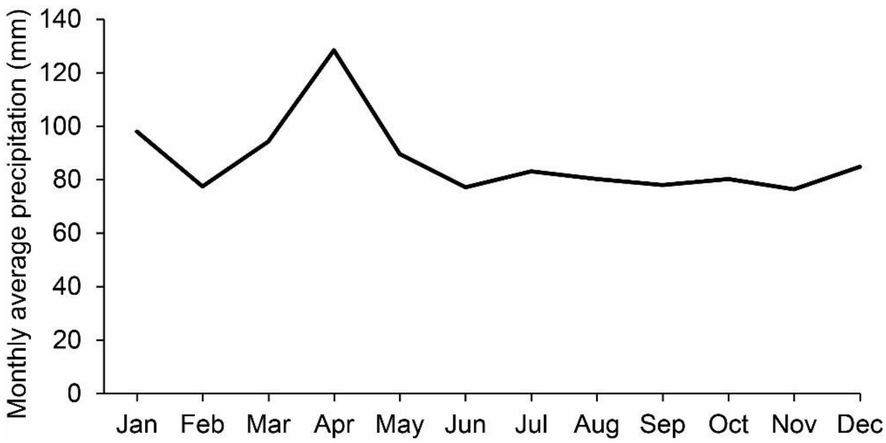

Figure 10. Average monthly precipitation (mm) of the study area between 2014 and 2019. The selection of this four years, in particular, is in line with the occurrence of the 2016 Kaikōura earthquake. From this bar graph, it is understood that the month of April received a relatively higher monthly average precipitation between 2014 and 2019.

3.5. Soil setting

The north-eastern part of New Zealand's southern island comprises six major soil types, including Brown soils, Melanic soils, Gley soils, Pallic soils, Recent soils, and Raw soils (Figure 11). Nearly half of New Zealand is covered by Brown soils, and they are mostly seen in mountainous regions. This type of soil remains wet and moist throughout the year. Unlike other soil types, Brown soils are highly weathered. Both Pallic soils and Brown soils are poor in iron oxide, which is an important material that makes the soil stable. Pallic soils are wet during the winter season and dry during summer. Next in the list of soils that cover the study area is Raw soils which are commonly present in region highly susceptible to erosion and dynamic sedimentation.

[10] Global Precipitation Measurement v6

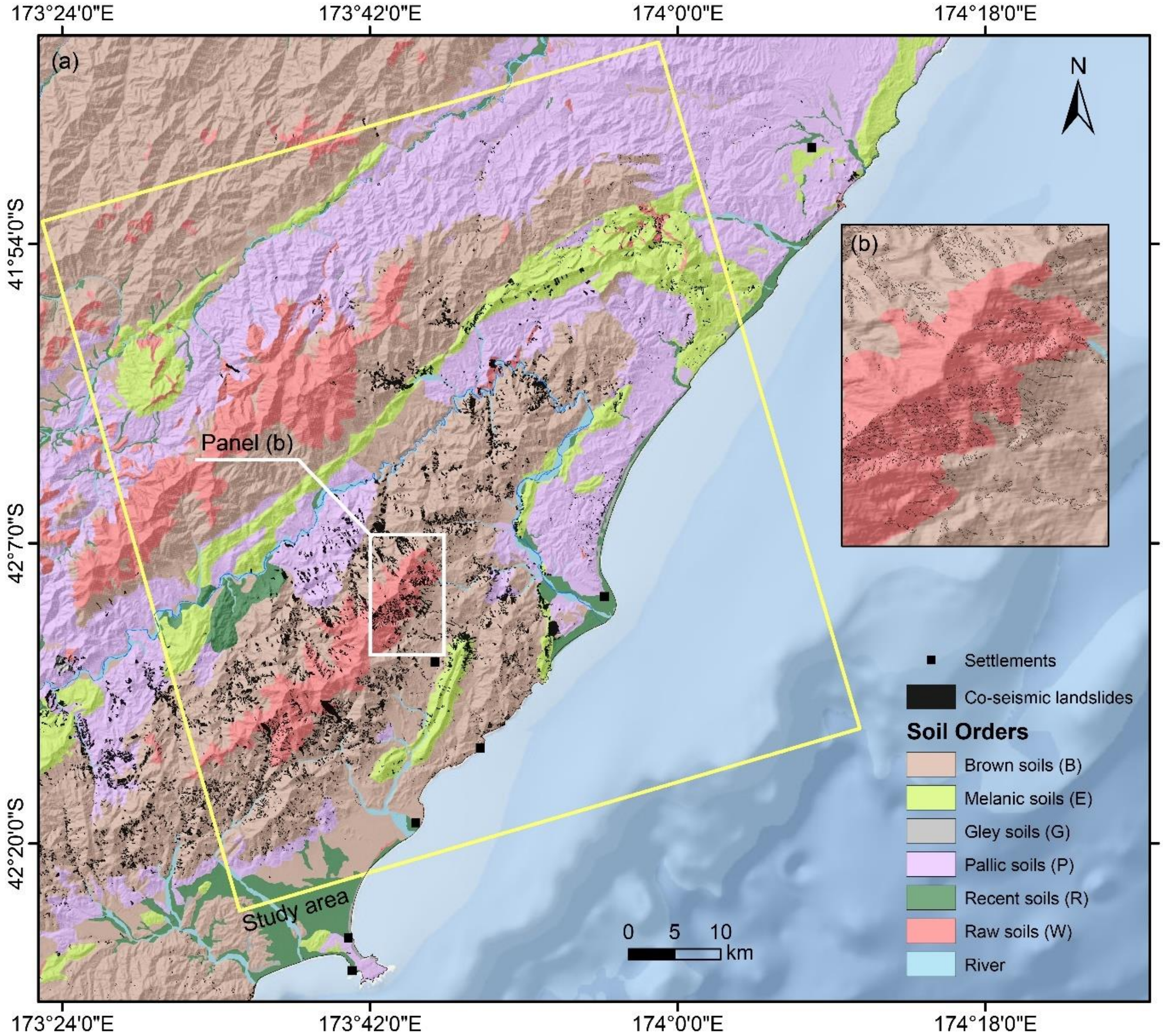

Figure 11. Soil orders of the study area.

3.6. Sentinel-1 SLC data

Considering the availability of data (see Table 2), freely accessible C-band Terrain Observation with Progressive Scans SAR (TOPS) based Sentinel-1 Interferometric Wide (IW) beam mode SLC SAR product having a swath width of 250 km is suitable for performing pre- and post-seismic deformation dynamics analysis of hillslopes present in the study area. The mission is run by European Space Agency, and the dataset can be freely downloaded from the ASF data search vertex (link).

Since the Kaikōura earthquake happened on 14 November 2016, 90 Sentinel-1 SLC datasets available between October 2014 and December 2018 in descending direction (path 154) are acquired (Figure 13). Since the count of persistent scatterers decreased over time owing to different decorrelations (Braun et al., 2020), the analysis period was split into two intervals of about two years interval as shown in Figure 12. This selection of periods also represents the pre-Kaikōura and post-Kaikōura phase, which is separated by the 2016 Kaikōura earthquake.

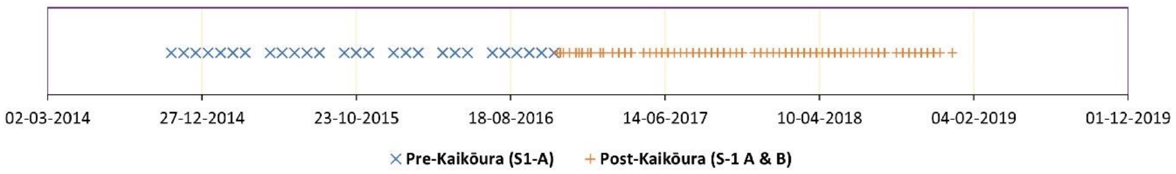

Figure 12. Distribution of examined Sentinel-1 images over time for pre-Kaikōura (x-marks in blue) and post-Kaikōura periods (Plus signs in orange) in ascending direction.

There are two satellites Sentinel-1 A and B, active from 2014 and 2016, which have 12-day repeat cycle. Thus, generally, when both data products are considered, the images can be acquired with 6 day repeat interval. However, for the study area considered in this work, the interval between two images majorly varies between 24 and 48 days in the case of the pre-seismic period, while the interval becomes shorter with most images acquired between an interval of 12 and 6 days in the post-seismic period. The number of Sentinel-1 images, along with their path and frame, are presented in Table 4.

In a standard setting, deformation acquired in LOS direction from both ascending and descending directions are integrated to calculate the north-south and east-west motion (Balbi et al., 2021; Blasco et al., 2019; Cigna et al., 2021; Mancini et al., 2021; Shankar et al., 2022). Unfortunately, only very few descending images are present during the pre-Kaikōura and post-Kaikōura period. During the pre-Kaikōura phase, there are only 12 descending image available and in the post-Kaikōura phase no images are available between December 2016 right after the event till June 2018. Then, the 3D decomposition by combining ascending and descending SAR data is not practically feasible.

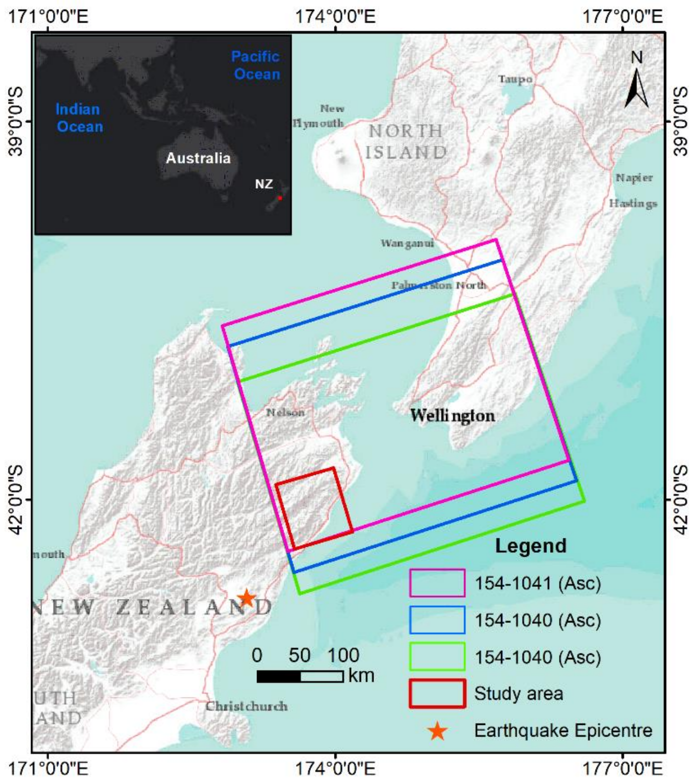

Figure 13. The frame and path of Sentinel-1 images used in this study.

Table 3. Details of Sentinel-1 data utilised in this study.

Period	Sensor	Direction	Pol.	Path	Frame & Image count	Start date/End date	Total number of images
Pre-Kaikōura	S-1A	Ascending	VV	154	1040 (14)	28-10-2014 to 10-11-2016	27
					1041 (13)		
Post-Kaikōura	S-1A	Ascending	VV	154	1041 (4)	16-11-2016 to 24-12-2018	63
	S-1B				1040 (3) & 1041 (56)		

3.7. Generic Atmospheric Correction Online Service for InSAR (GACOS) data

This research uses GACOS dataset provided by Newcastle University for eliminating the atmospheric delays caused due to water vapours. This dataset is generated using existing high resolution numerical weather model such as ECMWF[11] and Digital Elevation Model (DEM). The Zenith Tropospheric Delay (ZTD) products are downloaded as a binary grid by providing region of interest and the Sentinel-1 acquisition date and time (UTC).

3.8. Co-seismic landslide inventory

In this study, polygon-based co-seismic landslide inventory generated by Tanyaş et al. (2022a) is used to identify the slope units that failed during the earthquake. The landslide mapping was carried out using the pre- and post-Kaikōura Sentinel-2 images having a spatial resolution of 10 m. More than 14,000 landslides were mapped over the earthquake-affected region of about 14,000 km^2. Nearly 7,159 landslides fall into the study area considered in this research. Out of 101 landslide dams[12] triggered by the earthquake, 49 lies within the study area. Thus, the region considered in this study, which extent around 2300 km^{2,} nearly covers half of the co-seismic landslides that occurred during the 2016 earthquake.

3.9. Digital Elevation Model (DEM)

DEM helps in extracting some of the important topographic features, such as slope, aspect which can be used for deriving slope units and performing sensitivity and visibility analysis (López-Vinielles et al., 2021; van Natijne et al., 2022). In this study, void-filled Shuttle Radar Topography Mission (SRTM) DEM of 1-arc second global, resolution equal to ~30m, acquired from USGS Earth Explorer (link) is used.

3.10. Rainfall

For this study, daily rainfall data is acquired from the Climate Hazards Group InfraRed Precipitation with Station (CHIRPS) version 2.0 final dataset, which has a spatial resolution of 0.05 degrees and covers latitudes between 50 degrees (Funk et al., 2015). CHIRPS dataset is chosen for this study owing to its high spatial resolution of ~5km than that of GPM and TRMM which have a resolution of ~10km.

[11] European Centre for Medium-Range Weather Forecasts

[12] Landslide Dam is a type of slope failure which interrupts the flow of a river or drainage network and forms a natural temporary dam like barrier which gets eroded over the time.

4. METHODOLOGY

The complete research workflow of this study is presented in Figure 14. Overall, the methodology consists of six steps: a) pre-processing of PSI (single prime interferogram formation), b) PSI processing, c) decomposition of LOS deformation to downslope deformation, d) detection of actively deforming PS points, e) analysing the spatial distribution of PS across different landscape characteristics, e) identifying active hillslopes during pre- and post-seismic phase, f) examining the sub-meter hillslope evolution based on proposed post-seismic hillslope deformation scheme, and g) investigating the evolution types using deformation time series along with visual examination of daily precipitation.

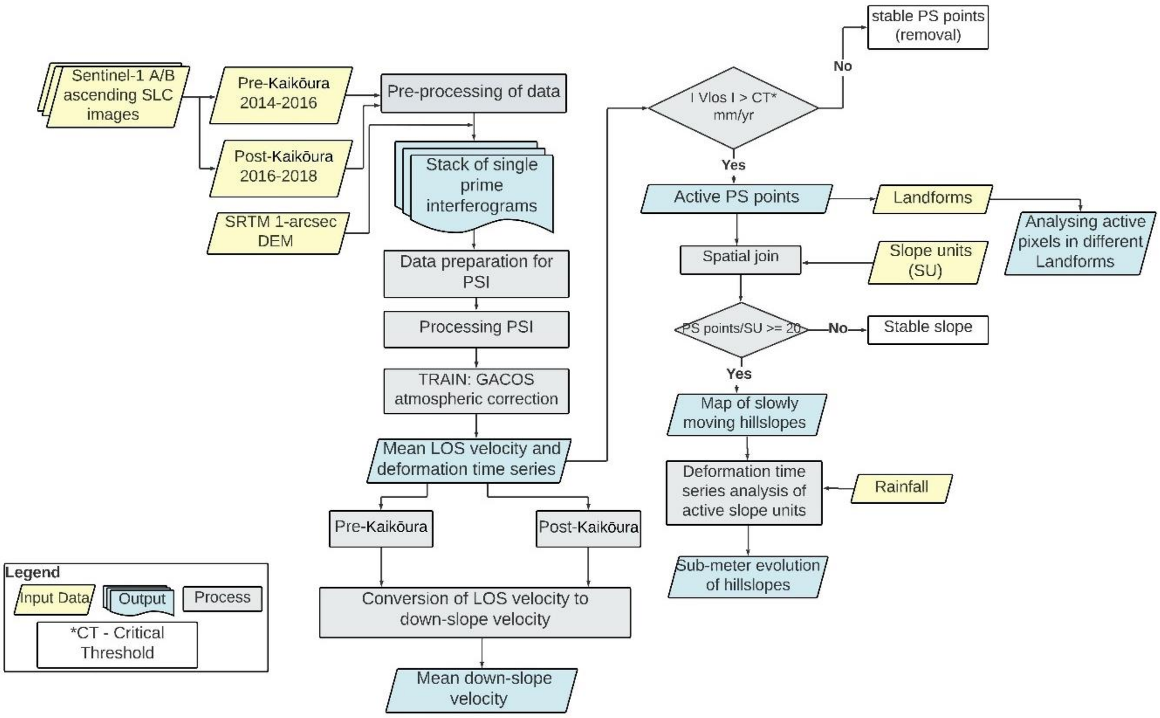

Figure 14. General synopsis of the methods.

4.1. Surface deformation extraction

The detailed workflow carried out to extract surface deformation from the Sentinel-1 SLC dataset with VV polarization, including pre-processing and processing stages of PSI, is presented in Figure 15.

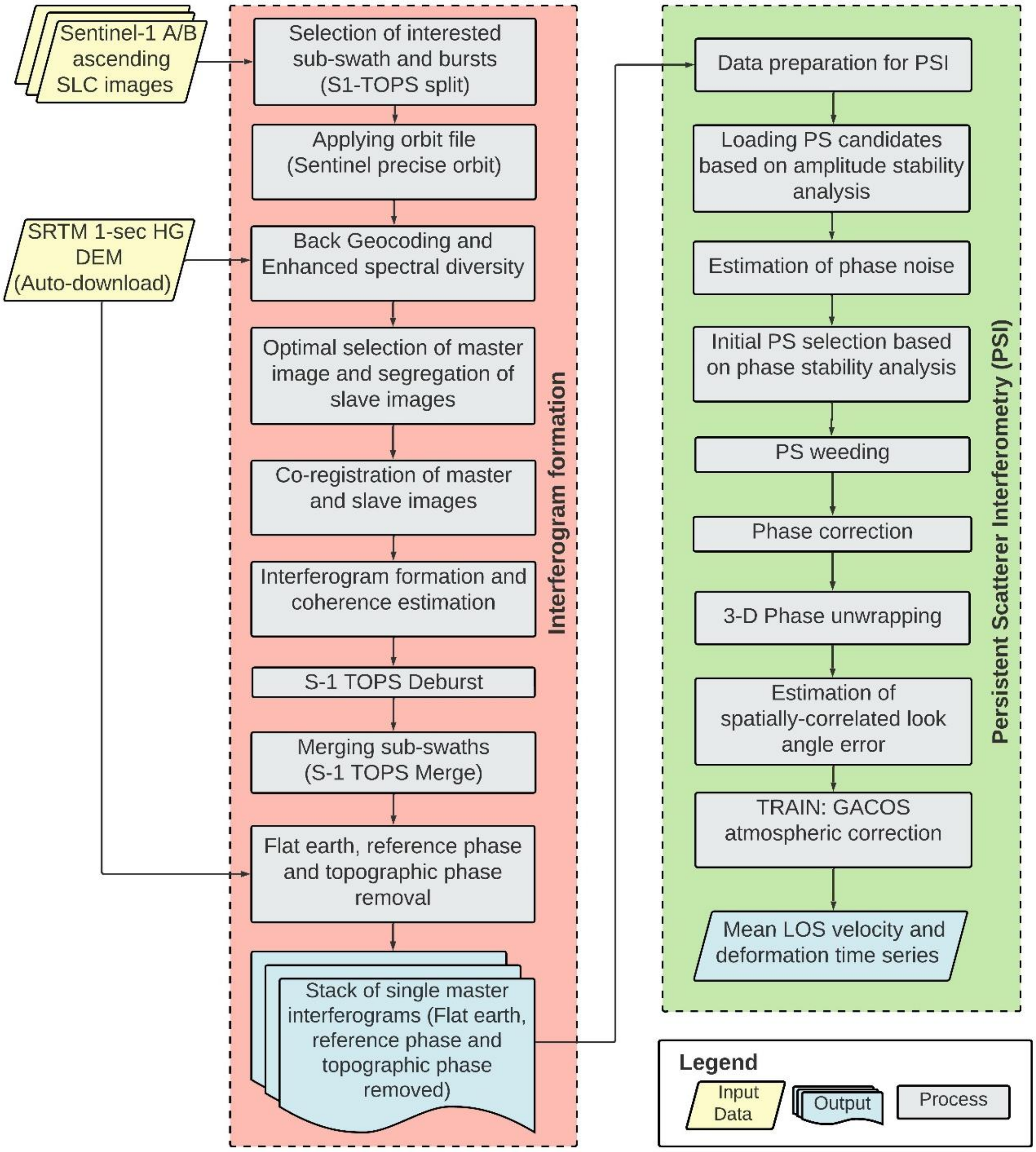

Figure 15. Comprehensive flowchart for retrieval of surface deformation.

4.1.1. Pre-processing (Single-prime interferogram formation)

In this research, for the automated generation of Sentinel-1 single-prime interferograms, the open-source SNAP2StaMPS python tool developed by Blasco et al. (2018) is used, which repeatedly calls the graphs created from the graph processing tool (GPT) of SentiNel Application Platform (SNAP version 8.0.0). This python-based SNAP2StaMPS tool is implemented in the Jupyter Notebook IDE[13] on a 32 vCPU Intel ×86-64, 768 GB RAM, NVIDIA RTX A4000 GPU computing unit.

Initially, an ideal complex-valued reference image is chosen for pre-Kaikōura and post-Kaikōura from the mid-point of the time-series analysis in a way that the perpendicular baseline distance between reference and

[13] Integrated Development Environment

secondary images is minimum as feasible, and coherence of the single-prime interferograms remain high. In addition, it is made sure that the selected reference image is not much affected by the atmospheric interference from rainfall and snowing as it might reduce the coherence of the generated interferograms (Zebker and Villasenor, 1992). Hence, two reference images, one for pre-Kaikōura acquired on 29 September 2015 and another sensed on 18 October 2017 for post-Kaikōura, are selected (Figure 16).

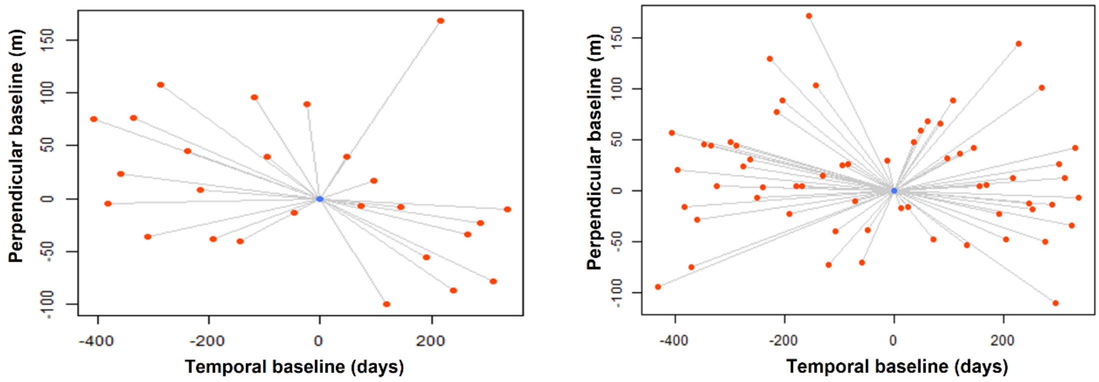

Figure 16. Baseline graph of two phases (pre-Kaikōura and post-Kaikōura) described in this research. Location of the Sentinel-1 TOPSAR sensor and sensed dates are presented in relation to the reference image.

Normally, Sentinel-1 images have three separate sub-swaths, containing nine or ten burst files per sub-swath. Each sub-swath has to be processed separately for co-registration since even a minimal problem in co-registration would result in an unrealistic phase surge in neighboring burst interferograms (Duan et al., 2020). In this study, sub-swath 1 (IW1) and burst 1 to 3 covering the study region are selected for splitting using the Sentinel-1 TOPS split tool in SNAP. Following this precise orbit (AUX_POEORB) files are automatically downloaded and applied to eliminate orbit errors related to the position of the satellite while acquiring the images. Both the steps are applied to all the images, including reference and secondary ones. This process of image splitting and applying orbit files is carried out with the help of graph presented in Figure 17.

Figure 17. Splitting sub-swath and applying orbit file.

After which, co-registration (Coreg) of stored single burst reference and the secondary image is performed, resulting in interferograms (Ifg). The co-registration step requires the implementation of back geocoding and Enhanced Spectral Diversity (ESD) enhancement to attain maximum coherence. The back geocoding is known as initial co-registration, and ESD is called fine co-registration. Complex-valued SAR pixels are converted to a cartesian reference system during initial co-registration. Applying orbit files aids in proper initial co-registration between reference and secondary images. Subsequently, the ESD approach is utilized to eliminate further errors in the co-registration of reference and secondary burst images (Fattahi et al., 2017; Prats-Iraola et al., 2012). In this way, all the secondary images are co-registered to a single-reference image, forming a stack of co-registered single prime interferogram stacks. Totally, 26 single-prime interferograms for pre-Kaikōura and 62 for post-Kaikōura are generated using the graph created from the GPT of SNAP (Figure 18). Once the co-registration is performed, the Sentinel-1 TOPS Deburst method combines the neighboring bursts in generated interferograms. In order to maintain the highest resolution and, more significantly, not to average the coherent scatterers, no multi-look has been applied while creating interferograms.

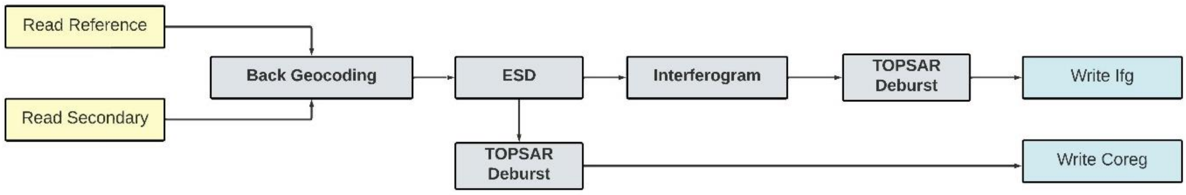

Figure 18. Co-registration (Coreg) of reference and secondary images and interferogram (Ifg) formation.

Then, the flat earth and topographic phase elimination are performed with the help of automatically downloaded Shuttle Radar Topography Mission (SRTM) 1 arc-sec HG DEM. The output from this step includes a topographic phase eliminated stack of single prime interferograms along with ortho-rectified latitude and longitude coordinates and altitude band utilised for further processing of PSI (Blasco et al., 2019).

Further processing of PSI is accomplished by exporting the co-registered stacks of single prime interferograms and topographic phase removed interferogram stacks using the StaMPS export tool in SNAP (Foumelis et al., 2018, Figure 19).

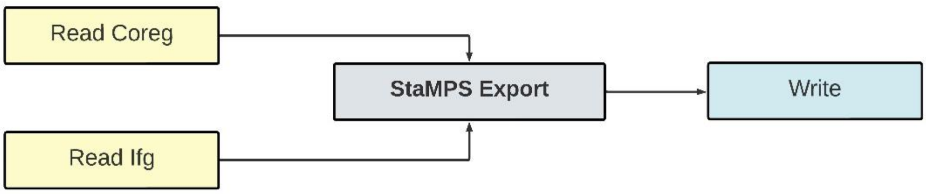

Figure 19. Export of single prime interferogram stack for StaMPS based PSI processing.

4.1.2. PSI processing

In this research, the Stanford Method for Persistent Scatterers (StaMPS) version 4.1b scripts for Matlab created by Hooper et al. (2018) were used to extract surface deformation time series from the exported single prime interferogram stack from SNAP. The default parameter configuration of StaMPS implementation doesn't always generate good quality results owing to the different natural settings of the study area. In order to achieve convincing deformation outputs, parameters for PSI StaMPS processing have to be configured (Balbi et al., 2021). StaMPS consists of 7 steps, from data preparation and loading for PSI processing to estimating spatially-correlated look angle error (SCLA, see Figure 15).

In this study, the different parameter configuration is tested to acquire the best deformation results. Experiments are carried out on a Ubuntu 20.04.4 LTS[14] based virtual computing unit (32 vCPU Intel ×86-64, 768 GB RAM, NVIDIA RTX A4000 GPU). The most significant PSI processing parameters that are used in this study after multiple iterative experiments for extracting deformation time series are presented in Table 4.

[14] Long Term Support

Table 4. Appropriate parameters employed in this research.

Parameter	Associated StaMPS Script	Step in StaMPS	Standard values	Period: Pre-Kaikōura (asc)	Period: Post-Kaikōura (asc)
Total Sentinel-1 scenes		-	-	23	67
Amplitude dispersion index (ADI)	mt_prep_snap	1	0.4 – 0.42	0.42	0.42
Maximum accepted uncorrelated DEM error (max_topo_err)	max_topo_err	2	5 m	20 m	20 m
CLAP[15] filter window size	clap_win		32	32	32
Maximum acceptable random phase density	density_rand	3	20 km^{-2}	20 km^{-2}	20 km^{-2}
Acceptable threshold standard deviation for weeding pixel	weed_standard_dev	4	1 – 1.2	1.2	1.2
Weeding neighbouring pixel	weed_neighbours		No	Yes	Yes
Weeding pixel lying in areas having zero elevation	weed_zero_elevation		No	Yes	Yes
The size of unwrapping grid	unwrap_grid_size	6	200	50	50
Size of the Goldstein filter's window	unwrap_gold_n_win		32	16	16
Smoothing window (in days)	unwrap_time_win		730	365	365
Estimation of phase ramp	scla_deramp	7	No	Yes	Yes
Filter that is applied spatially	scn_wavelength	8	100	50	50
Filter that is applied temporally	scn_time_win		365	50	50
For eliminating tropospheric errors	subtr_tropo		No	Yes	Yes
The technique used for atmospheric delay correction	tropo_method		'a_l'	'a_gacos'	'a_gacos'
Reference longitude and latitude	ref_centre_lonlat	-	-	173.69, -42.039	173.69, -42.039
Reference radius	ref_radius		-	100 m	100 m
final density of PS per km^2	-	-	-	109.65	58

Initially, phase stability is determined with the help of amplitude dispersion index (ADI) for recognising candidate PS pixels having a constant phase signal over noisy random phase across the analysed period (Hooper, 2008). Since Kaikōura is a mountainous terrain with vegetation and bare rocks, the maximum acceptable threshold of ADI was increased from standard 0.4 to 0.42 in order to have more candidate PS pixels. Subsequently, random phase noise for every candidate pixel presenting in the single prime interferogram stack is estimated in the second step (Hooper et al., 2007). Scattering from different objects on the Earth surface lying within the same pixel generates phase noise which is sorted by employing iterative CLAP filter. By doing so, coherence of the candidate PS pixel is determined through time, which aids in determining PS pixel. In addition, DEM error is estimated and eliminated in this step by setting a maximum threshold for DEM error. In this study, the standard acceptable 5 m DEM error is increased to 20 m as the study area is a hilly terrain.

[15] Combined low-pass and adaptive phase filter

Following this, the maximum acceptable random phase density is fixed to 20 km^{-2} for having at least 20 random phase pixels per km^2. Consequently, the pixels with high random phase are eliminated by setting a threshold of standard deviation for random phase and neighbouring pixels arising from a similar DS having identical phase noise are weeded. In this study, the maximum acceptable standard deviation for weeding random phase was set to 1.2. In addition, the random phase in regions with zero altitude is eliminated since this study focuses on hillslopes.
This step is followed by phase correction, wherein the SCLA DEM errors are fixed. Consequently, unwrapping of the wrapped phase between $-\pi$ and $+\pi$ is carried out in three dimensions (i.e., spatially two dimensions and temporally one) to extract a unique phase. Following this, SCLA errors arising from DEM, the orbit of satellite, and phase ramps are estimated and removed.

Finally, the influence of the elevation-dependent atmospheric phase is eliminated by carrying out atmospheric correction using Toolbox for Reducing Atmospheric InSAR Noise (TRAIN). Since the considered study area is large (2300 km^2), the phase-based linear atmospheric correction doesn't control the influence of atmospheric phase that too especially in the complex hilly terrain such as Kaikōura (Bekaert et al., 2015). Hence, the GACOS dataset is employed in this study for eliminating the atmospheric delay. The phase delay caused by atmospheric errors is computed for each interferogram using the wavelength and look angle of the Sentinel-1 images (Karanam et al., 2021). This phase delay is then subtracted from each interferogram.

4.2. Projection from V_{LOS} to V_{Slope}

The deformation result extracted from PSI processing is available in sensor geometry as the LOS deformation vector, which is a one-dimensional representation of Earth surface deformation occurring in three-dimension (Hanssen, 2001). By combining the LOS deformation vectors of PS pixel observed in both ascending and descending images, horizontal and vertical deformation vectors can be obtained by decomposition (Blasco et al., 2019). The velocity in the LOS direction can be rewritten as a summation of vertical, east, and north velocity as follows (Hanssen, 2001):

$$\mathrm{V_{LOS}} = \mathrm{V_{East}} + \mathrm{V_{North}} + \mathrm{V_{Vertical}} \tag{9}$$

Since no descending images are available for the same period as ascending scenes, projecting one-dimensional LOS deformation to horizontal and vertical deformation is not possible in this study. Otherwise a harsh assumption must be made. For instance, by projecting LOS deformation onto the steepest direction along the slope (Aslan et al., 2020; Notti et al., 2014; Teshebaeva et al., 2019; Yi et al., 2022). As such, the movement in non-slip direction is assumed to be marginal. Naturally, due to gravity, materials on the hillslope tend to move downslope and especially this is widely assumed for translational landslides wherein the displacement occurs parallel to the slope (Bianchini et al., 2013). Therefore, in this study, we make an assumption that materials on the hillslope displace downslope in the steepest direction (Figure 20), and the projection from LOS to the downslope direction is carried out using the following equation (Notti et al., 2014):

$$V_{Slope} = \frac{V_{LOS}}{C} \tag{10}$$

Where V_{Slope} is downslope velocity and C is the factor that provides info on the amount of downslope displacement (Notti et al., 2014). Factor C is estimated as follows (Aslan et al., 2020):

$$C = N \times (\cos(S) \times \sin(A - 90^o)) + E \times \left(-1 \times (\cos(S) \times \cos(A - 90^o))\right) + H \times \left(Sin(S)\right) \tag{11}$$

Where S is the slope and A is the aspect derived from SRTM 1 arcsec DEM (~30 m) while the other parameters including N, E and H are estimated as follows:

$$N = \cos(90° - \alpha)\times\cos(180° - \gamma) \tag{12}$$

$$E = \cos(90° - \alpha)\times\cos(270° - \gamma) \tag{13}$$

$$H = \cos(\alpha) \tag{14}$$

where α is the satellite's heading azimuth and γ is the incidence angle.

In certain regions, the factor C can be zero, which will make downslope velocity infinity. To avoid such scenario, the value of C is set to 0.3 when the range of C is between 0 and 0.3 and to -0.3 while the value vary between -0.3 and 0 (Kalia, 2018).

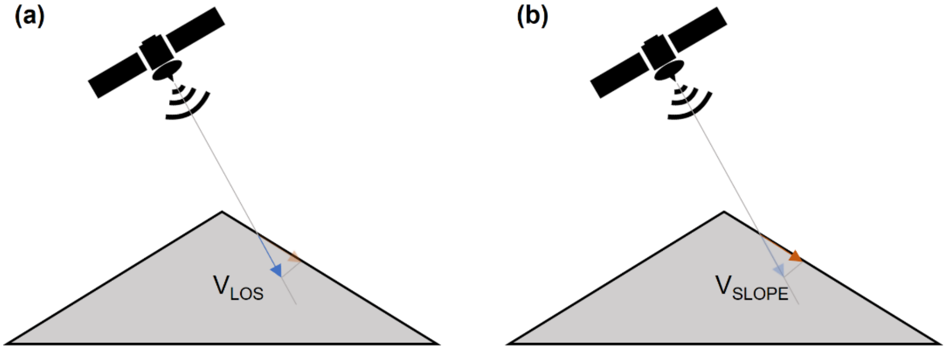

Figure 20. Deformation velocity projection. (a) LOS deformation velocity, and (b) Vslope deformation velocity

In this study, the conversion of V_{LOS} to V_{Slope} is performed using R and the workflow is presented in Figure 21.

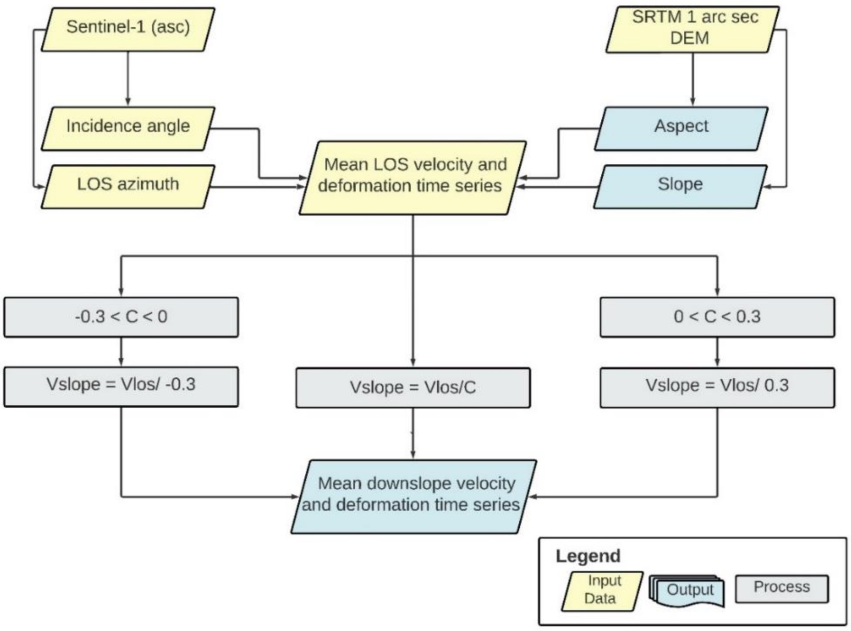

Figure 21. Projection of V_{LOS} to V_{Slope}. (asc: ascending)

4.3. Detection of actively deforming PS pixels

Following the generation of surface deformation time series with the help of the PS-InSAR technique, every single time series is methodically evaluated for discovering actively deforming points (Raspini et al., 2018). But analysing each time series manually would be a laborious task both in terms of time and computational effort, especially when the region under investigation is large. In order to overcome this problem, defining a critical stability threshold to the deformation velocity can aid in identifying those points that may be actively deforming. Also, by following such a procedure, stable points can be eliminated for further analysis, which reduces the burden on analysing deformation time series (Aslan et al., 2020).

For identifying actively deforming points, there are two commonly used method in literature: a) setting a critical stability threshold of either one or two standard deviation for PS velocity and b) using the hillslope velocity classification of Cruden and Varnes (1996). In the case of former method, those PS points whose absolute velocities are more than 1 or 2 standard deviations (σ) are considered 'active', and the rest are considered 'stable' (Aslan et al., 2020; Bekaert et al., 2020). In the latter method, for instance, Cigna et al., (2013) characterised those hillslopes having active deformation to be extremely slow-moving (-13 mm/yr $\leq V_{LOS} < 16$ mm/yr) and very slow-moving hillslopes ($V_{LOS} \geq 16$ mm/yr) based on Cruden and Varnes (1996) classification. Even though there is no lower threshold coined for extremely slow-moving hillslopes in Cruden and Varnes (1996) classification, the authors made an assumption in setting -13 mm/yr as the minimum threshold. Since the range of deformations is different in the case of pre-Kaikōura and post-Kaikōura phases, using σ as a critical stability threshold will result in points having different ranges of velocity being classified as active and stable. To avoid such confusions, in this study, I coupled both approaches summarized above to differentiate active PS from stable ones. As a result, I set the common critical stability threshold as 10 mm/yr. This assumption well align with the literature (e.g., 13 mm/yr in Cigna et al., 2013) and the dataset I examined in which the one standard deviation of mean LOS velocities from post-Kaikōura phase is 8.44 mm/yr. Therefore in this study, those PS having mean LOS velocity equal or greater than ±10 mm/yr are classified as active points, while the rest are excluded as they are stable. Moreover, this procedure can aid us in removing pixels that are affected by shadow effects (Bekaert et al., 2020). In addition, identified active PS are also sub-categorized as extremely slow-moving (± 10 mm/yr $\geq V_{LOS} < \pm 16$ mm/yr) and very slow-moving ($V_{LOS} \geq \pm 16$ mm/yr) PS (Cruden and Varnes, 1996) to characterise actively deforming slopes into extremely slow and very slow-moving hillslopes. This characterisation is elaborated in the Section 4.4.

4.4. Spatial distribution of PS over different landscape characteristics

A large number of earlier studies aim at revealing the relationship between rainfall and deformation in an area to understand the evolution of active deformations which are driven by rainfall (Bayer et al., 2018; Liu et al., 2022; Sun et al., 2015; Tong and Schmidt, 2016; Wang et al., 2022). In this research, the spatial distribution of PS across various landscape characteristics such as morphometric variables, seismic variable, and lithology are examined for understanding their association.

Detected active PS are only used for the analysis in the case of morphometric variable and lithology whereas the entire PS pixels are employed for the rest. Even though such analyses are common while examining spatial distribution of co- and post-seismic landslides but they are rarely available in the case of analysing sub-meter deformation measurements of hillslopes extracted from PSI approach. Thus, in this study, I would like to provide insights on this matter via simple bivariate analyses between our PS data and a number of environmental factors governing hillslope deformation.

4.4.1. Morphometric variables

The morphometric variables such as elevation and hillslope steepness are examined in relation to the entire PS that are obtained in this research during pre- and post-Kaikōura phases. These variables provide insights about the hillslope geometry and serve as an indicator in addressing the balance of stability factors acting on a hillslope (McColl, 2022). The void filled Shuttle Radar Topography Mission (SRTM) DEM of 1-arc second global having a spatial resolution of ~30m is used for extracting the elevation and slope steepness. In order to examine the entire PS with the altitude and slope steepness, multiple bins with equal space of 10 mm are generated using the mean annual LOS deformation velocity.

In addition, this research uses 'r.geomorphons' tool in the GRASS GIS (Jasiewicz and Stepinski, 2013) to generate various landform types to investigate if there is a prevalent occurrence of actively deforming PS across any landform elements (GRASS Development Team, 2021). This tool uses an automatic pattern-based categorisation technique that uses DEM as an input for generating different landform types. Given the large areal extent of the study area, various landforms are observed.

For classifying different landforms, local ternary patterns along with line of sight approach is employed (Ngunjiri et al., 2020). This approach helps to identify ten basic forms, including flat, peak, ridge, shoulder, spur, slope, hollow, footslope, valley and pit (Figure 22, Kramm et al., 2017).

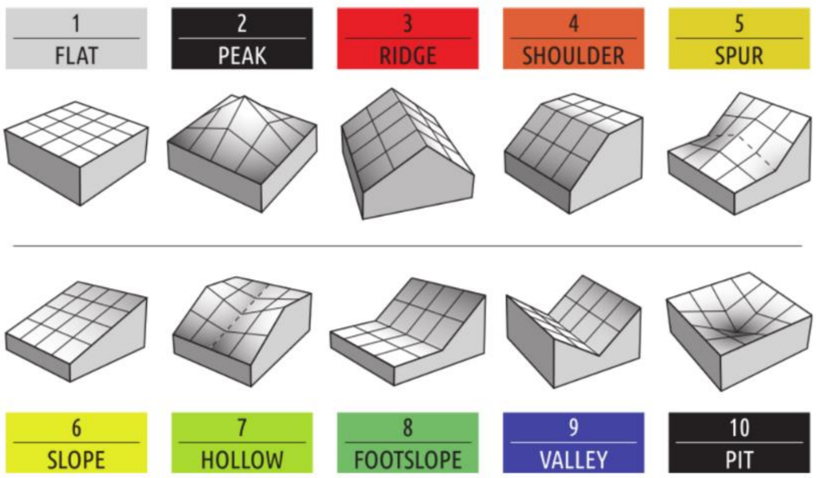

Figure 22. Representation of ten common landforms (Gruber et al., 2019).

4.4.2. Seismic variable

In this research, the PGA experienced during the co-seismic phase of the 2016 Kaikōura phase is examined with the PS showing the mean annual deformation velocity obtained during the post-Kaikōura phase. Such analysis is performed to understand the effect of PGA on post-seismic deformation. The entire PS is categorised into multiple bins having an equal space of 10 mm.

4.4.3. Lithology

The association between lithological control of actively deforming regions is rarely investigated in the literature. Such examination can help us understand and discover any geological formations that contribute to the active deformation. Xu et al. (2021) examined the lithological control of hillslopes in the entire western coastal region of the United States that are identified to have slow movement for understanding the influence of geology on them. Similarly, Bayer et al. (2018) investigated the influence of weak lithology on the slow-moving hillslopes in the Apennines. In this research, lithology of the study area obtained from the

LRIS[16] portal ((https://lris.scinfo.org.nz/) is utilized in examining the relationship between lithology and detected actively deforming PS in the entire region of interest.

4.5. Identifying and characterisation of slow-moving hillslopes

Once the active pixels are detected by setting a common critical stability threshold, the pixel clustering approach is commonly used for selecting those regions having a group of active pixels which aids in excluding single noisy pixels (Aslan et al., 2020; Bekaert et al., 2020). The drawback of this approach is that clustering techniques don't consider the discrete process of slopes. In addition, this approach is only useful while generating deformation time series with SBAS as it produces a large number of deformation pixels. Therefore, this study offers an alternative procedure wherein a topographic-driven approach is employed to identify slow-moving hillslopes using deformation velocity from PS pixels. This approach recognises the discrete movements of slopes, which includes the generation of slope units and further spatial analysis such as spatial join and boolean process for distinguishing slow-moving hillslopes.

4.5.1. Generation of slope units

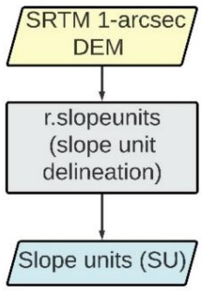

Figure 23. Workflow for generation of slope

Slope units are geomorphological topographic units which represent those regions that have similar slope and aspect (Alvioli et al., 2018). In other words, portions of terrain displaying homogeneity in terms of slope and aspect are preserved as a slope unit (Alvioli et al., 2016). These units represent what geomorphologist widely accept as a natural hillslope, and it is highly suitable for landslide related studies, including landslide mapping and landslide susceptibility modelling (Guzzetti et al., 2005). Earlier studies had aggregated a cluster of significant coherent scatterers lying on a hillslope that display active deformation to be slow-moving hillslopes rather than considering any terrain unit since processes that occur within a slope is mostly discrete (Bekaert et al., 2020). Even though slope units have been in use for landslide studies from 1988, it has been rarely used for identifying slowly moving hillslopes in combination with InSAR techniques (López-Vinielles et al., 2021). Thus, in this study, slope units are used to aggregate those coherent scatterers within a hillslope that are displaying active deformation. For delineating slope units, r.slopeunits developed by Alvioli et al. (2016) is used.

4.5.2. Spatial join and boolean process

After generating the slope units, the spatial join tool in Arcmap 10.8.1 is utilised to count the number of active PS pixels within a slope unit, which is a polygon. During the process, the target and join features are set to be the slope units and active PS pixel layers, respectively. Those active PS pixels which are entirely contained within a slope unit are counted, and one to one join operation is used. This creates a spatial join attribute for each slope unit, which contains the total number of active PS pixels contained within them. At this point, a PS threshold is defined to identify if a slope unit is slowly moving or not. Such an approach increases the reliability that the active deformation of PS is associated with hillslope processes and is not because of any individual unstable structures (Notti et al., 2014). In literature, atleast three to five actively deforming PS is utilised for identifying a slow-moving hillslope (Cigna et al., 2013; López-Vinielles et al., 2021; Pawluszek-Filipiak et al., 2021). However, in this study, we safely assume that those slope units which contains ≥ 20 active PS are classified as slow-moving hillslopes rather than using 3 or 5 PS as a threshold. This ensures high reliability on capturing the slope processes, and those slope units having lower PS are marked as stable. In addition, the slow-moving hillslopes are further classified into extremely slow-moving (± 10 mm/yr $\geq V_{LOS} < \pm 16$ mm/yr) and very slow-moving hillslopes ($V_{LOS} \geq \pm 16$ mm/yr). If a slope unit

[16] Land Resource Information System (LRIS)

consists PS of both the classes, the mean of the average annual LOS deformation velocity for the entire hillslope is considered.

4.6. Proposal of post-seismic hillslope deformation matrix

In order to define the different state of sub-meter hillslope deformation activity before and after the Kaikōura earthquake, following two-dimensional post-seismic hillslope deformation matrix is implemented in this study (Table 5). The mean annual LOS deformation velocity of the entire hillslopes is used to define the state of activity of a hillslope. More complicated version of the PSI deformation-based activity matrix has been implemented in earlier studies such as Bianchini et al. (2012), Cigna et al. (2013), and Righini et al. (2011). However, these activity matrix proposed in earlier studies requires the multi-temporal landslide inventory to understand the long-term activity of the hillslopes in order to properly classify them. But, in this study, we used a rather simple approach for defining four types of sub-meter hillslope deformation activity during pre- and post-earthquake periods.

It is assumed that four different types of hillslope activities can be captured with the help of the proposed activity matrix. The first type of activity is those hillslopes that are seen stable in the pre-seismic phase, which become active in the post-seismic period (Lacroix et al., 2014). The second type of activity can be actively deforming hillslopes that continues to deform actively after the large ground shaking experienced from the earthquake (Bekaert et al., 2020). Those actively deforming hillslopes that become stable during the post-seismic period are the third type of hillslope deformation activity. The ultimate type of hillslope deformation activity can be those hillslopes that remain stable during the pre- and post-seismic phases.

Table 5. Activity matrix of hillslopes during pre- and post-Kaikōura phase.

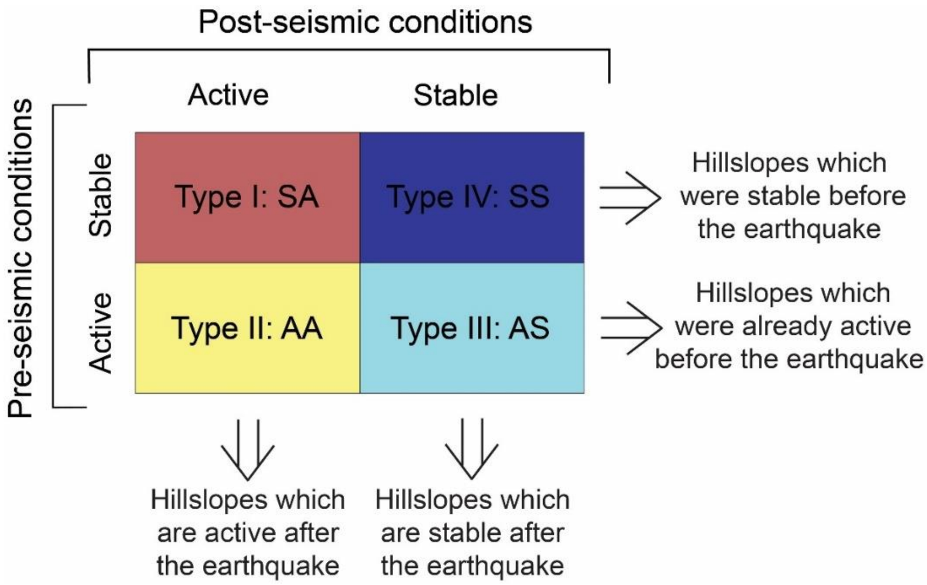

4.7. Analysing deformation time-series along with the visualisation of rainfall measurements

Once hillslopes having slow active deformations are identified, the deformation time series of such active slope units are analysed along with precipitation measurement in order to understand the impact of change in pore pressure and water table level on deformation evolution (Kang et al., 2021). In this study, the Google Earth Engine (GEE) is used to extract the daily precipitation from CHIPRS data (0.05 degrees spatial resolution) between the period of analysis (i.e., 2014 to 2018). Reducer function (ee.Reducer) from GEE is applied for obtaining the mean precipitation of interested slope units. The mean deformation of slope units, along with their standard deviation and daily mean rainfall measurement from CHIPRS data, is examined with the help of R, while some interesting individual active PS pixels are also visualised.

5. RESULTS

This chapter describes the outcomes that are obtained as a result of following the methodology stated above in chapter 4.

5.1. Mean annual LOS deformation velocity before the Kaikōura earthquake

The average annual LOS deformation velocity of the study area before the Kaikōura earthquake as a result of processing 26 Single prime interferogram stacks of Sentinel-1 between 28 October 2014 and 10 November 2016 ranges from -20.27 mm to 20.08 mm (Figure 24). It can be observed that the majority of the study area has a deformation between -5 mm/yr and 5 mm/yr in the pre-seismic phase, which is denoted by light green colour (Figure 24). These LOS velocities were calculated among 252,231 coherent PS pixels all over the study area. The positive values signify those regions of the study area moving toward the sensor, while those parts moving away from the sensor have a negative value. All the PS pixels are referenced to a stable region within the study area, denoted with a triangle symbol (see Figure 24).

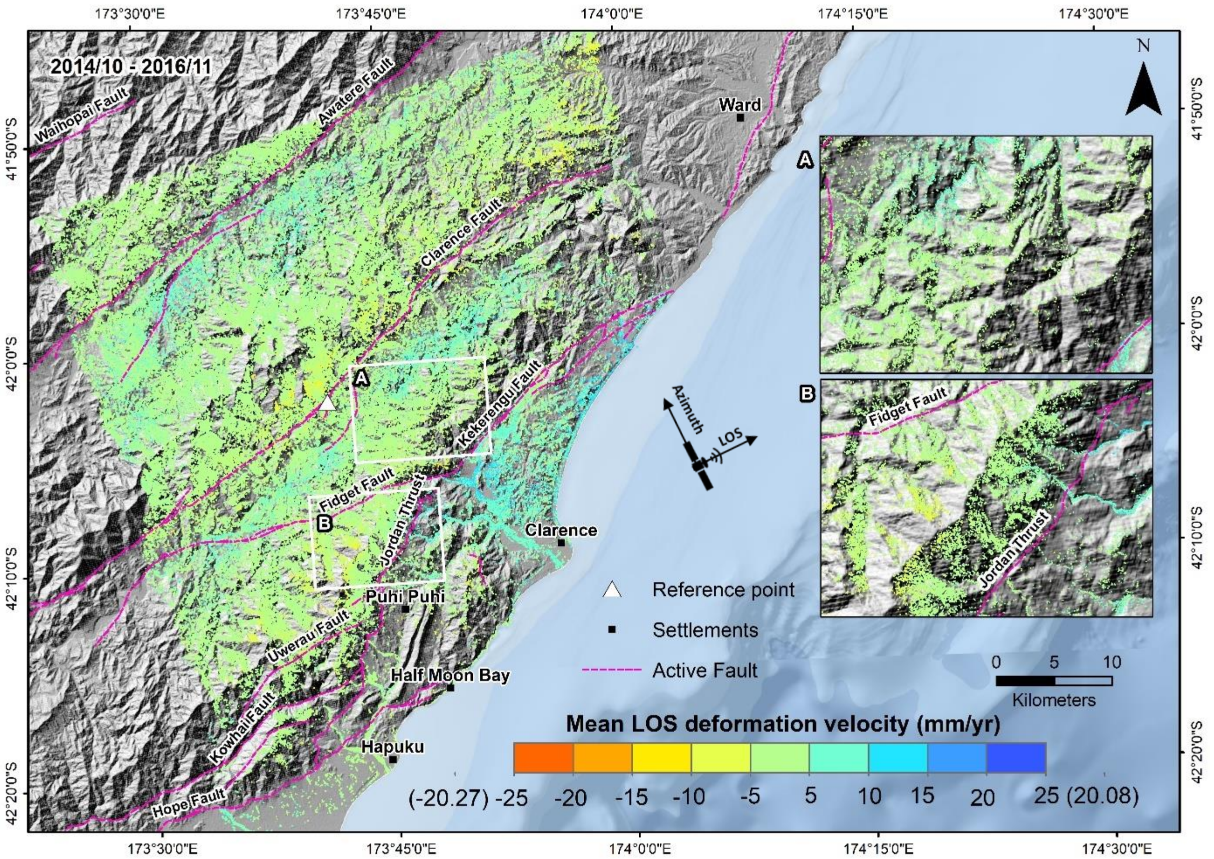

Figure 24. Mean annual LOS deformation rate expressed in mm is presented with the hillshade extracted from SRTM 1 arcsec DEM.

The mean and standard deviation of the average annual LOS deformation velocities calculated during the pre-seismic phase are 0.98 mm and 3.86 mm, respectively (Figure 25).

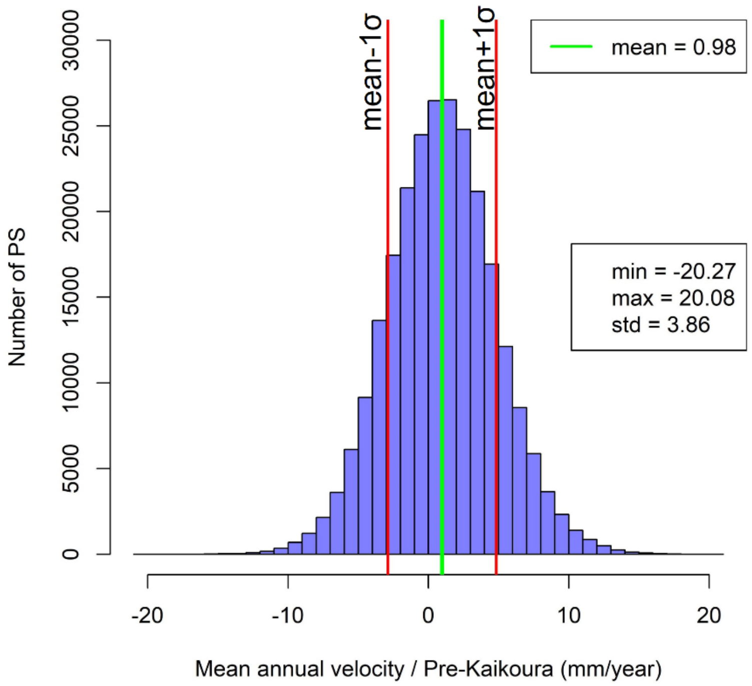

Figure 25. Normal distribution of mean annual LOS deformation velocity during the pre-Kaikōura phase. The green line represents the mean value while the red lines correspond to the one standard deviation from the mean on both negative and positive sides.

In order to understand the distribution of PS pixels during the pre-Kaikōura phase, different bins of mean annual LOS deformation velocity are generated and examined with the altitude and slope steepness. The PS pixels moving towards the sensor (20 to 30 mm/yr) and away from the sensor (-20 to -30 mm/yr) are noted to be present below 500 m of elevation and 20 degrees of slope (Figures 26a and b). Nearly 75% of PS having velocity of -10 to -20 mm/yr lies between 500 and 2000 m elevation with a slope steepness of 20 to 40 degrees (see Figures 26a and b). However, more than three quartiles of PS having a mean annual LOS deformation velocity of 10 and 20 mm/yr is observed in regions lower than 1000 m in altitude and within a slope steepness of 20 degrees (see Figures 26a and b).

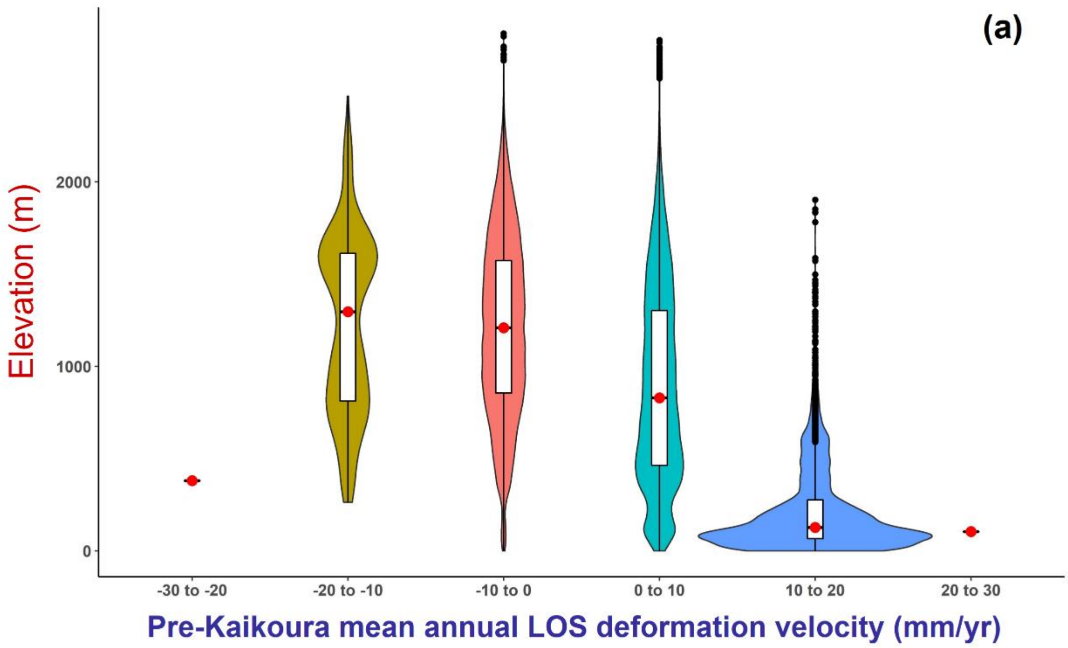

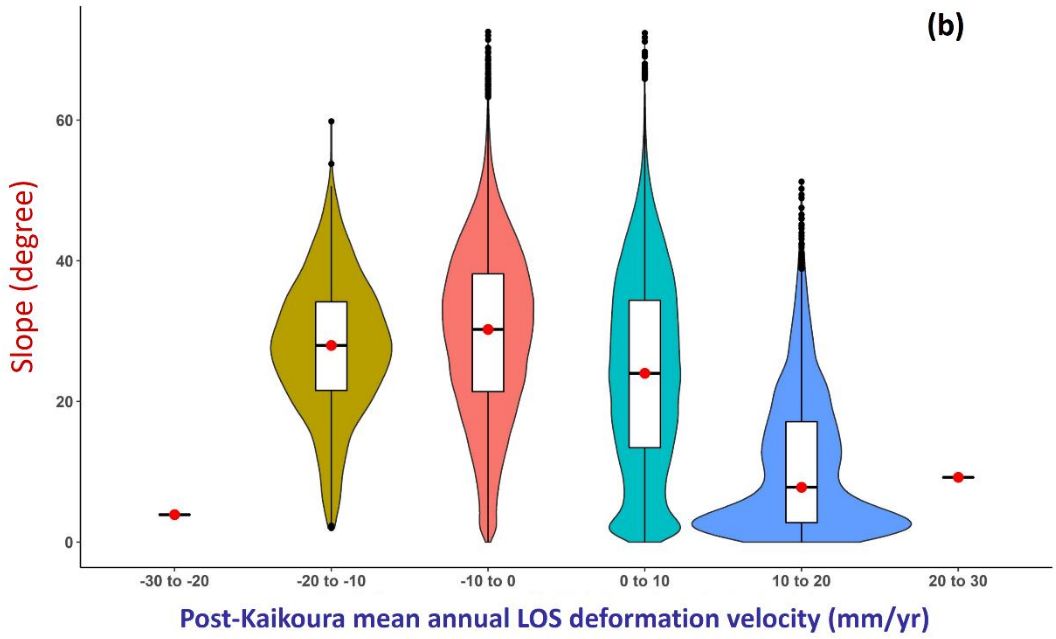

Figure 26. Violin plots depicting the variation of (a) elevation and (b) slope steepness in relation to different bins of mean annual LOS deformation velocity extracted for the period before the Kaikōura earthquake.

Figures 26 (a) and (b) show that pixels having active deformation (>|10|mm/yr or relatively high deformations) range in a relatively small interval compared to stable pixels (i.e., <|10|mm/yr). This implies that conditions governing the existing of actively deformed hillslopes are bounded by environmental variables, whereas stable hillslopes are spread all over the study area.

5.2. Mean annual deformation velocity after Kaikōura earthquake

The average annual deformation velocity of the study area after the 14 November 2016 Kaikōura earthquake until December 2018 ranges between -54.1 mm and 39.1 mm (Figure 27). Deformation from nearly 134,810 PS pixels is used in calculating this mean annual LOS deformation velocity after the earthquake. Two extreme deformations indicated with blue (Figure 27a) and red (Figure 27b) colour variations relating to movements away from the sensor and towards the sensor are noted in hillslopes north of the Kekerengu fault, and Jordan thrust fault, respectively.

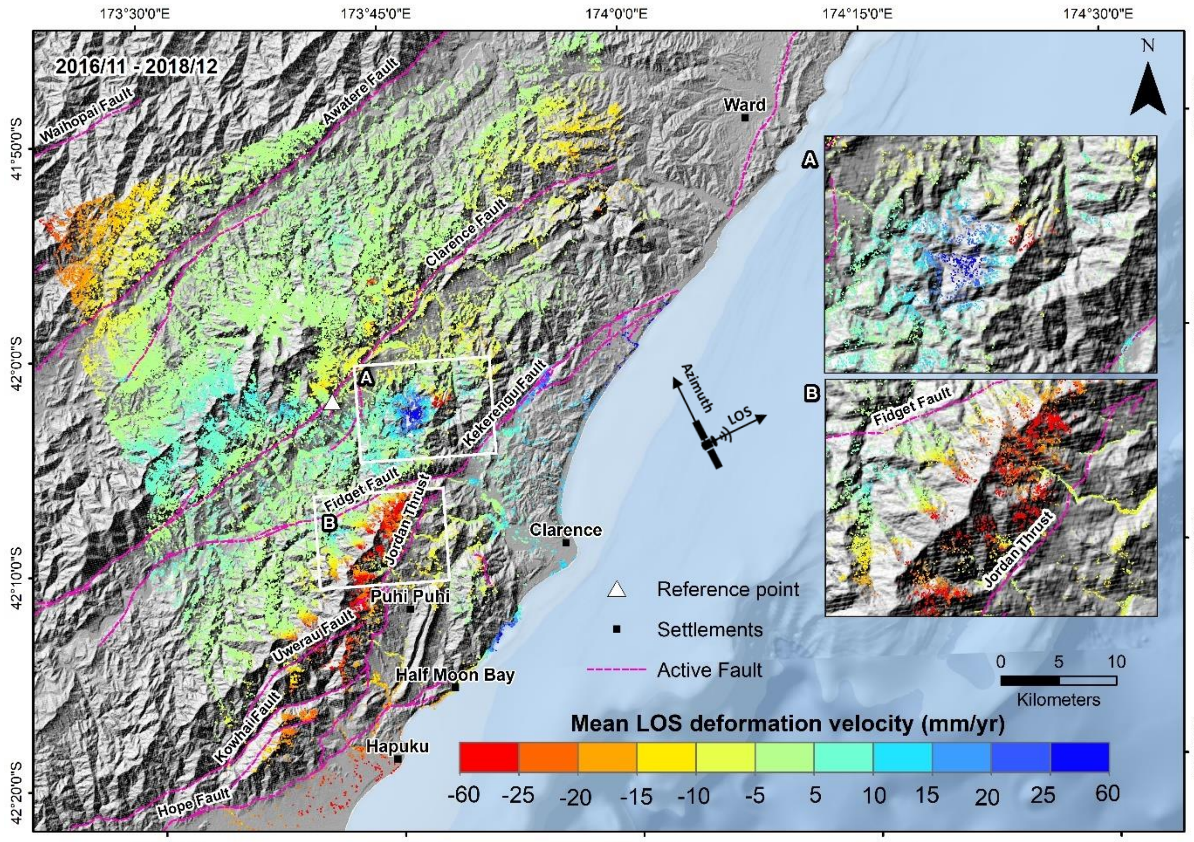

Figure 27. Mean annual LOS deformation velocity during the post-Kaikōura period (November 2016 – December 2018). The regions in darker blue (a) and red (b) denote the parts of the study area experiencing movement towards the sensor and away from the sensor, respectively.

The stable area chosen for reference in the Post-Kaikōura deformation analysis is the same as the pre-Kaikōura deformation analysis, which is denoted by a triangle symbol. The average annual LOS deformation velocity of the entire study area post-earthquake is around -1.41 mm, and the standard deviation is about 8.44 mm (Figure 28).

To understand the variability of PS pixels having different deformation rates, ten bins of mean annual LOS deformation velocity, each having a 10 mm interval, are created and investigated with elevation, slope steepness, PGA, and distance to fault rupture of the study area (Figure 29a, b, and c). Interestingly, PS experiencing an uplift of 20 to 40 mm/yr are observed in regions with elevations lower than 1000 m, yet the slope steepness differs between 0 and 60 degrees (see Figure 29a and b). Contrarily, the PS pixels experiencing subsidence higher than -40 mm/yr are noted in places with an altitude more prominent than 1000 m, and 75% of data lies in terrain having a slope of 20 to 40 degrees (see Figures 29a and b). Furthermore, the pixels having deformation between -10 and 10 mm/yr are seen all over the study area.

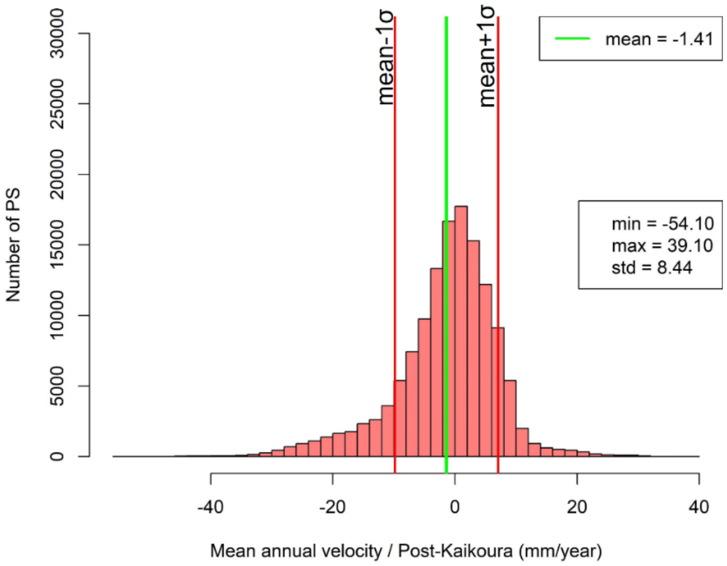

Figure 28. Normal distribution of mean annual LOS deformation velocity during the post-Kaikōura phase. The green dash line represents the mean, while the red line corresponds to the one standard deviation.

The PGA is not included in analysing the variability of pre-Kaikōura LOS deformation because ground shaking is experienced during and after the co-seismic period and not earlier than that. From the investigation, it is observed that PS having higher deformation either moving away from the satellite (-40 to -60 mm/yr) or towards the satellite (20 to 40 mm/yr) are primarily found in regions that experienced PGA larger than 0.6 g during the earthquake (see Figure 29c). Overall, the larger the ground shaking, the higher the post-seismic deformation.

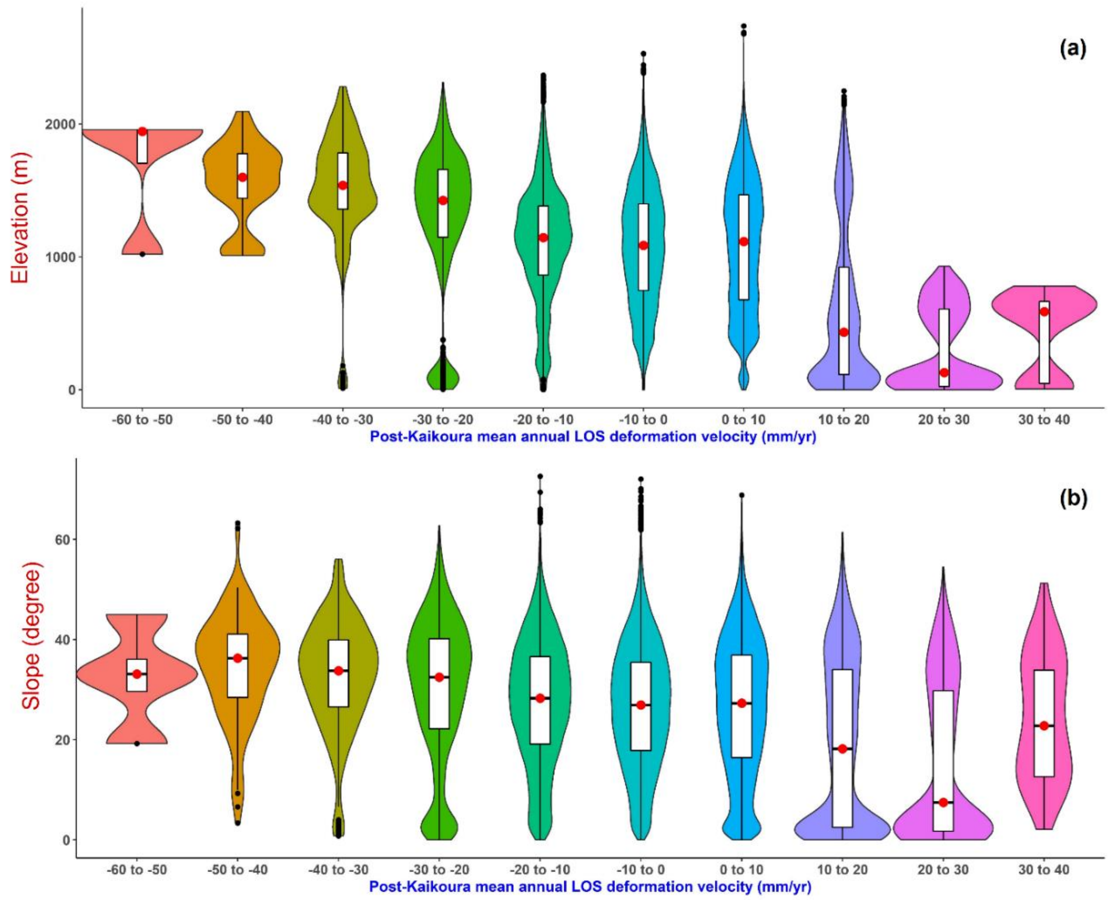

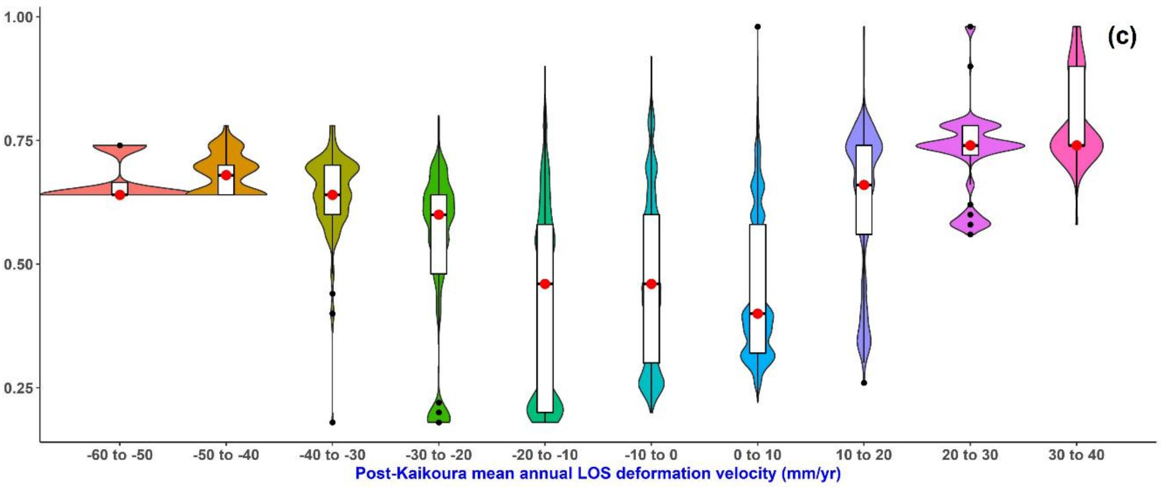

Figure 29. Violin plots showing how (a) elevation, (b) slope steepness, and (c) PGA vary in response to various bins of mean annual LOS deformation velocity retrieved following the Kaikōura earthquake. The red dot in the middle represents the mean values in the respective bins.

5.3. Comparison of deformation rate before and after the Kaikōura earthquake

The deformation rate in the study area before and after the earthquake is quantitatively compared to understand the change in deformation velocity in the entirety (Figure 30). In general, the mean annual LOS deformation velocity shows an approximately 130% absolute increase in the post-Kaikōura phase compared to its pre-seismic counterpart. The PS having velocity between -10 and +10 mm/yr decreased from 248,300 in the count during the pre-Kaikōura phase to 112,287 in the post-Kaikōura period, nearly 55% reduction in the number of PS pixels (See Figure 30). Similarly, 705 PS exhibiting a deformation velocity of -10 to -20 mm/yr before the earthquake increased to 11,924 PS after the event (See Figure 30). There is a 38% increase in the PS pixels that displayed a deformation rate of 10 to 20 mm/yr during the post-Kaikōura phase.

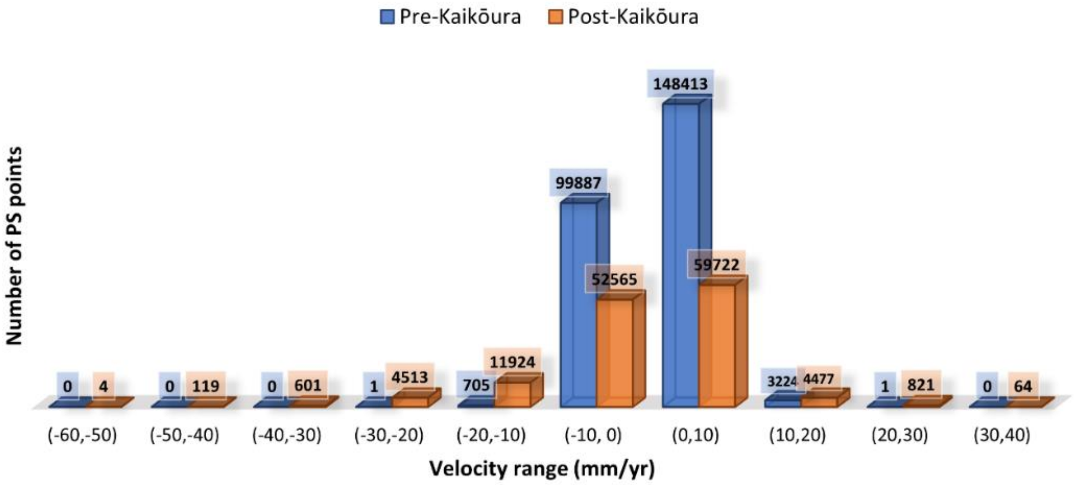

Figure 30. Comparison of PS point counts during pre- and post-Kaikōura by generating mean LOS deformation velocity bins.

5.4. Downslope velocity before the earthquake

After extracting the deformation of the study area in the LOS direction, it is projected to downslope velocity. Since there is no availability of descending images in the same period of analysis, we used the formulation from Aslan et al. (2020) for projecting deformation in the LOS direction to the downslope direction. During the pre-Kaikōura phase, the downslope velocity ranges between a minimum of -63.88 mm/yr and a maximum of 67.58 mm/yr (Figure 31).

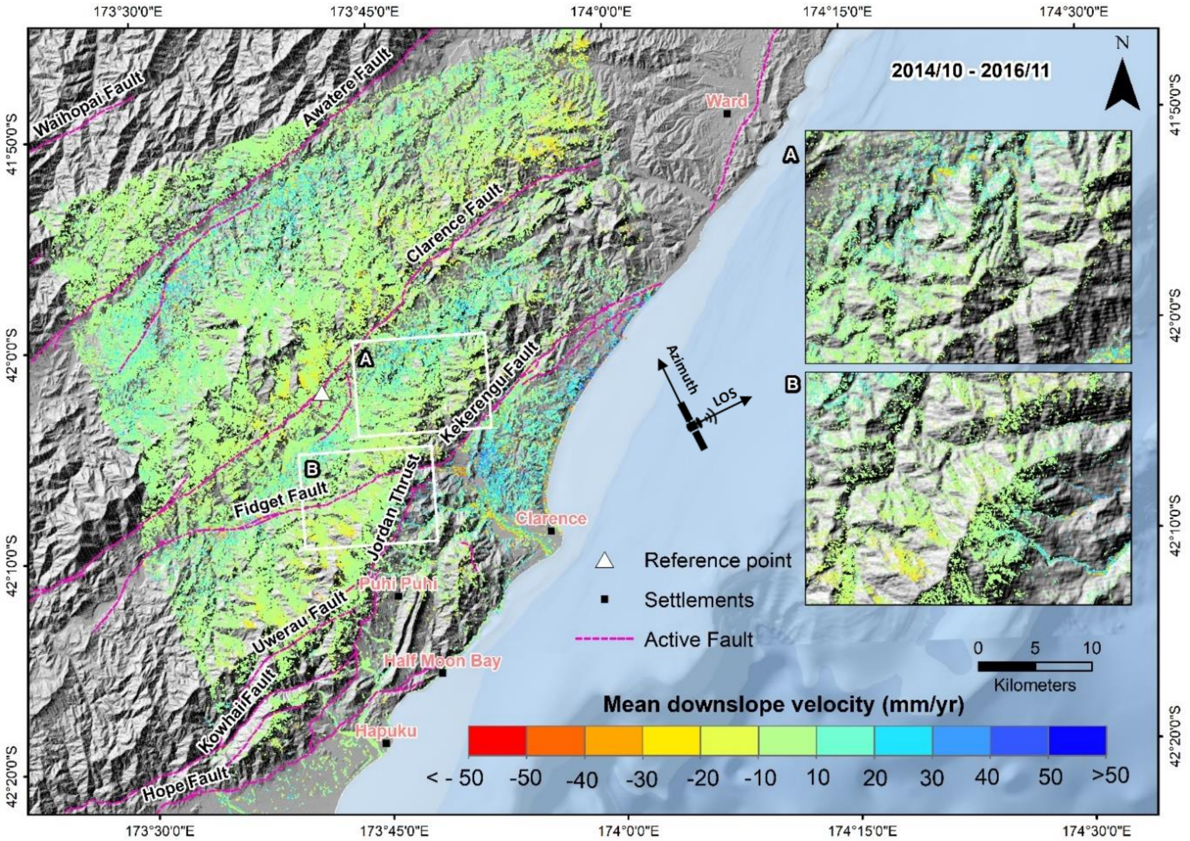

Figure 31. Mean annual Vslope velocity (mm/yr) during the pre-Kaikōura period.

The mean annual downslope velocity is around 1.31 mm/yr, and the standard deviation is about 11.14 mm/yr (Figure 32).

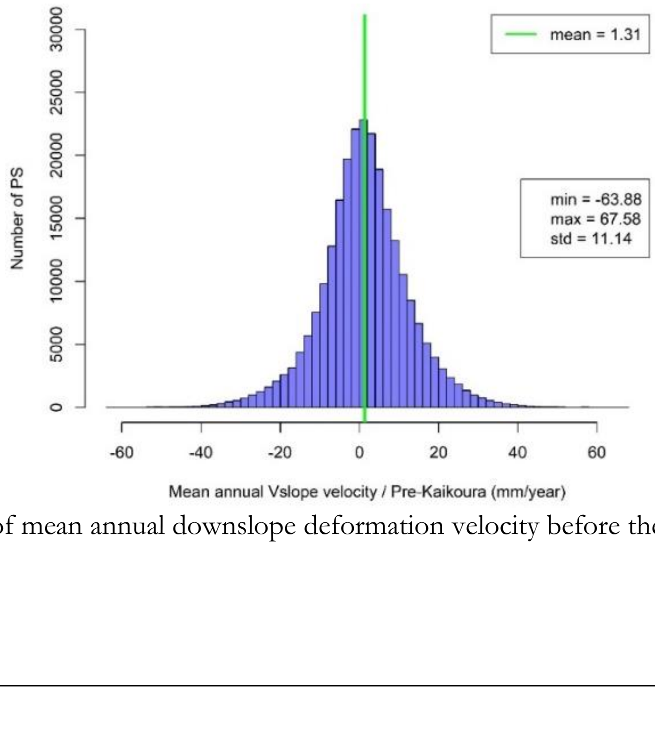

Figure 32. Histogram of mean annual downslope deformation velocity before the Kaikōura earthquake.

5.5. Downslope velocity after the earthquake

During the post-Kaikōura phase, the mean annual downslope deformation velocity is observed to range between -170.23 mm/yr and 159.01 mm/yr (Figure 33). The mean and standard deviation of downslope velocity after the Kaikōura earthquake between 16 November 2016 and 24 December 2018 is about -3.57 mm/yr and 22.48 mm/yr (Figure 34).

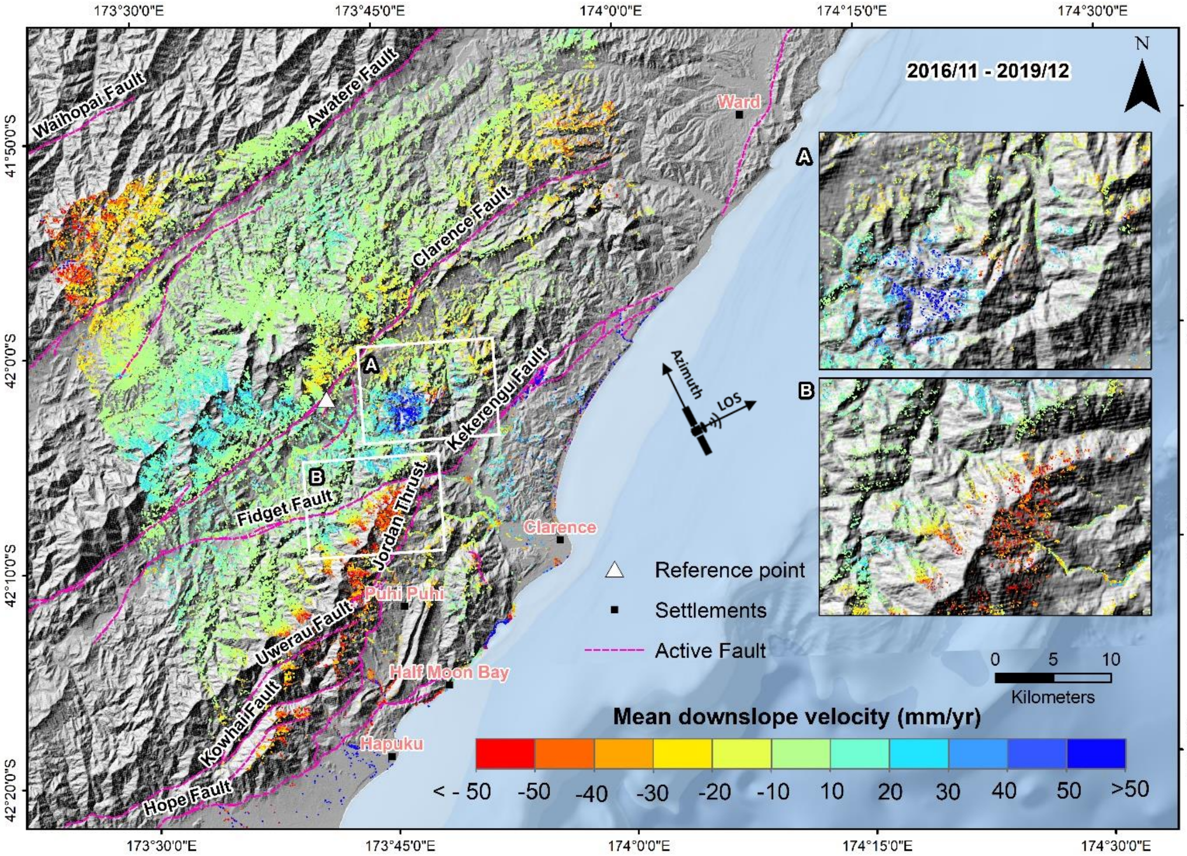

Figure 33. Mean annual downslope velocity during the post-Kaikōura phase.

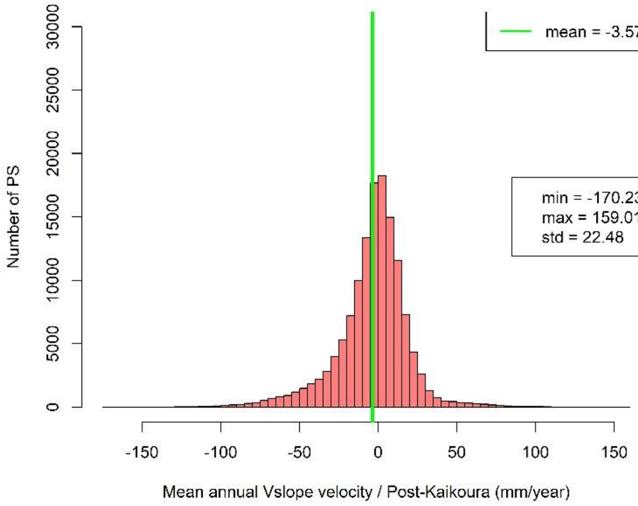

Figure 34. Histogram of mean annual downslope velocity after Kaikōura earthquake.

Notably, in both phases, downslope velocity is higher than that of the LOS velocity, which is in line with all other studies in the literature that used similar formulations other than ascending and descending LOS deformation for the decomposition of deformation into different directions. It also implies that actual deformation is in the downslope direction. In this study, the mean annual LOS deformation velocity is further used for identifying the pixels that have abnormal deformation over time.

5.6. Active PS pixels detection

The detection of actively deforming PS is carried out by setting a critical stability threshold of 10 mm/yr to the LOS deformation. The same critical stability threshold is applied for mean annual pre- and post-Kaikōura LOS deformation velocity (Figures 35a and b). Despite low PS pixels during the post-Kaikōura phase, it is quite observable that the number of PS having a mean annual deformation velocity equal or larger than the defined critical stability threshold is higher in the post-Kaikōura phase than its counterpart (see Figures 35a and b). This is mainly due to the increase in the deformation velocity of the study area after the Kaikōura earthquake.

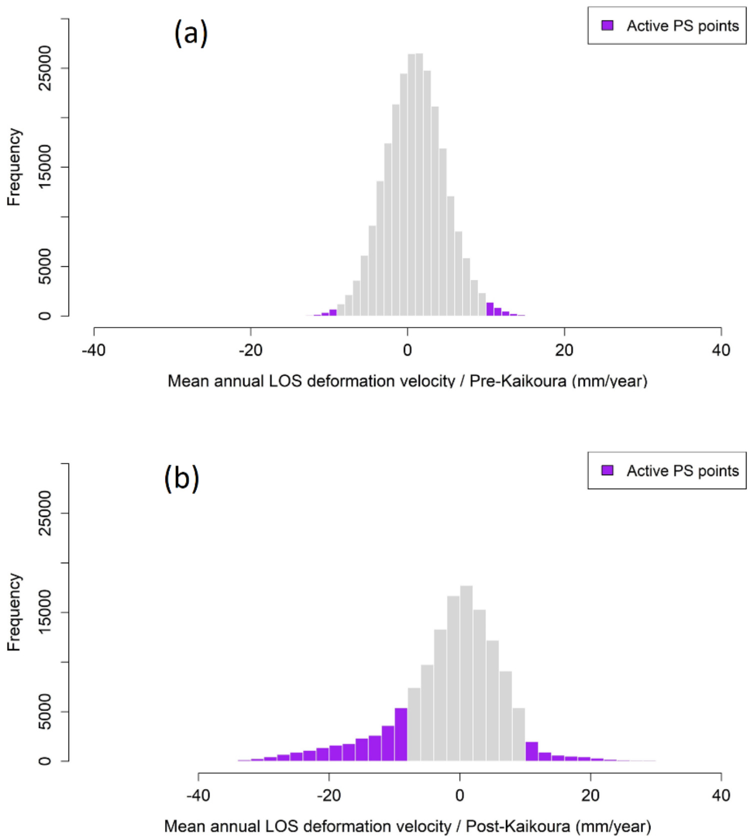

Figure 35. Histogram highlighting the active PS pixels as blue bars from the stable PS pixels displayed as grey bars.

Out of 252,231 PS that were detected in the pre-Kaikōura period, nearly 2,599 PS pixels are classified as active, which is 1.03 % of the entire PS. About 19,446 PS pixels are identified as active in the post-Kaikōura period, which amounts to 14.42 % of total PS found.

After classifying and detecting the active PS, they are further classified into two types of slow-moving PS, namely, extremely slow-moving and very slow-moving PS. In the pre-Kaikōura phase, about 98.73% (2566) of active PS comes under extremely slow-moving while the rest (33) is very slow-moving PS (Figure 36). During the post-Kaikōura phase, 10,641 and 8,805 PS out of 19,446 is identified as extremely slow-moving and very slow-moving PS, respectively (see Figure 36). A large number of very slow-moving PS denoted by red colour (Figure 37) are observed in hillslopes north of the Jordan thrust fault and south of the Uwerau fault. It is also noted in the coastal region of the study area, especially near Hapuku (see Figure 37). The hillslopes located in the northwest region above the Awatere fault of the study area also consist of a higher density of very slow-moving PS pixels (see Figure 37).

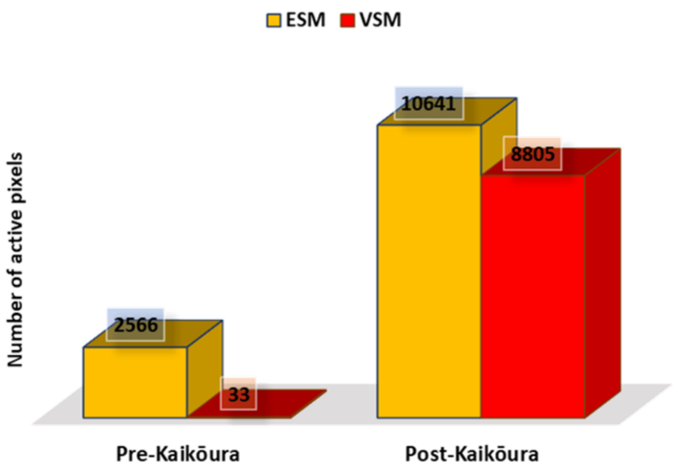

Figure 36. Extremely slow-moving (ESM) and very slow-moving (VSM) PS pixels during pre- and post-Kaikōura phases.

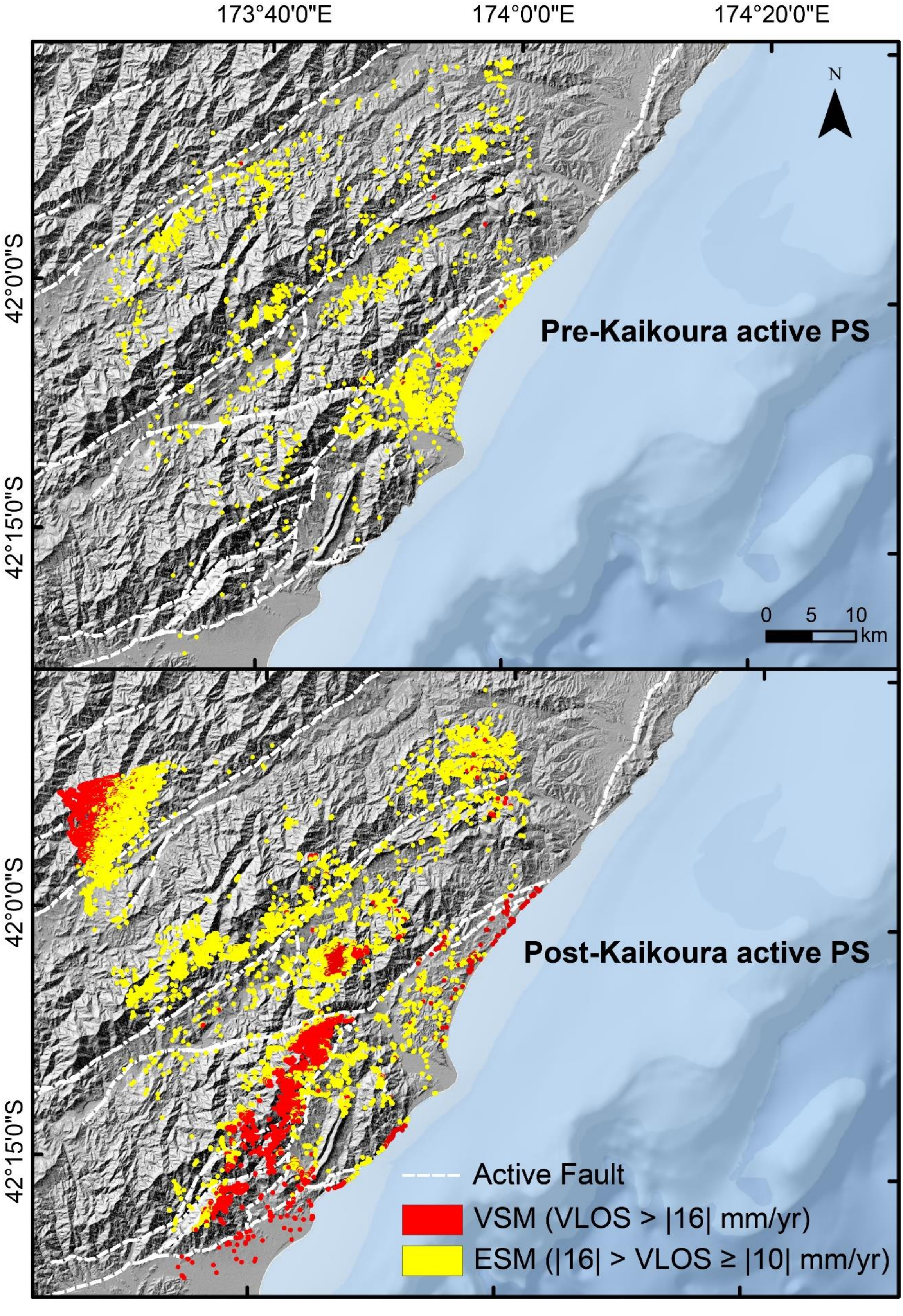

Figure 37. Spatial distribution of extremely slow-moving and very slow-moving PS pixels during pre- and post-Kaikōura periods.

5.7. Spatial distribution of active PS in different landforms

Before analysing the distribution of active PS across diverse landforms, aerial coverage of landform elements in the study area is presented in Figure 38 and Figure 39, respectively. All the ten typical landforms are present in the area of interest, with slope and spur covering more than half of the entire region (see Figure 39). On the other hand, flat and footslope are the landforms with the least aerial coverage. In contrast, hollow (18.79%), valley (11.25%), and ridge (10.29%) cover 40.85% of the study area in total (see Figure 39). The spatial resolution of SRTM-1 arcsec DEM could be a reason for the least area being classified as footslopes and flat landform (Ngunjiri et al., 2020).

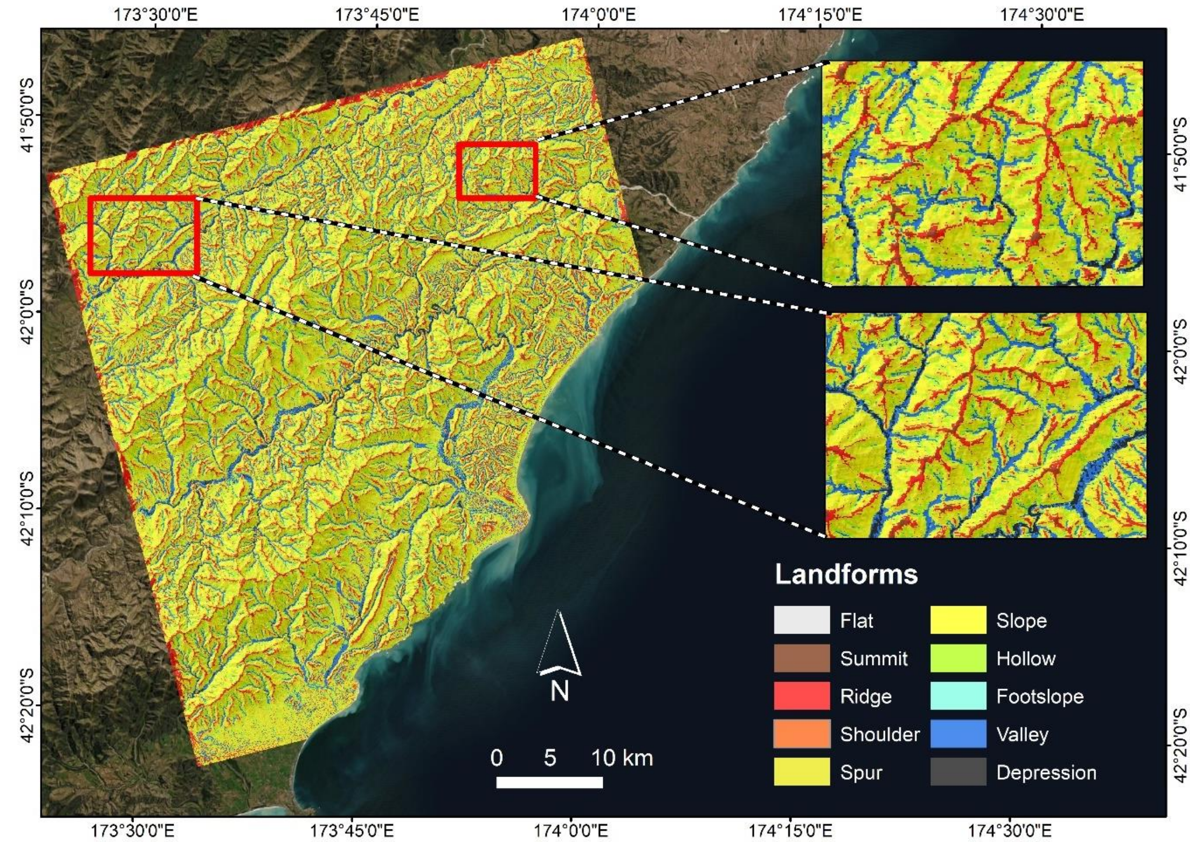

Figure 38. Spatial distribution of ten common landforms identified in the study area.

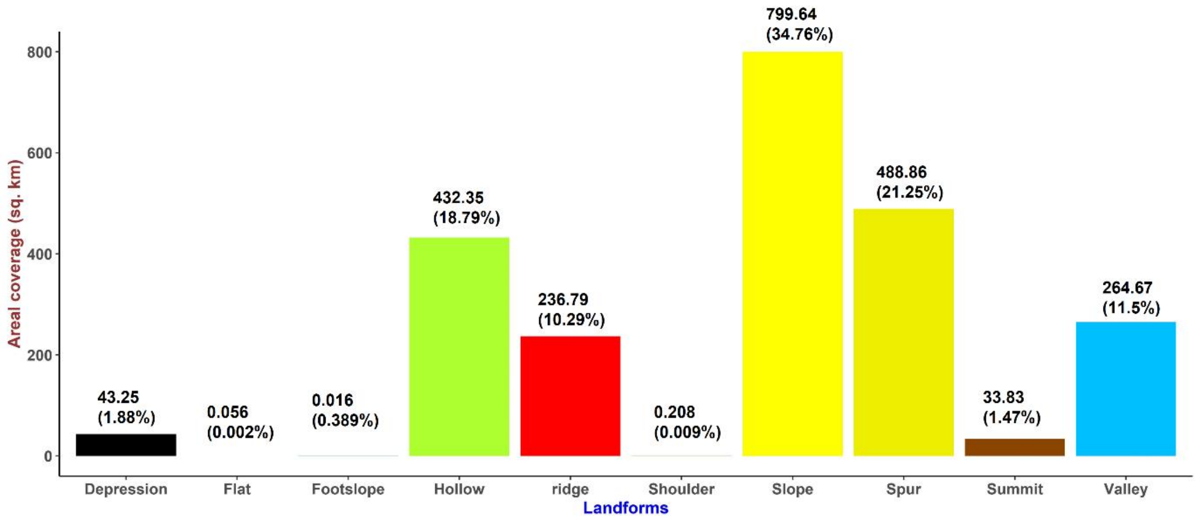

Figure 39. Aerial coverage of different landforms in the study area with their percentage.

Actively deforming PS pixels (extremely slow-moving and very slow-moving) are largely observed in landforms such as slope, spur, ridge, hollow, valley, and summit during the pre- and post-Kaikōura phase (Figures 40a and b). It is also visible that there is a significant increase in the number of PS moving very slowly in the post-Kaikōura compared to its counterpart (see Figure 40).

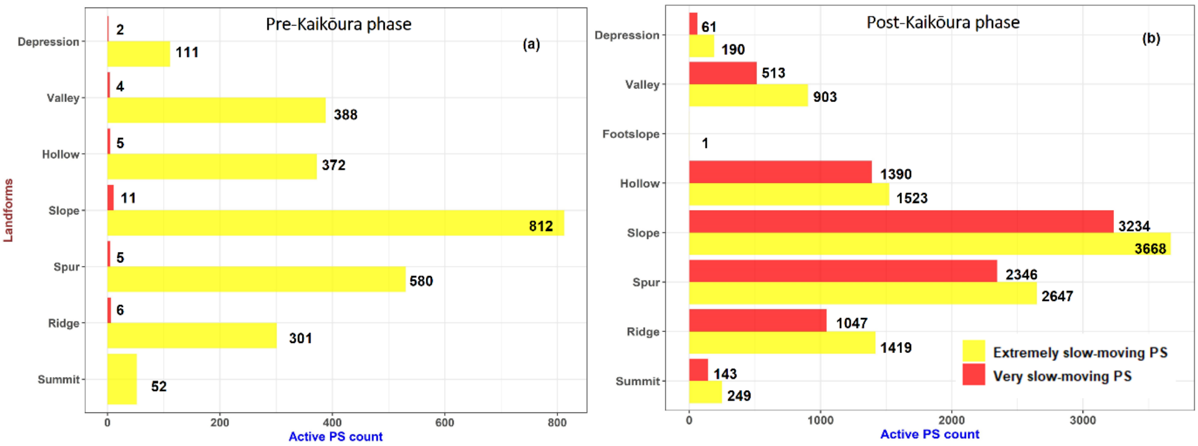

Figure 40. Distribution of extremely slow-moving and very slow-moving PS pixels over different geomorphons present in the study area during (a) pre-Kaikōura and (b) post-Kaikōura period.

5.8. Lithological control of actively deforming PS

Lithology of the study area is relatively identical and is largely covered by greywacke. Therefore, most of the actively deforming PS in both pre- and post-Kaikōura phases is observed in greywacke. Weakly consolidated conglomerate and mudstone consist of more active PS, especially extremely slow-moving, after greywacke in the pre-Kaikōura period. But in the case of the post-seismic phase, limestone had the most very slow-moving PS pixels, while the alluvium flood plain consisted of the most extremely slow-moving PS after the greywacke.

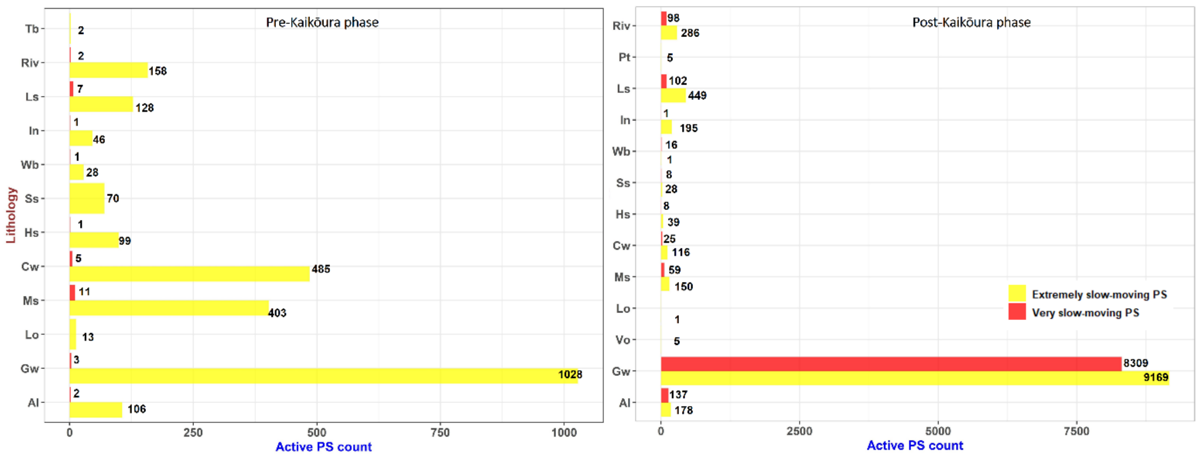

Figure 41. Distribution of extremely slow-moving and very slow-moving PS across different lithological units before (a) and after (b) the earthquake. Al – undifferentiated flood plain alluvium, Gw – greywacke, Vo - lavas and welded ignimbrites, Lo – loess, Ms – mudstone, Cw - weakly consolidated conglomerate, Hs – sandstone (strong), Ss- sandstone (weak), Wb – windblown, In – ancient volcanoes, Ls – limestone, Pt – peat, Tb – pyroclastics.

5.9. Slope units

In total, the region of interest of this study consists of 5104 slope units with an average area of about 450,804 m² and a standard deviation of 390935 m² (Figure 42). The maximum size of the slope unit was around 3,806,250 m².

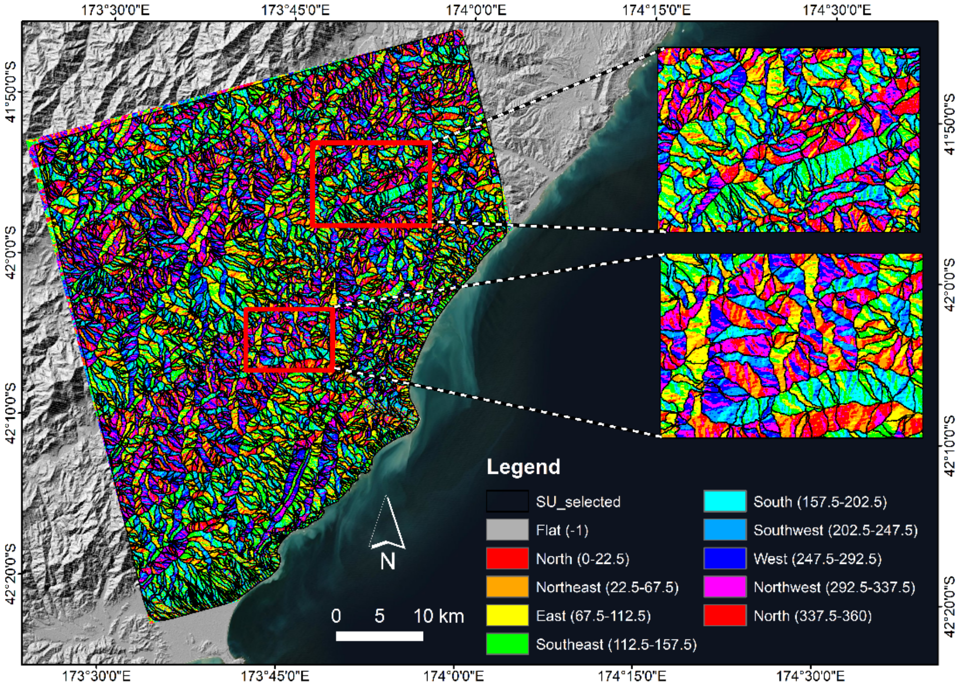

Figure 42. Delineated slope units of the study area overlaid on aspect and hillshade.

5.10. Identification of actively deforming hillslopes

Actively deforming PS are spatially joined with delineated slope units for identifying actively deforming hillslopes in the study area. Slope units with equal or more than 20 actively deforming PS are classified as actively deforming hillslopes. Such actively deforming hillslopes are further classified into extremely slow-moving and very slow-moving hillslopes based on the average LOS velocity of the hillslopes. By doing so, it is identified that nine actively deforming hillslopes were present in the study area before the Kaikōura earthquake between October 2014 and November 2016 (Figure 43), which comes under the category of extremely slow-moving hillslopes. After the Kaikōura earthquake, between November 2016 and December 2018, nearly 243 hillslopes are actively deforming (Figure 44). Out of 243 actively deforming hillslopes, 141 are found to be extremely slow-moving, and 102 are observed as very slow-moving.

The hillslopes which are detected to be active before the 2016 Kaikōura earthquake have an area of 1.32 km² on average (Figure 45a), while their average slope is 20.74° (Figure 45b). The actively deforming hillslopes that are identified during the post-seismic phase have an average area of about 0.83 km² (Figure 46 a), with hillslopes having minimum and maximum areas of about 0.12 km² and 3.8 km², respectively. Their average slope is around 29.3°, while the minimum and maximum slope of hillslopes range between 8.77 and 39.29° (Figure 46 b).

The density of active PS within actively deforming hillslopes during the pre-Kaikōura phase ranges between 13.14 km² and 57.5 km² (Figure 47a), while PS density in active hillslopes during the post-Kaikōura phase varies between 5.52 km² and 450.9 km² (Figure 47b). Higher the PS density, the reliability of the active deformation finding is more considerable (Cigna et al., 2013).

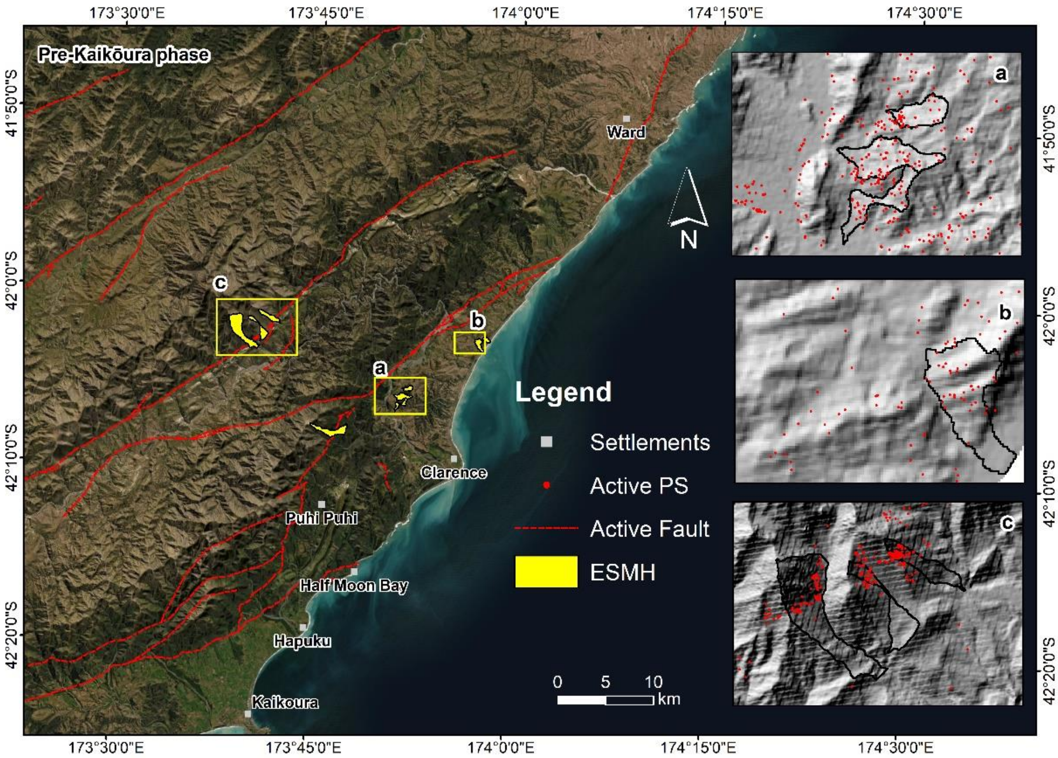

Figure 43. Actively deforming hillslopes identified during the pre-Kaikōura phase superimposed on World Imagery basemap. The active PS pixels are overlaid upon hillslopes in the insert maps (a, b, c and d) (ESMH: Extremely slow-moving hillslope).

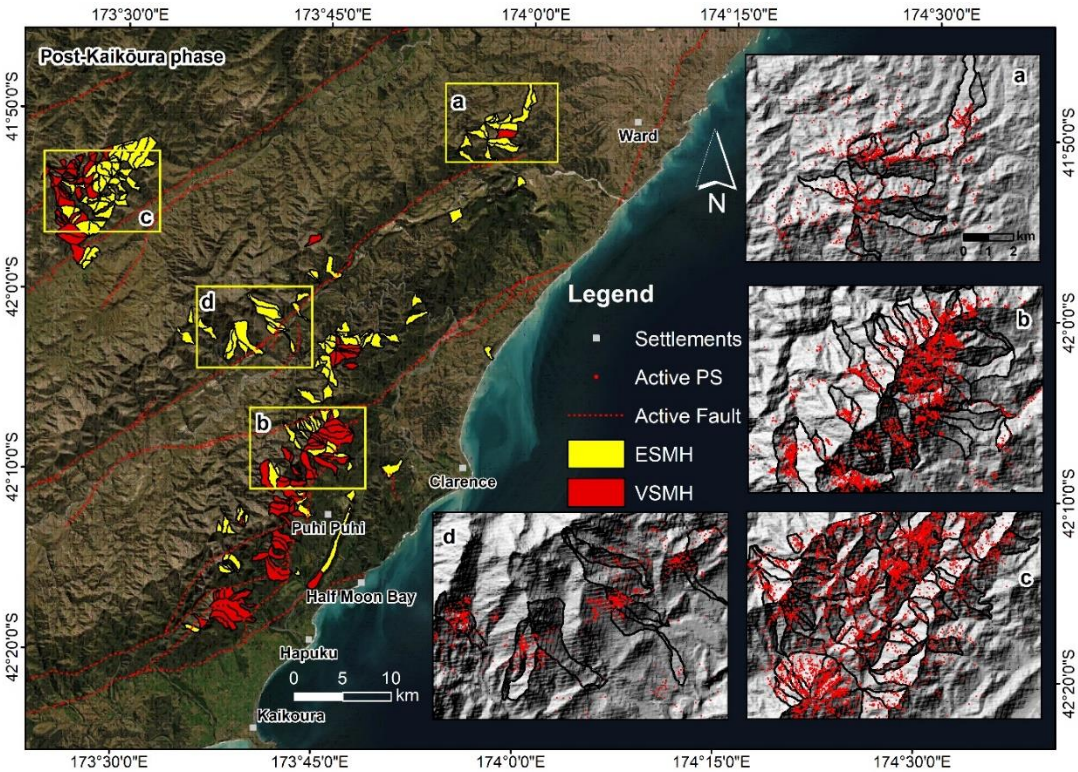

Figure 44. Actively deforming hillslopes during the post-Kaikōura phase till December 2018 overlaid upon World Imagery basemap (ESMH: Extremely slow-moving hillslope, VSMH: Very slow-moving hillslope).

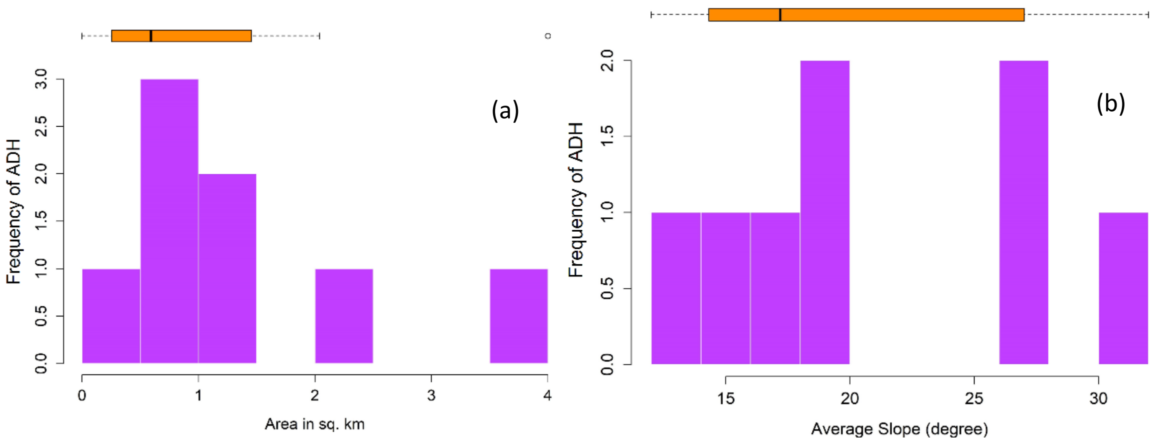

Figure 45. Distribution of surface area (a) and average slope (b) in degrees of actively deforming hillslopes (ADH) before the Kaikōura earthquake.

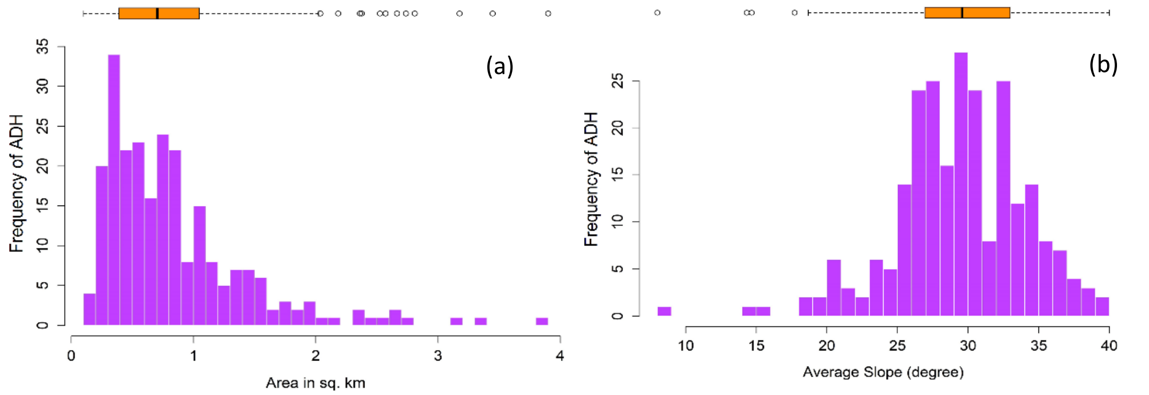

Figure 46. Distribution of surface area (a) and mean slope in degrees of actively deforming hillslopes (ADH) after the Kaikōura earthquake.

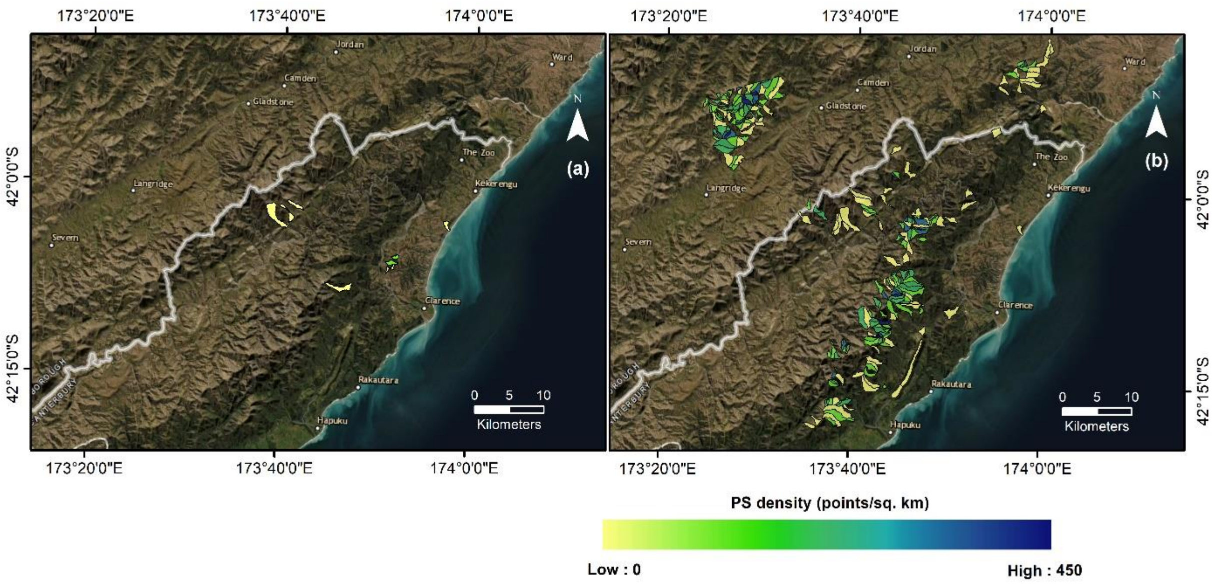

Figure 47. PS density per hillslope during (a) pre- Kaikōura and (b) post- Kaikōura phase is created with the detected active PS.

5.11. Post-seismic hillslope deformation matrix

Four types of sub-meter hillslope deformation activity have been observed in the study area (Figure 48), as described in Section 4.6, Table 5. According to the post-seismic hillslope deformation matrix presented in Table 5, 239 new actively deforming hillslopes were identified during the post-Kaikōura period, which was stable before the 2016 Kaikōura earthquake (Type I: SA). There are four hillslopes that are observed to be active during both pre- and post-Kaikōura phases (Type II: AA). Nearly five of actively deforming hillslopes are noticed to have become stable after the earthquake, which is classified as the third type of hillslope deformation activity (Type III: AS). Finally, 4856 hillslopes are observed to have stable kinematics before and after the Kaikōura earthquake (Type IV: SS).

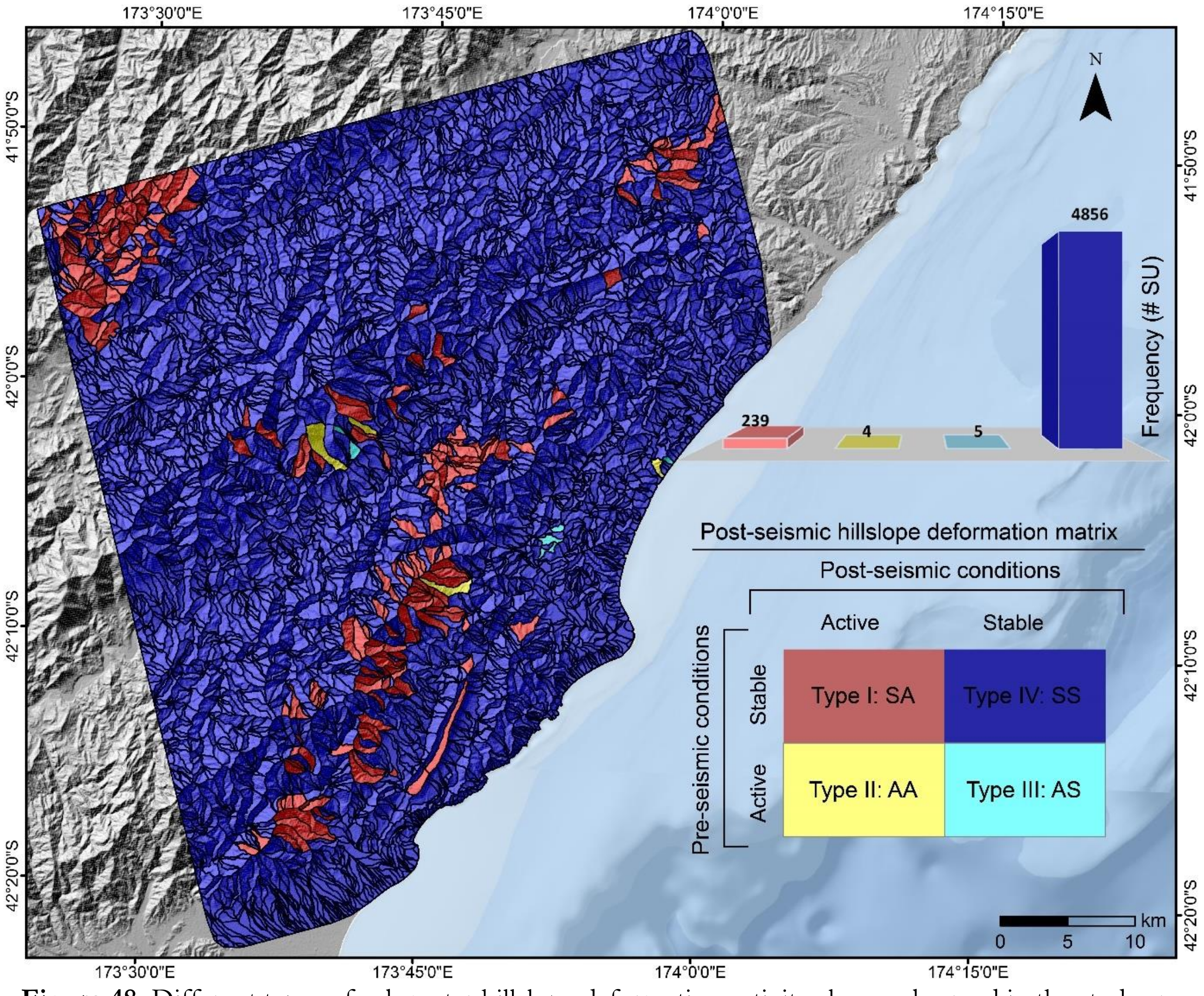

Figure 48. Different types of sub-meter hillslope deformation activity classes observed in the study area.

Also, I checked the spatial distribution of hillslopes associated with both presence of co-seismic landslides and active hillslope deformations (Figure 49). Results show that nearly 127 hillslopes that are found to be actively deforming in the post-Kaikōura phase is affected by the co-seismic landslides that occurred during the mainshock of 2016 Kaikōura earthquake (see Figure 49). About 116 hillslopes that are not affected by the co-seismic landslides are discovered to be having active sub-meter deformations (see Figure 49).

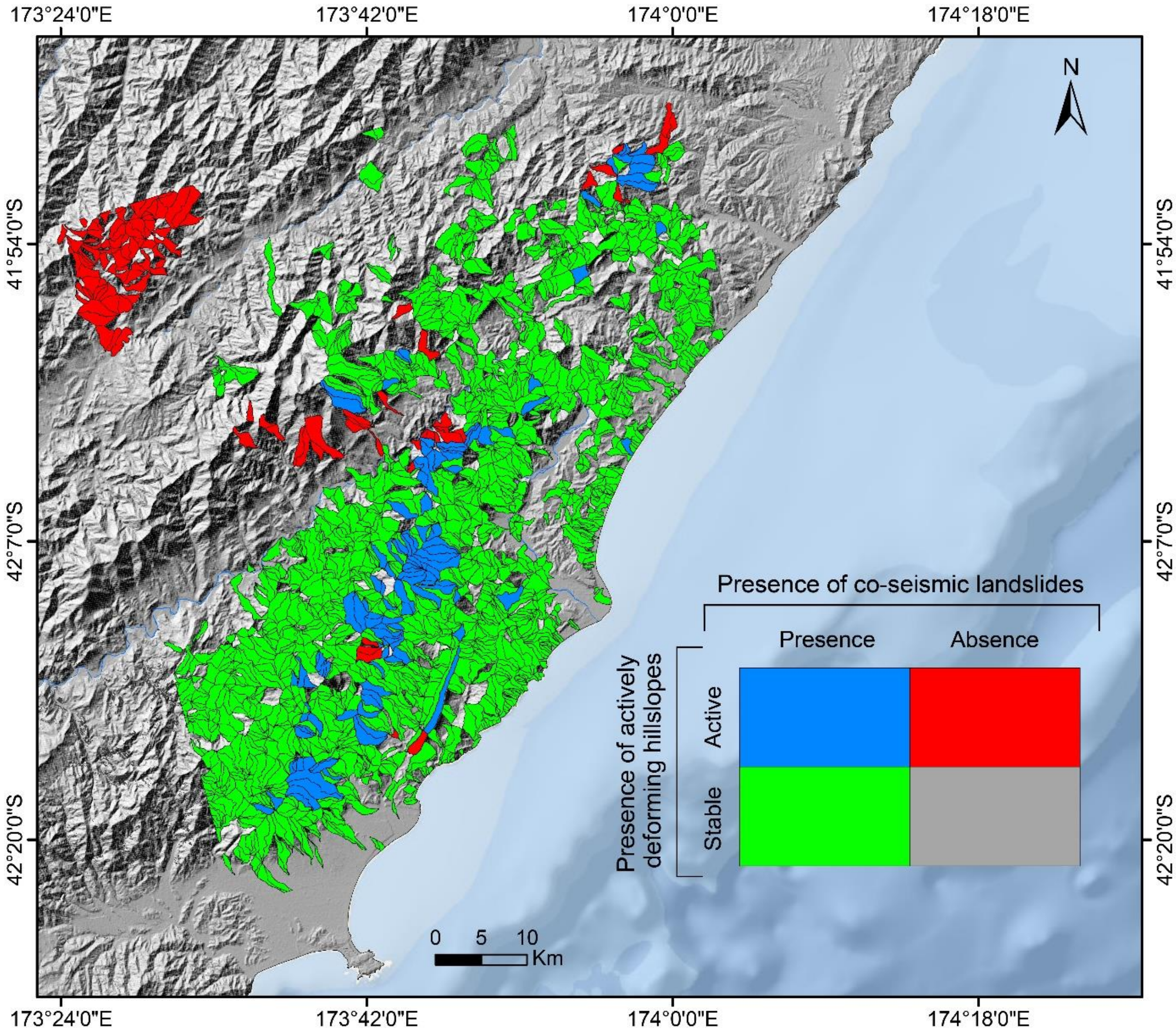

Figure 49. Different types of actively deforming hillslopes associated with presence of co-seismic landslides.

5.12. Evolution of hillslopes affected by the 2016 Kaikōura earthquake

It is evident from the previous sections that hillslopes present in the study area were significantly impacted by the 2016 Kaikōura earthquake, which had a magnitude of 7.8. Now, I will examine the first three types of post-seismic hillslope deformation classes in detail below with the deformation time series and visual examination of daily precipitation from CHIRPS data using one representative hillslope in each class.

5.13. Type-I (SA)

Apart from triggering a large number of co-seismic landslides, the 2016 Kaikōura earthquake is found to have initiated active deformation in 239 hillslopes across the study area, which were seen to be inactive before the large seismic event. Out of 239 hillslopes, 129 belong to the extremely slow-moving hillslope category, while the rest are very slow-moving hillslopes. This way doing a pre-seismic deformation analysis even for a shorter period helps us to know if a hillslope is already active before the earthquake.

Since there are more than 200 hillslopes in this evolution type, here, only a few six of those hillslopes are exemplified with their deformation time series and daily precipitation.

The first representative hillslope depicts the evolutionary history of how a stable hillslope is metamorphosed into a very slow-moving landslide with an absolute mean annual LOS deformation velocity of greater than 16 mm/yr owing to the impact of a high magnitude earthquake (Figure 50). It is located 89 km northeast from the epicenter of the Kaikōura earthquake and just above the Jordan thrust fault, which experienced a significant slip during the 2016 event (Diederichs et al., 2019). The slope gradient of the hillslope ranges between 3.03° and 60°, with an average elevation of 1,053 m. The hillslope has an area of about 1.4 km^2, and the scarp region, which is identified to be active with the help of PSI in the post-Kaikōura phase, is around ~0.45 km^2. There is a lack of PS coverage over the densely vegetated body and toe of the hillslope owing to the temporal decorrelation. Yet, a small region devoid of vegetation in the body of the hillslope is observed to contain a few PS, which are also actively deforming in the post-seismic phase (see Figures 50a and b). However, the PS located in the toe of the hillslope is inactive during the post-seismic period (see Figure 50b). The annual average LOS and downslope deformation velocity of the entire hillslope vary wildly in the periods before and after the 2016 Kaikōura earthquake (Figures 50c and d). The mean LOS deformation velocity of the hillslope is 2.5 mm/yr during the pre-seismic phase and -31.51 mm/yr after the earthquake (see Figures 50c and d).

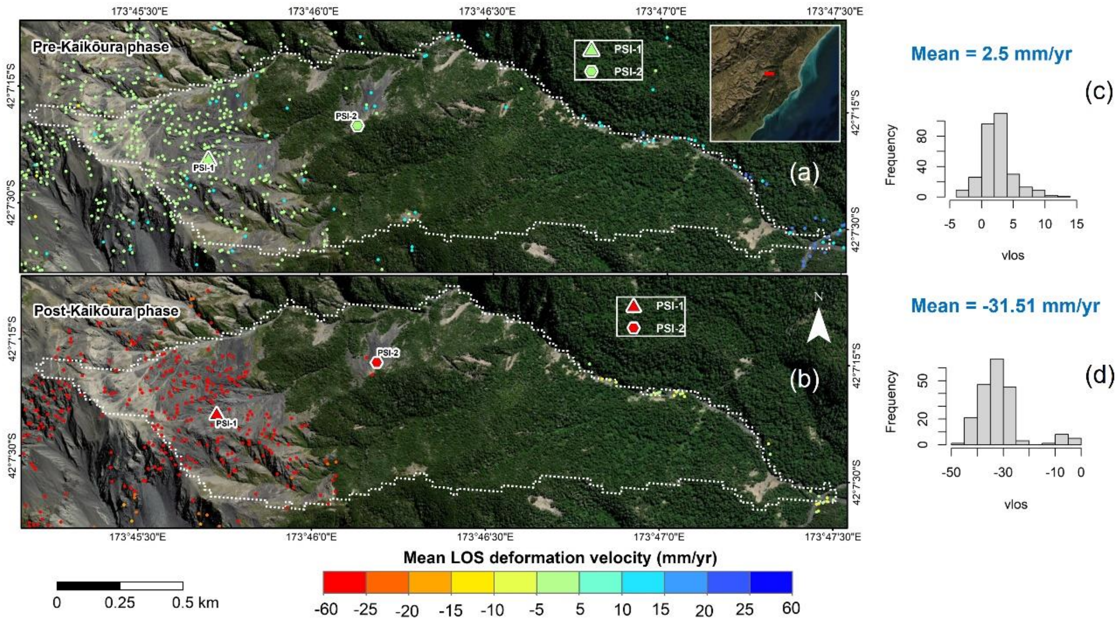

Figure 50. PS pixels identified during (a) pre-Kaikōura and (b) post-Kaikōura phase exhibiting mean LOS deformation velocity (c-d).

Similarly, the hillslope experienced 6.5 mm/yr and -78.76 mm/yr of mean downslope deformation velocity before and after the seismic incident, respectively. The maximum and minimum average LOS deformation velocity experienced by the hillslope during the pre-seismic phase is 12.21 mm/yr and -3.6 mm/yr. In contrast, it is observed to be -2.64 mm/yr and -45.18 mm/yr during the post-seismic phase, respectively. The pre-Kaikōura deformation results show that the hillslope is stable between 2014 and 2016, right before the earthquake.

To understand how the deformation of the hillslope varies in different time steps before and after the 2016 Kaikōura earthquake, the deformation time series of the entire hillslope along with two selected PS points, one on the scarp and another located on the body of the hillslope is visualised along with the daily precipitation from CHIRPS data, which has a spatial resolution of about 5 km (Figure 51a, b, c, and d). It can be noted from the linear trend of deformation that the hillslope was inactive during the pre-Kaikōura phase (see Figure 51a) and began to show a sudden increase in the deformation rate after the earthquake (see Figure 51b). In addition, the deformation time series exhibit seasonal deformation during the post-Kaikōura phase (Figure 51b, d, and f). Nearly a cumulative LOS displacement of about 100 mm is witnessed in the entire hillslope between November 2016 and December 2018 (Figure 51b). There is a gradual decay in the deformation velocity during the post-Kaikōura period, which can be observed from the average deformation time series of the hillslope (see Figure 51b).

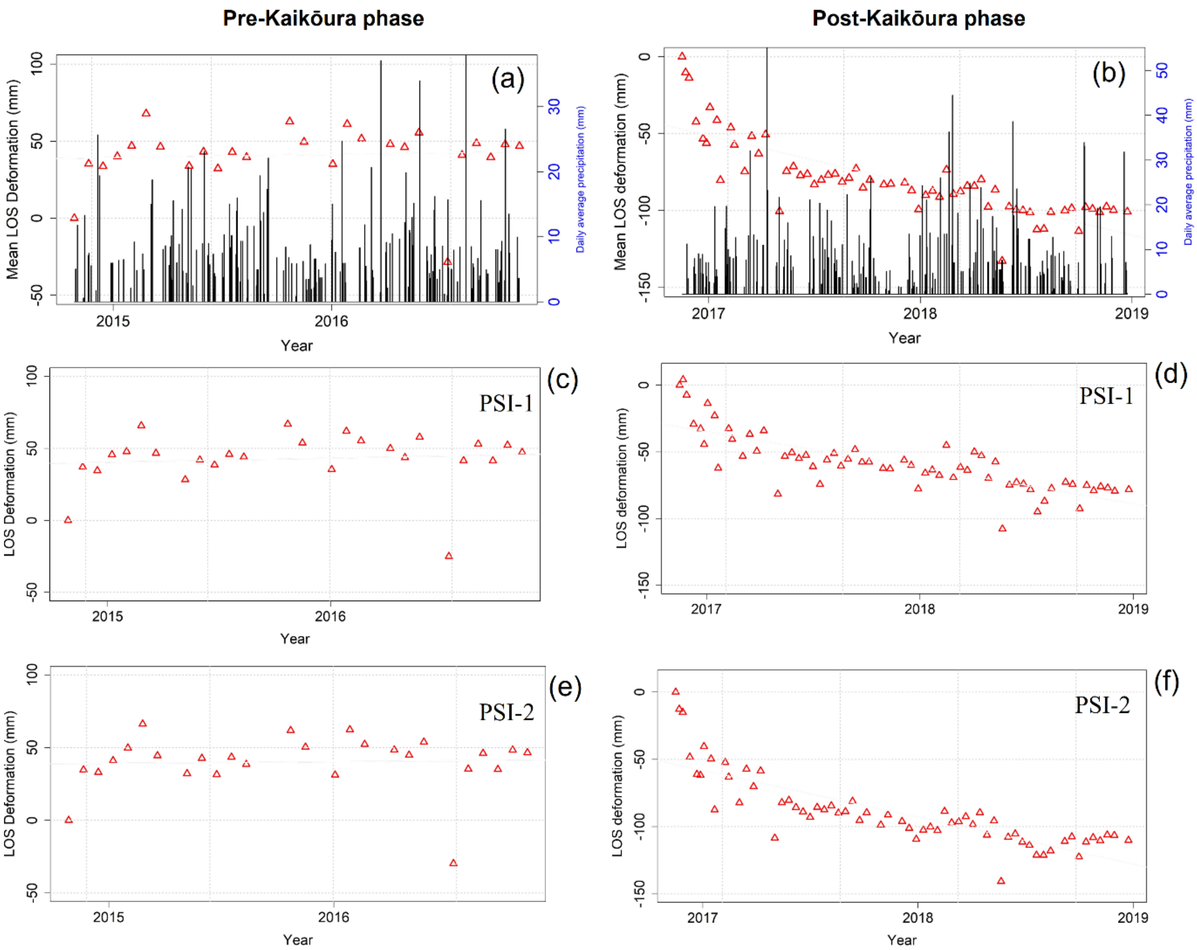

Figure 51. Example of Type-I (SA) hillslope represented by mean LOS deformation time series (a-b) and LOS deformation of two PS points located inside the hillslope (c-f) during pre-Kaikōura and post-Kaikōura phases.

5.14. Type-II (AA)

The second important evolution type noticed in this study is the active deformation of hillslopes before and after the earthquake. Four hillslopes were found to be having such evolution after the 2016 Kaikōura earthquake, among which one hillslope is presented with active PS and their respective deformation time series for each phase before and after the earthquake (Figure 52). Among the four hillslopes, two were affected by co-seismic landslides during the mainshock of the earthquake in 2016 and still continue to deform actively in the post-seismic phase. The representative hillslope which is discussed for this deformation evolution type is not affected by the co-seismic landslide. The hillslope is located 94.5 km away from the earthquake epicenter and has an area of about 1.01 km^2. This hillslope is found to be extremely slow-moving before the 2016 earthquake (see Figures 52c and d), which continues to be the same after the event but with a change in the deformation velocity. The mean LOS deformation velocity of hillslope slightly increased from -11.64 mm/yr during the pre-Kaikōura phase to -12.12 mm/yr in the post-Kaikōura phase (see Figures 52c and d)). The region below the source area is identified to be actively deforming before and after the seismic event (see Figures 52a and b). The deformation time series also confirms the active movement of hillslope during both pre- and post-Kaikōura phase (Figure 52e and f).

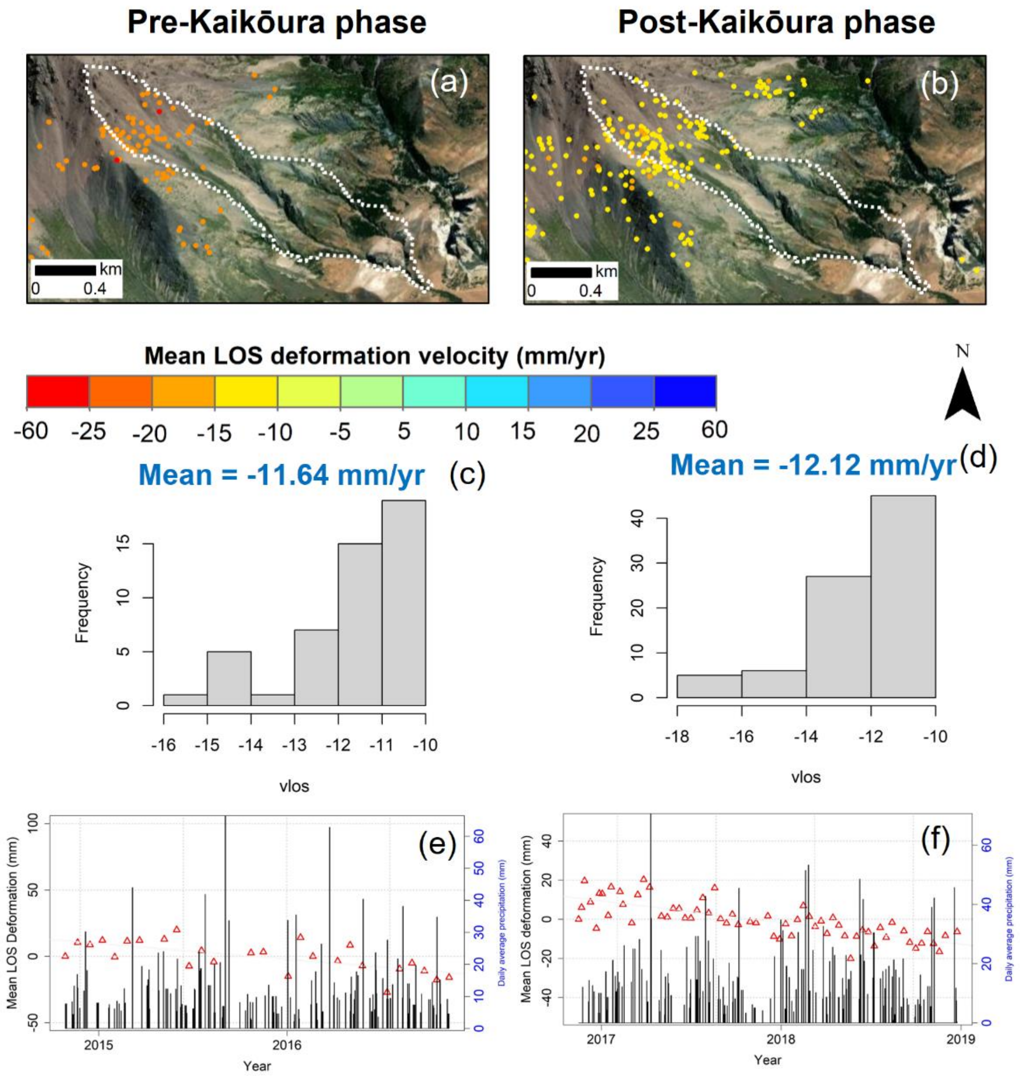

Figure 52. Example of hillslope evolution Type-II (AA) represented with active PS of a representative hillslope (a and b) along with the histogram of its mean LOS velocity (c and d) and its respective deformation time series (e and f) during pre- and post-Kaikōura phase.

5.15. Type-III (AS)

The third evolution type that is observed in the study area is the stabilisation of hillslopes in the post-Kaikōura phase that are found to be extremely slow-moving in the pre-Kaikōura phase. There are five hillslopes in this category, among which only one is affected by co-seismic landslides during the mainshock while the rest of the hillslopes are not. In this type, a representative hillslope is presented, for example, which is not affected by the co-seismic landsliding.

The representative hillslope is about 98.01 km northeast of the earthquake's epicenter and has an area of about 0.81 km^2 (Figure 53). The hillslope has a positive mean LOS deformation velocity before and after the earthquake (see Figure 53a-d). However, the hillslope is observed to have extremely slow movement before the earthquake, with mean LOS deformation of about 11.66 mm/yr (see Figure 53c). In the post-seismic phase, there is a decrease in the deformation velocity to 6.43 mm/yr, which is below the active deformation threshold (see Figure 53d). The deformation time series can be seen supporting this type of hillslope deformation evolution (see Figure 53e and f).

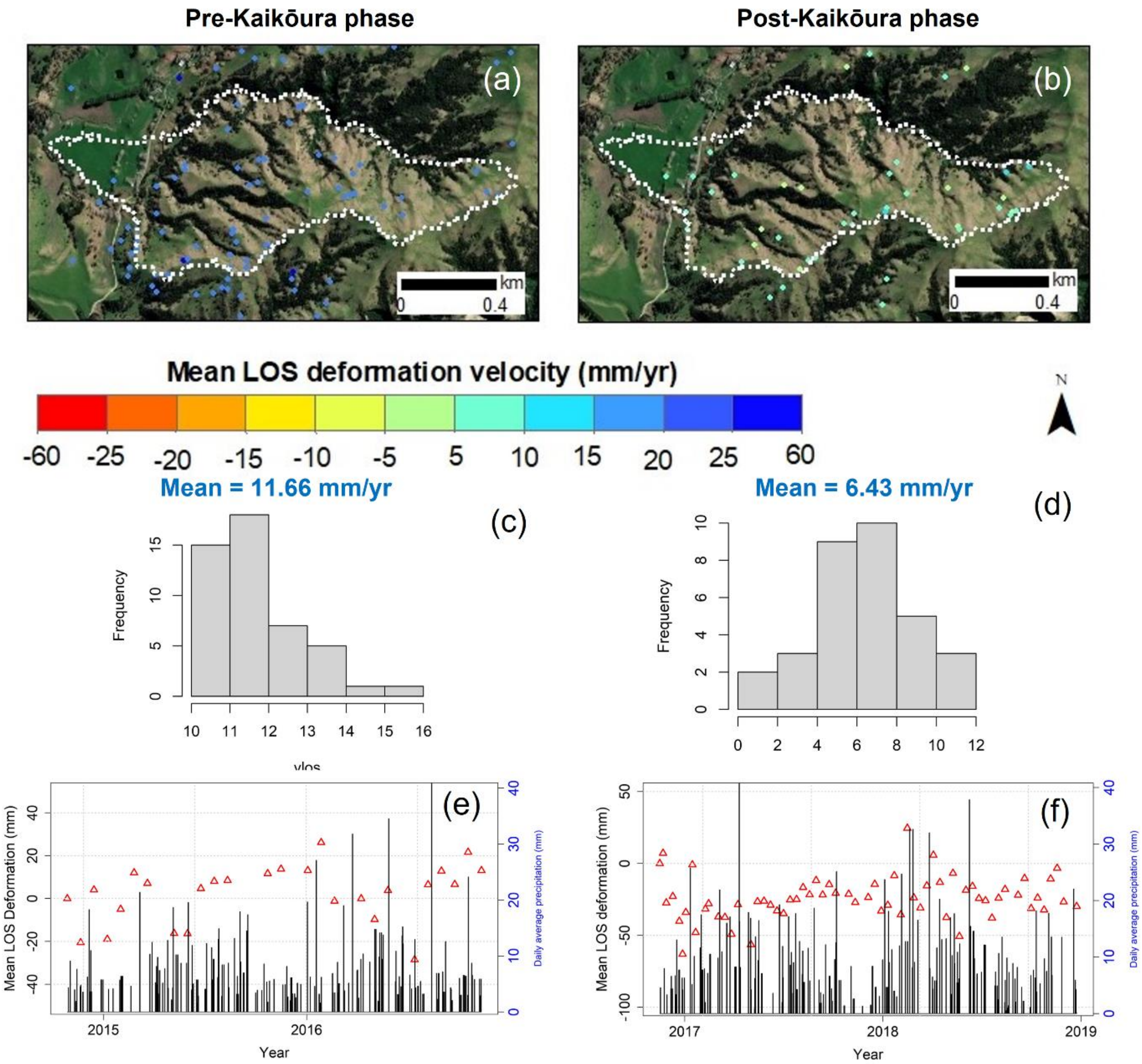

Figure 53. Example of hillslope evolution Type-III (AS) represented with active PS of a representative hillslope (a and b) along with the histogram of its mean LOS velocity (c and d) and its respective deformation time series (e and f) during pre- and post-Kaikōura phase.

6. DISCUSSION

Understanding the evolution of hillslopes affected by intense seismic shaking helps to better evaluate post-seismic hazards and risks, as well as plan management and mitigation measures. So far, there has been a large body of literature available on studying the impact of earthquake legacy effect on the post-seismic evolution of rapidly collapsing hillslopes (Chen et al., 2020; Fan et al., 2018; Kincey et al., 2021; Shafique, 2020; Tang et al., 2016; Tanyaş et al., 2021a, 2021b; Wang and Mao, 2022), while there are only a few studies (Cai et al., 2022; Cheaib et al., 2022; Lacroix et al., 2022) carried out on examining the same on the evolution of extremely slow and very slow-moving hillslopes in an earthquake-affected region. To the best of our knowledge, such documentation on the impact of the earthquake legacy effect has not been carried out for the hillslopes that become active with a sharp surge in the velocity during the post-seismic period yet. This research focuses on addressing such prevailing knowledge gap in the existing literature by attempting to capture the varying deformation dynamics exhibited by the active hillslopes in the range of millimeters to centimeters before and after the mainshock of the 2016 Kaikōura earthquake in order to understand their evolution triggered by the earthquake. The findings of this study offer the first comprehensive illustration of how a large magnitude earthquake alters the dynamics of the stable hillslopes owing to its impact. The area affected by the 2016 Kaikoura earthquake, which had one of the most intricate rupturing mechanisms ever documented in history (Hamling et al., 2017), is covered by greywackes that are widely observed for deep-seated active hillslopes (Korup, 2008; Jelének and Kopačková-Strnadová, 2021; Massey et al., 2018b, 2020; Singeisen et al., 2022; Tanyaş et al., 2022; Cruden and Varnes, 1996; WP/WLI, 1995).

Although intense ground shaking from large seismic events frequently causes landslides, hillslopes activated by the earthquake with sub-meter displacement are difficult to detect in active mountainous terrains. Employing the MT-InSAR technique can help in finding such hillslopes triggered by the earthquake having sub-meter deformation and understanding their evolution over time after the event. In this context, this research has two main novelties. First, this research developed and showcased a novel systematic approach for identifying active hillslopes which are already existed before and those that were generated after the impact of the 2016 Kaikōura earthquake. The proposed technique could be transferable to other earthquake-affected areas to unveil the evolution of the hillslopes in post-seismic periods. Ultimately, by analysing and comparing the changes in the deformation time series of those detected active hillslopes during immediate pre- and post- Kaikōura phases, this study has found four types of hillslope evolution, among which three are the most significant. The results of this study for the first time, documented an abrupt increase in the number of active deforming hillslopes which are identified immediately during the coseismic. By identifying and monitoring such active hillslopes triggered by the earthquake for a long term can help in making well-informed management decisions to prevent those active slopes from failing catastrophically owing to acceleration from further external triggers, which can save people's life and property (Lacroix et al., 2020). Second, for the first time, SUs are used in this study to aggregate actively deforming PS contained within them to identify active hillslopes rather than using the standard pixel density clustering approach as employed by Bekaert et al. (2020) and Aslan et al. (2020). Below, I will discuss the findings of this research further as well as the methodological preferences I made during the analyses.

6.1. Classification of hillslopes based on surface deformations

In this research, the landslide velocity classification from Cruden and Varnes (1996) is used to define the critical stability threshold and also the velocity limit between extremely slow-moving and very slow-moving PS. Such an approach was also used by Cigna et al. (2013). However, a large number of studies combine these both velocity classes into a single category and term them collectively as the slow-moving hillslopes

(Handwerger et al., 2013; Lacroix et al., 2020). In this research, there is a sudden increase of PS having very slow movement in the post-Kaikōura phase compared to its counterpart (see Figure 37).

Overall, this study found 243 hillslopes actively deforming after the impact of the 2016 Kaikōura earthquake, among which nine hillslopes were already found to be active before the event, however, their deformation velocity was extremely slow (see Figure 43 and 44). Cai et al. (2022) reported such activation of new actively deforming hillslopes affected by 2017 Jiuzhaigou earthquake. The findings suggest that the average slope angle of actively deforming hillslopes identified during the post-Kaikōura phase is gentle (29.3°). However, there are slopes which are seen in more steeper slopes above 35° in the study area. Bekaert et al. (2020) documented that slow-moving hillslopes identified in the region affected by the 2015 Gorkha earthquake have an average slope of 22°. Xu et al. (2021) reported that nearly more than 500 active hillslopes detected in the western coast of the United States have slope angles from 5° till 30°. In addition, most of the co-seismic landslides, excluding Wenchuan landslide inventories, have an average slope angle of 27°, and 80% of all landslides have a slope angle between 10° and 45° (Tanyaş et al., 2017).

Most importantly, this study found four types of hillslope evolution by proposing a generic PSI matrix (See Figure 48). The first type is those hillslopes which were stable before the earthquake that became active after its impact. This research also confirms the same with the help of deformation time series (see Figure 50). Such evolution is mainly attributed to the intense seismic shaking, which reduces the strength of the hillslope (Brain et al., 2017). However, it is not known if these hillslopes were historically active before 2014. Similar evolution of hillslopes was also reported in the very recent research of Cai et al. (2022) and Cheaib et al. (2022). Both studies also verified the same with deformation time series information. The second type of evolution observed is those hillslopes that are active before and after the earthquake. It is also found that there are both acceleration and deacceleration in the mean deformation velocity during the post-Kaikōura phase compared to the pre-Kaikōura phase. Bekaert et al. (2020) reported a similar evolution of active hillslopes before and after the 2015 Gorkha earthquake. However, Cai et al. (2022) found that there was a acceleration in the deformation velocity of active hillslopes after the 2017 Jiuzhaigou earthquake impact. Based on analysing the deformation time series Cheaib et al. (2022) document that active hillslope being accelerated during the immediate phase close to the mainshock which decreases later. This research also found that four hillslopes that were active before the earthquake became stable after its impact. Such evolution can be owing to the intense seismic shaking. Lastly, a large number of hillslopes are found to behave stable before and after the 2016 Kaikōura earthquake.

6.2. Similarities between abrupt co-seismic and slow-moving post-seismic deformations

My analyses on the spatial distribution of surface deformations over the study area with respect to various environmental variables provided some new insight helping us to better understand factors governing hillslope deformation in post-seismic periods. In fact, some of those observations, which are discussed below, also showed similarities with variables controlling the spatial distribution of co-seismic landslides.

For instance, analysing the mean annual LOS deformation velocity of pre- and post-Kaikōura with elevation and slope angle in the former case, and with elevation, slope angle and PGA in the latter case reveals some interesting results which haven't been explored in other studies concerning evolution of hillslopes having active movements. Firstly, the PS having deformation between -10 mm/yr and +10 mm/yr is observed all over the study area during both the pre- and post-Kaikōura phase. However, most of the PS that is moving away from the sensor having deformation velocity less than -10 mm/yr are seen in regions with higher altitude and large slope angle, while PS that are moving towards the sensor with a deformation velocity greater than +10 mm/yr are observed in lower elevations and slope angle (see Figure 26 and Figure 29). This observation is true in the case of both pre- and post-Kaikōura phases. It is contemplated that the PS experiencing negative deformation velocity (movement away from the sensor) are mostly related to the hillslope activities, while those experiencing positive deformation velocity (movement towards sensor) are chiefly associated with the fluvial processes that take place in the foothills of the study area.

Another important revelation that has been found in this research is the relationship between post-seismic deformation velocity and PGA recorded during the main shock of the 2016 Kaikōura earthquake. From examining the spatial distribution of active PS over the study area, it is found that most of the VSM PS detected in the post-Kaikōura phase are concentrated around rupturing zone where the landscape was exposed to higher ground shaking during the 2016 mainshock. Such an observation is also valid for the co-seismic landslides triggered by the 2016 Kaikōura earthquake, as majority of the landslides occurred close to the fault rupture zone (Massey et al., 2020).

More specifically, nearly most of the larger negative (-40 to -60 mm/yr) and positive (20 to 40 mm/yr) deformation velocities are associated with PGA greater than 0.6 g. Such a trend is also witnessed in the case of distribution of co-seismic landslides triggered by the 2016 Kaikōura earthquake, where three quartiles of co-seismic landslide distribution are observed in places that experienced PGA between 0.5 g and 0.7 g (Tanyaş et al., 2022). Similarly, by analysing more than 30 earthquake events and co-seismic deformation, it is found by Petricca et al. (2021) that higher deformation is often associated with the region experiencing elevated PGA. Huang et al. (2017) reported similar findings wherein the deep-seated landslides triggered by the 2016 Amatrice earthquake (Mw=6.2) in Italy had PGA larger than 0.5 g. In the same line with the co-seismic landslide literature, I also found out that the earthquake legacy effect is also more persistent on hillslopes exposed to strong ground shaking.

Also, VSM PS detected after the 2016 Kaikōura earthquake impact mostly appears in the higher elevated landforms such as slope, spur, ridge, and summit than in the landforms that are found in the lower altitudes such as footslope and depression landforms (see Figure 40). Such observation is also consistent with that of co-seismic landslides triggered during the mainshock of the 2016 Kaikōura earthquake (Tanyaş et al., 2022). This finding provides evidence that the occurrence of active PS in the higher section of the topographic profile is associated with topographic amplification, which is so far reported only in the case of co-seismic landslides (Rizzitano et al., 2014). In addition, such a distribution can also be slightly attributed to the fact that the higher topographic region of the study area is mostly devoid of vegetation, while the lower terrain other than the drainage system is covered with dense vegetation. Thus, higher PS density can be observed in the higher topographic profile than the other except for the valley region (see Figure 40).

Overall, the results of this study suggest that the impact of the 2016 Kaikōura earthquake has massively increased the mean annual LOS deformation velocity by 130% in the study area during the post-Kaikōura phase till 2018. Given the fact that the region is affected by a large magnitude earthquake that involves surface rupture of more than 11 fault planes (Hamling et al., 2017), itself is enough to support the surge in the post-seismic deformation velocity. In fact, the increase in the average annual deformation velocity in the LOS direction is largely observed near the fault rupture plane, as one can expect. Such an abrupt increase in the LOS deformation velocity is also observed in the case of the 2015 Gorkha earthquake, even two years after the event, which had the same magnitude as the 2016 Kaikōura earthquake (Bekaert et al., 2020).

The study area is mostly covered by greywacke formation and as a natural consequence of this a large quantity of the detected active PS is observed in greywacke, which is a sedimentary rock type (see Figure 41). Before the earthquake, most of the active PS were observed weakly consolidated conglomerate and mudstone next to greywacke (see Figure 41a). After the earthquake, limestone had the most very slow-moving PS pixels, while the alluvium flood plain consisted of the most very slow-moving PS after the greywacke (see Figure 41b). Xu et al. (2021) documented that sedimentary rocks are largely associated with shallow and modest active hillslopes owing to their higher shear strength than compared to metaphoric rocks. However, I observed a tremendous surge in the VSM PS in regions covered by greywacke during the post-Kaikōura phase than in the pre-Kaikōura phase. This can also be due to the reduction in the shear strength of the greywacke caused by the intense ground shaking during the mainshock of the Kaikōura earthquake (Brain et al., 2017). In addition, the distribution of active PS over different lithology type is in line with that of co-seismic landslides that occurred during the 2016 Kaikōura earthquake (Tanyaş et al., 2022).

6.3. Justification of choices made during InSAR processing

In this research, freely available C-band Sentinel-1 SLC IW mode dataset having a spatial resolution of 5 × 20 m and polarisation of VV is used for InSAR processing and deformation measurements extraction. The processing of interferograms is separated for the pre- and post- Kaikōura phases rather than processing them in a single stack. The analysis period of the pre-Kaikōura phase is between 28 October 2014 and 10 November 2016, while the time window of the post-Kaikōura phase is right after the mainshock of the Kaikōura earthquake from 16 November 2016 till 24 December 2018. Till the start of the Sentinel-1 B sensor from 2016, images are available for each 24 days rather than 12 days. Owing to which during the pre-Kaikōura phase, there are only 27 images within a gap of 745 days, while there are 67 images within a similar gap of 769 days during the post-Kaikōura phase (See Figure 12 and Table 3). This study satisfies the minimum requirement for at least 25 images spanning more than a year to extract reliable deformation measurements using the PSI technique (Colesanti et al., 2003; Hooper et al., 2007). In addition, both during pre- and post-Kaikōura phases, data covering slightly more than two years (730 days) are used for PSI processing. If the data only covered less than two years, it would have been challenging to explain the mean annual deformation velocity as the actual mean velocity. The geometric decorrelation was not a problem in this research as the perpendicular baselines of images are lesser than 200 m.

In this study, split of the pre- and post- seismic phases is carried out to eliminate the potential phase aliasing effect that is associated with the co-seismic deformation owing to the sudden acceleration in the deformation (Manconi, 2021). Such analysing strategy is also followed because of the limitation of the PSI technique in identifying coherent radar signals (PS) over a long time period because of temporal decorrelation arising from growth of vegetation, intense precipitation, and snowing seasons, which can greatly affect the PS selection (Bekaert et al., 2020; Hanssen, 2001). Such separation of the interferometric stack processing before and after the seismic shaking is already been carried out in previous studies analysing active landslides before and after the 2015 Gorkha earthquake (Mw = 7.8, Bekaert et al., 2020) and 2017 Jiuzhaigou earthquake (Mw =7, Cai et al., 2022). Even though the previously mentioned studies have used SBAS technique for the extraction of spatio-temporal deformation measurements, they have separated the analysis period before and after the intense seismic shaking in order to neglect the co-seismic displacements similar to the case in this research. In this regard, this research is also the first to use the PSI technique for monitoring the evolution of hillslopes before and after the impact of an earthquake instead of using the more computationally intensive SBAS approach for such a large area of about 2300 km^2. This is also the main reason for this study to consider the PSI technique for extracting spatio-temporal measurements, which is relatively less computationally demanding than SBAS (Aslan et al., 2020). The previous studies that examined active hillslopes before and after an earthquake performed their analysis in a comparatively smaller region than this research (Bekaert et al., 2020; Cai et al., 2022; Cheaib et al., 2022; Lacroix et al., 2022). However, there are certain limitations of using PSI that can be overcome by employing the SBAS approach, which is further elaborated in the limitation section.

Assigning an appropriate ADI value is challenging in order to select high-density PS owing to the low coherence as the study area is mostly covered by dense vegetation and hardly has any major artificial structures. Even though the higher elevated regions are less covered by vegetation, setting a lower ADI threshold value similar to Aslan et al. (2022) and (2020) will result in lower PS density. Therefore, in this research, an ADI threshold of 0.42 is set for both pre- and post-Kaikōura phases of PSI processing. Multiple studies have employed such high ADI value, especially in mountain regions covered by high vegetation and having less impervious structures (Dong et al., 2018; Liu et al., 2022). However, even after defining a higher ADI value, it can be observed from Table 4 that PS density per km^2 nearly diminishes to half during the post-Kaikōura period, which can be attributed to temporal decorrelation arising from various factors such as regrowth of vegetation in hillslopes affected by coseismic displacement. In addition, the precipitation measurement from CHIRPS shows that 2018 received the highest maximum amount of rainfall experienced in the last 30 years (see Figure 9). These difficulties of applying the InSAR technique to the area under examination could also be counted as reasons for the lack of similar studies on this site so far.

6.4. Limitations

Even though PSInSAR-based sub-meter evolution monitoring and mapping of hillslopes have a good effectiveness, but it also has certain limitations. The first and foremost challenge in using the PSI approach is the loss of temporal correlation, which can arise from many factors, including high precipitation, snowfall and growth of vegetation (Bekaert et al., 2020; Hanssen, 2001). These reasons inhibited in acquiring PS pixels over highly vegetated regions of the hillslopes, while only those scarp regions devoid of vegetation cover and dense snowfall were observed to contain PS pixels (see Figure 49). Such a disadvantage of temporal decorrelation can be reduced by utilising a longer wavelength such as L-band images, which can penetrate through the dense vegetation cover (Xu et al., 2021). However, it should be also noted that shorter wavelength data such as C-band images is extremely responsive in capturing deformation signals (van Natijne et al., 2022). In addition, employing other MT-InSAR technique such as SBAS can help in increasing the density of captured deformation measurements over space as its characteristics allows selecting DS along with PS (Chen et al., 2021).

The second constraint of this research is the unavailability of descending flight direction images of Sentinel-1, which inhibited the decomposition of LOS deformation into horizontal and vertical components. This drawback is overcome in this research by making assumptions to project the mean annual LOS deformation velocity into downslope deformation velocity using relevant literature as support (Aslan et al., 2020; Notti et al., 2014). Therefore, this research utilised LOS deformation further to detect active PS in accordance with the hillslope velocity classification of Cruden and Varnes (1996). Such an approach is not uncommon, as previous studies have also utilised the LOS deformation velocity for identifying active hillslopes (Bayer et al., 2018; Bekaert et al., 2020; Cheaib et al., 2022; Lacroix et al., 2022).

The next challenge is that InSAR is highly effective to detect the deformation that occurs parallel direction of LOS than those that happen perpendicular to the flight direction (Xu et al., 2021) owing to its right-looking nature. In this study, a large number of hillslopes face south-east direction while there is also considerable amount of hillslopes that are seen facing north and south direction. In addition, even though InSAR based deformation measurements are reported to be in line with those recorded in GNSS stations (Cigna et al., 2021), the unavailability of GNSS station data from the study site to evaluate the reliability of the extracted surface deformation measurement is also a major limitation in this study.

It should also be noted that hillslopes with sub-meter deformations are only identified and monitored in this study. Therefore, those hillslope that are reported to be stable in this research could also experience rapid movements or failures in the post-seismic phase. This is because PS-InSAR based approach can only detect and capture deformation measurements less than a meter. In addition, there are no studies available to my knowledge documenting the post-seismic rapid landsliding in the study area, thus, it is difficult to say if the stable slopes reported in this study are actually stable. In addition, in the post-seismic phase, there are active movements that are a mix of tectonic and landsliding-related movements, which are not explored. In addition, this study doesn't correlate the precipitation measurements with the deformation measurement mainly because of the coarse spatial resolution (about 5 km) of the CHIRPS dataset.

7. CONCLUSION AND RECOMMENDATION

7.1. Conclusion

This research developed a new systematic approach for identifying extremely slow- and very slow-moving hillslopes in post-seismic periods. Specifically, I examined pre- and post- seismic hillslope deformations in the area affected by the 2016 Kaikōura earthquake and monitored their sub-meter evolution using freely available Sentinel-1 images through the PSI approach. The extracted surface deformation using PSI approach showed that an abrupt increase in the post-seismic deformations occurred following the intense ground shaking. The results of this study also showed that the regions affected by higher ground shaking exhibited also higher deformation in the post-seismic phase compared to hillslopes affected by lower seismic shaking. I captured relatively high negative deformations mostly associated with a high elevation and slope steepness, while larger positive deformation is mainly observed in the lower elevation and slope steepness. However, there are a number of outliers that behave differently from this observation, which is likely due to different scattering types in PS registry.

Also, for the first time, this study integrated the use of slope units in the post-processing of surface deformation measurements which proved to be very useful in the detection of actively deforming hillslopes. The sharp increase in the number of stable hillslopes that started moving extremely slowly and very slowly after the impact of the 2016 Kaikōura earthquake and their deformation dynamics there after confirms the firm role of earthquake legacy effect on their evolution. Analysing the number of detected actively deforming hillslopes in the post-Kaikōura phase that are affected by co-seismic landslides confirms the control of co-seismic landslides on the post-seismic sub-meter hillslope evolution. Furthermore, this study revealed four hillslope evolution types, such as (i) inactive hillslope becoming active (Type I: SA), (ii) active hillslope remaining unaffected with changes in dynamics (Type II: AA), (iii) active hillslope that have become inactive (Type III: AS) and (iv) those hillslopes that are stable prior and following the earthquake (Type IV: SS), by generating a transferable and generic hillslope activity matrix for the slopes that are affected by an earthquake event.

The following section will provide answers to the research questions that are put forth in the introduction section.

i. What are the optimum configuring parameters for the PSI approach to retrieve the LOS deformation measurements of (constantly) coherent radar scatterers?

In this study, multiple parameters are configured differently from the standard values for a better extraction of surface deformation (see Table 4). Initially, the ADI is set to 0.42 for both pre- and post- Kaikōura phase analysis in order to capture have higher PS density over the highly vegetated study area. The maximum accepted uncorrelated DEM error is reduced from standard 5 m to 20 m in the second step of PSI processing. During the PS weeding stage, the threshold standard deviation for weeding pixel is fixed as 1.2, and the neighbour pixels are weeded in addition to the weeding of PS in areas having zero elevation. The 3D unwrapping method is used for unwrapping with better accuracy. The unwrapping grid size is set to 50 from the standard value of 200, and the size of the Goldstein filter's window is fixed to be 16, whereas the smoothing window is set to 365 days. In this study, GACOS dataset is used to do atmospheric phase correction.

ii. What are the differences between pre- and post-seismic mean annual LOS deformation velocity?

The mean LOS deformation velocity in the pre-Kaikōura phase ranges between -20.27 mm/yr and 20.08 mm/yr, while the same in the post-Kaikōura phase ranges from -54.10 mm/yr and 39.10 mm/yr. By comparing the mean LOS deformation velocity of pre- and post-Kaikōura phase, it is found that there is a nearly 130% absolute surge in the deformation velocity during the post-Kaikōura phase. However, the total number of PS captured during the pre-Kaikōura phase decreases by 46.5% in the post-Kaikōura phase.

iii. How does deformation measurement change across basic morphometric variables such as elevation and slope steepness during the pre- and post-seismic phase?

It is found that in this study area, during both pre- and post-seismic phases, PS having comparatively larger negative deformation velocity of more than -10 mm/yr are observed in higher altitudes associated with steeper slopes while the PS having larger negative deformation than 10mm/yr are observed in lower elevations having lesser slope gradient. This is an important finding as larger negative deformations are associated with hillslope deformation processes while greater positive deformations are linked to the fluvial processes.

iv. How does deformation measurement change across places experiencing different PGA during the post-seismic phase?

The PS having larger deformation velocity, either positive (20 to 40 mm/yr) or negative (-30 to -60 mm/yr) has been affected by PGA higher than 0.6 g. This shows that regions affected by higher ground shaking during the 2016 Kaikōura earthquake have higher deformation in the post-seismic phase.

v. What are the different landforms and lithologies that control the active deformations?

In this study, a large number of PS exhibiting active deformations are observed in landforms associated with higher topographic profile such as slope, spur, ridge, hollow, and summit during both pre- and post-Kaikōura phase.

Most of the actively deforming PS in both pre- and post-Kaikōura phases is observed in greywacke. During pre-Kaikōura period, more actively deforming PS, especially the extremely slow-moving (± 10 mm/yr $\geqslant$ VLOS < ± 16 mm/yr) ones, are observed across weakly consolidated conglomerate and mudstone. But during the post-seismic phase, limestone had the most very slow-moving PS pixels (VLOS $\geqslant \pm$ 16 mm/yr), while the alluvium flood plain consisted of the most extremely slow-moving PS after the greywacke.

vi. What is the best critical stability threshold that can be defined to detect and characterise the active PS?

In this study, those PS having mean LOS deformation velocity equal or greater than ± 10 mm/yr are classified as active points, while the rest are excluded as stable. Such a critical stability threshold is defined to avoid confusion in using either one or two standard deviations for PS velocity and b) using the hillslope velocity classification of Cruden and Varnes (1996). In this study, both the approaches summarized above are coupled to differentiate active PS from stable ones. In addition, identified active PS are also sub-categorized as extremely slow-moving (± 10 mm/yr $\geqslant$ VLOS < ± 16 mm/yr) and very slow-moving (VLOS $\geqslant \pm$ 16 mm/yr) PS.

vii. What are the different types of post-seismic sub-meter hillslope evolution captured in this study?

By proposing a post-seismic hillslope deformation matrix, this study captured four hillslope deformation evolution types. They are (i) inactive hillslope becoming active (Type I: SA), (ii) active hillslope remaining unaffected with changes in dynamics (Type II: AA), (iii) active hillslope that have become inactive (Type III: AS) and (iv) those hillslopes that are stable prior and following the earthquake (Type IV: SS). The hillslope activity matrix could be applied to other earthquake-affected areas to systematically and consistently examine hillslope evolution processes in post-seismic periods. This study found 239 hillslopes in type I, four hillslopes in type II, five hillslopes in type III, and 4856 hillslopes in the last type IV.

7.2. Recommendations

For the future scope of this research, the following recommendation are provided:

- Using GNSS station or other geodetic data for evaluating and improving the accuracy of the surface deformation measurements extracted in this research.

- Exploring the factors controlling the hillslope deformation in a multivariate scheme could help us to improve our understanding on the impact of earthquake legacy effect on the entire region. In this context, the relationship between the deformation measurements with rainfall, soil moisture, land surface temperature and areal fraction of snow cover as well as various morphometric and geologic variables should be studied further.

- To improve the detection of active PS, artificial intelligence such as recurrent neural network can be used to identify those PS that behave different from stable ones.

- The analysis can be further extended to the available Sentinel-1 images between 2019 and 2022 to understand the evolution of hillslopes in those time period which is not performed in this research. Such analysis could reveal the recovery time of active hillslopes to return to its stable state. So far, no study have used deformation measurement to study the recovery time of active hillslopes.

- Use of higher resolution DEM than SRTM 1-arc sec DEM, (e.g. TanDEM) could improve the obtained deformation measurements.

- The results of this study can be further used in the assessment of hazard and risk in the region.

- The seasonal deformation pattern of active hillslopes can be further studied with the help of higher spatial resolution precipitation data such as rain gauge data.

- The investigation of scattering types of PS, including surface, volume and double bounce scattering, using multi-polarization SAR data (e.g. Sentinel-1 SAR with VV and VH) may contribute to better data interpretation.

LIST OF REFERENCES

Alvioli, M., Marchesini, I., Reichenbach, P., Rossi, M., Ardizzone, F., Fiorucci, F., Guzzetti, F., 2016. Automatic delineation of geomorphological slope units with r.slopeunits v1.0 and their optimization for landslide susceptibility modeling. Geoscientific Model Development 9, 3975–3991. https://doi.org/10.5194/GMD-9-3975-2016

Alvioli, M., Mondini, A.C., Fiorucci, F., Cardinali, M., Marchesini, I., 2018. Topography-driven satellite imagery analysis for landslide mapping. http://www.tandfonline.com/action/journalInformation?show=aimsScope&journalCode=tgnh20#.VsXodSCLRhE 9, 544–567. https://doi.org/10.1080/19475705.2018.1458050

Artese, S., Perrelli, M., 2018. Monitoring a Landslide with High Accuracy by Total Station: A DTM-Based Model to Correct for the Atmospheric Effects. Geosciences 2018, Vol. 8, Page 46 8, 46. https://doi.org/10.3390/GEOSCIENCES8020046

Aslan, G., de Michele, M., Raucoules, D., Bernardie, S., Cakir, Z., 2021. Transient motion of the largest landslide on earth, modulated by hydrological forces. Scientific Reports 2021 11:1 11, 1–12. https://doi.org/10.1038/s41598-021-89899-6

Aslan, G., Foumelis, M., Raucoules, D., de Michele, M., Bernardie, S., Cakir, Z., 2020. Landslide mapping and monitoring using persistent scatterer interferometry (PSI) technique in the French alps. Remote Sensing 12. https://doi.org/10.3390/RS12081305

Badoux, A., Andres, N., Techel, F., Hegg, C., 2016. Natural hazard fatalities in Switzerland from 1946 to 2015. Natural Hazards and Earth System Sciences 16, 2747–2768. https://doi.org/10.5194/nhess-16-2747-2016

Balbi, E., Terrone, M., Faccini, F., Scafidi, D., Barani, S., Tosi, S., Crispini, L., Cianfarra, P., Poggi, F., Ferretti, G., 2021. Persistent Scatterer Interferometry and Statistical Analysis of Time-Series for Landslide Monitoring: Application to Santo Stefano d'Aveto (Liguria, NW Italy). Remote Sensing 2021, Vol. 13, Page 3348 13, 3348. https://doi.org/10.3390/RS13173348

Bamler, R., Hartl, P., 1998. Synthetic aperture radar interferometry. Inverse Problems 14, R1. https://doi.org/10.1088/0266-5611/14/4/001

Bardi, F., Raspini, F., Frodella, W., Lombardi, L., Nocentini, M., Gigli, G., Morelli, S., Corsini, A., Casagli, N., 2017. Monitoring the Rapid-Moving Reactivation of Earth Flows by Means of GB-InSAR: The April 2013 Capriglio Landslide (Northern Appennines, Italy). Remote Sensing 2017, Vol. 9, Page 165 9, 165. https://doi.org/10.3390/RS9020165

Bayer, B., Simoni, A., Mulas, M., Corsini, A., Schmidt, D., 2018. Deformation responses of slow moving landslides to seasonal rainfall in the Northern Apennines, measured by InSAR. Geomorphology 308, 293–306. https://doi.org/10.1016/j.geomorph.2018.02.020

Bayer, B., Simoni, A., Schmidt, D., Bertello, L., 2017. Using advanced InSAR techniques to monitor landslide deformations induced by tunneling in the Northern Apennines, Italy. Engineering Geology 226, 20–32. https://doi.org/10.1016/j.enggeo.2017.03.026

Beck, H.E., Zimmermann, N.E., McVicar, T.R., Vergopolan, N., Berg, A., Wood, E.F., 2018. Present and future Köppen-Geiger climate classification maps at 1-km resolution. Scientific Data 2018 5:1 5, 1–12. https://doi.org/10.1038/sdata.2018.214

Bekaert, D.P.S., Handwerger, A.L., Agram, P., Kirschbaum, D.B., 2020. InSAR-based detection method for mapping and monitoring slow-moving landslides in remote regions with steep and mountainous terrain: An application to Nepal. Remote Sensing of Environment 249, 111983. https://doi.org/10.1016/j.rse.2020.111983

Bekaert, D.P.S., Hooper, A., Wright, T.J., 2015. A spatially variable power law tropospheric correction technique for InSAR data. Journal of Geophysical Research: Solid Earth 120, 1345–1356. https://doi.org/10.1002/2014JB011558

Berardino, P., Fornaro, G., Lanari, R., Sansosti, E., 2002. A new algorithm for surface deformation monitoring based on small baseline differential SAR interferograms. IEEE Transactions on Geoscience and Remote Sensing 40, 2375–2383. https://doi.org/10.1109/TGRS.2002.803792

Bianchini, S., Herrera, G., Mateos, R.M., Notti, D., Garcia, I., Mora, O., Moretti, S., 2013. Landslide Activity Maps Generation by Means of Persistent Scatterer Interferometry. Remote Sensing 2013, Vol. 5, Pages 6198-6222 5, 6198–6222. https://doi.org/10.3390/RS5126198

Blanco-Sànchez, P., Mallorquí, J.J., Duque, S., Monells, D., 2008. The Coherent Pixels Technique (CPT): An Advanced DInSAR Technique for Nonlinear Deformation Monitoring. Earth Sciences and Mathematics 1167–1193. https://doi.org/10.1007/978-3-7643-8907-9_10

Blasco, J.M.D., Fernandez, D., Foumelis, M., Blasco, J.D., Desnos, Y.-L., Engdahl, M., Fernández, D., Veci, L., Lu, J., Wong, C., 2018. ESA SNAP – Stamps integrated processing for sentinel-1 persistent scatterer interferometry, in: International Geoscience and Remote Sensing Symposium (IGARSS). IEEE, pp. 1364–1367. https://doi.org/10.1109/IGARSS.2018.8519545

Blasco, J.M.D., Foumelis, M., Stewart, C., Hooper, A., 2019. Measuring Urban Subsidence in the Rome Metropolitan Area (Italy) with Sentinel-1 SNAP-StaMPS Persistent Scatterer Interferometry. Remote Sensing 2019, Vol. 11, Page 129 11, 129. https://doi.org/10.3390/RS11020129

Bontemps, N., Lacroix, P., Larose, E., Jara, J., Taipe, E., 2020a. Rain and small earthquakes maintain a slow-moving landslide in a persistent critical state. Nature Communications 11, 1–10. https://doi.org/10.1038/s41467-020-14445-3

Bontemps, N., Lacroix, P., Larose, E., Jara, J., Taipe, E., 2020b. Rain and small earthquakes maintain a slow-moving landslide in a persistent critical state. Nature Communications 11, 1–10. https://doi.org/10.1038/s41467-020-14445-3

Booth, A.M., Roering, J.J., Rempel, A.W., 2013. Topographic signatures and a general transport law for deep-seated landslides in a landscape evolution model. Journal of Geophysical Research: Earth Surface 118, 603–624. https://doi.org/10.1002/jgrf.20051

Bouali, E.H., Oommen, T., Escobar-Wolf, R., 2018. Mapping of slow landslides on the Palos Verdes Peninsula using the California landslide inventory and persistent scatterer interferometry. Landslides 15, 439–452. https://doi.org/10.1007/S10346-017-0882-Z/TABLES/6

Brain, M.J., Rosser, N.J., Tunstall, N., 2017. The control of earthquake sequences on hillslope stability. Geophysical Research Letters 44, 865–872. https://doi.org/10.1002/2016GL071879

Braun, A., Höser, T., Delgado Blasco, J.M., 2020. Elevation change of Bhasan Char measured by persistent scatterer interferometry using Sentinel-1 data in a humanitarian context. https://doi.org/10.1080/22797254.2020.1789507 54, 1–18. https://doi.org/10.1080/22797254.2020.1789507

Cai, J., Zhang, L., Dong, J., Dong, X., Li, M., Xu, Q., Liao, M., 2022. Detection and characterization of slow-moving landslides in the 2017 Jiuzhaigou earthquake area by combining satellite SAR observations and airborne Lidar DSM. Engineering Geology 305, 106730. https://doi.org/10.1016/J.ENGGEO.2022.106730

Cao, Y., Hamling, I., Massey, C., Upton, P., 2022. Slow-moving landslides triggered by the 2016 Mw 7.8 Kaikōura earthquake, New Zealand: a new InSAR phase-gradient based time-series approach. https://doi.org/10.1002/ESSOAR.10512014.1

Carlà, T., Intrieri, E., Raspini, F., Bardi, F., Farina, P., Ferretti, A., Colombo, D., Novali, F., Casagli, N., 2019. Perspectives on the prediction of catastrophic slope failures from satellite InSAR. Scientific Reports 2019 9:1 9, 1–9. https://doi.org/10.1038/s41598-019-50792-y

Chang, L., Dollevoet, R.P.B.J., Hanssen, R.F., 2017. Nationwide Railway Monitoring Using Satellite SAR Interferometry. IEEE Journal of Selected Topics in Applied Earth Observations and Remote Sensing 10, 596–604. https://doi.org/10.1109/JSTARS.2016.2584783

Chang, L., Hanssen, R.F., 2014. Detection of cavity migration and sinkhole risk using radar interferometric time series. Remote Sensing of Environment 147, 56–64. https://doi.org/10.1016/J.RSE.2014.03.002

Chaussard, E., Wdowinski, S., Cabral-Cano, E., Amelung, F., 2014. Land subsidence in central Mexico detected by ALOS InSAR time-series. Remote Sensing of Environment 140, 94–106. https://doi.org/10.1016/J.RSE.2013.08.038

Cheaib, A., Lacroix, P., Zerathe, S., Jongmans, D., Ajorlou, N., Doin, M.P., Hollingsworth, J., Abdallah, C., 2022. Landslides induced by the 2017 Mw7.3 Sarpol Zahab earthquake (Iran). Landslides 19, 603–619. https://doi.org/10.1007/S10346-021-01832-0/FIGURES/10

Chen, M., Tang, C., Xiong, J., Shi, Q.Y., Li, N., Gong, L.F., Wang, X.D., Tie, Y., 2020. The long-term evolution of landslide activity near the epicentral area of the 2008 Wenchuan earthquake in China. Geomorphology 367, 107317. https://doi.org/10.1016/J.GEOMORPH.2020.107317

Chen, X., Tessari, G., Fabris, M., Achilli, V., Floris, M., 2021. Comparison Between PS and SBAS InSAR Techniques in Monitoring Shallow Landslides 155–161. https://doi.org/10.1007/978-3-030-60311-3_17

Cigna, F., Bianchini, S., Casagli, N., 2013. How to assess landslide activity and intensity with Persistent Scatterer Interferometry (PSI): The PSI-based matrix approach. Landslides 10, 267–283. https://doi.org/10.1007/S10346-012-0335-7/FIGURES/11

Cigna, F., Ramírez, R.E., Tapete, D., 2021. Accuracy of Sentinel-1 PSI and SBAS InSAR Displacement Velocities against GNSS and Geodetic Leveling Monitoring Data. Remote Sensing 2021, Vol. 13, Page 4800 13, 4800. https://doi.org/10.3390/RS13234800

Colesanti, C., Ferretti, A., Prati, C., Rocca, F., 2003. Monitoring landslides and tectonic motions with the Permanent Scatterers Technique. Engineering Geology 68, 3–14. https://doi.org/10.1016/S0013-7952(02)00195-3

Colesanti, C., Wasowski, J., 2006. Investigating landslides with space-borne Synthetic Aperture Radar (SAR) interferometry. Engineering Geology 88, 173–199. https://doi.org/10.1016/j.enggeo.2006.09.013

Corominas, J., Moya, J., Lloret, A., Gili, J.A., Angeli, M.G., Pasuto, A., Silvano, S., 2000. Measurement of landslide displacements using a wire extensometer. Engineering Geology 55, 149–166. https://doi.org/10.1016/S0013-7952(99)00086-1

Crosetto, M., Monserrat, O., Cuevas-González, M., Devanthéry, N., Crippa, B., 2016. Persistent Scatterer Interferometry: A review. ISPRS Journal of Photogrammetry and Remote Sensing 115, 78–89. https://doi.org/10.1016/J.ISPRSJPRS.2015.10.011

Cruden, D., Varnes, D., 1996. Landslide types and processes, in: Turner, A., Schuster, R. (Eds.), Landslides Investigation and Mitigation. ransportation research board, US National Research Council., Washington DC, pp. 36–75.

Debella-Gilo, M., Kääb, A., 2012. Measurement of surface displacement and deformation of mass movements using least squares matching of repeat high resolution satellite and aerial images. Remote Sensing 4, 43–67. https://doi.org/10.3390/rs4010043

Desrues, M., Lacroix, P., Brenguier, O., 2019. Satellite pre-failure detection and in situ monitoring of the landslide of the tunnel du Chambon, French alps. Geosciences (Switzerland) 9, 313. https://doi.org/10.3390/geosciences9070313

Diederichs, A., Nissen, E.K., Lajoie, L.J., Langridge, R.M., Malireddi, S.R., Clark, K.J., Hamling, I.J., Tagliasacchi, A., 2019. Unusual kinematics of the Papatea fault (2016 Kaikōura earthquake) suggest anelastic rupture. Science Advances 5. https://doi.org/10.1126/SCIADV.AAX5703/SUPPL_FILE/AAX5703_SPARSE_ICP_CODE_AND_DOCUMENTATION.TAR

Ding, C., Feng, G., Liao, M., Tao, P., Zhang, L., Xu, Q., 2021. Displacement history and potential triggering factors of Baige landslides, China revealed by optical imagery time series. Remote Sensing of Environment 254, 112253. https://doi.org/10.1016/j.rse.2020.112253

Dong, J., Zhang, L., Tang, M., Liao, M., Xu, Q., Gong, J., Ao, M., 2018. Mapping landslide surface displacements with time series SAR interferometry by combining persistent and distributed scatterers: A case study of Jiaju landslide in Danba, China. Remote Sensing of Environment 205, 180–198. https://doi.org/10.1016/J.RSE.2017.11.022

Dowling, C.A., Santi, P.M., 2014. Debris flows and their toll on human life: A global analysis of debris-flow fatalities from 1950 to 2011. Natural Hazards 71, 203–227. https://doi.org/10.1007/s11069-013-0907-4

Duan, W., Zhang, H., Wang, C., Tang, Y., 2020. Multi-Temporal InSAR Parallel Processing for Sentinel-1 Large-Scale Surface Deformation Mapping. Remote Sensing 2020, Vol. 12, Page 3749 12, 3749. https://doi.org/10.3390/RS12223749

Duputel, Z., Rivera, L., 2017. Long-period analysis of the 2016 Kaikoura earthquake. Physics of the Earth and Planetary Interiors 265, 62–66. https://doi.org/10.1016/J.PEPI.2017.02.004

Fan, X., Domènech, G., Scaringi, G., Huang, R., Xu, Q., Hales, T.C., Dai, L., Yang, Q., Francis, O., 2018. Spatio-temporal evolution of mass wasting after the 2008 Mw 7.9 Wenchuan earthquake revealed by a detailed multi-temporal inventory. Landslides 2018 15:12 15, 2325–2341. https://doi.org/10.1007/S10346-018-1054-5

Fan, X., Scaringi, G., Korup, O., West, A.J., van Westen, C.J., Tanyas, H., Hovius, N., Hales, T.C., Jibson, R.W., Allstadt, K.E., Zhang, L., Evans, S.G., Xu, C., Li, G., Pei, X., Xu, Q., Huang, R., 2019. Earthquake-Induced Chains of Geologic Hazards: Patterns, Mechanisms, and Impacts. Reviews of Geophysics 57, 421–503. https://doi.org/10.1029/2018RG000626

Fattahi, H., Agram, P., Simons, M., 2017. A Network-Based Enhanced Spectral Diversity Approach for TOPS Time-Series Analysis. IEEE Transactions on Geoscience and Remote Sensing 55, 777–786. https://doi.org/10.1109/TGRS.2016.2614925

Ferretti, A., Fumagalli, A., Novali, F., Prati, C., Rocca, F., Rucci, A., 2011. A new algorithm for processing interferometric data-stacks: SqueeSAR. IEEE Transactions on Geoscience and Remote Sensing 49, 3460–3470. https://doi.org/10.1109/TGRS.2011.2124465

Ferretti, A., Prati, C., Rocca, F., 2001. Permanent scatterers in SAR interferometry. IEEE Transactions on Geoscience and Remote Sensing 39, 8–20. https://doi.org/10.1109/36.898661

Ferretti, A., Prati, C., Rocca, F., 2000. Nonlinear subsidence rate estimation using permanent scatterers in differential SAR interferometry. IEEE Transactions on Geoscience and Remote Sensing 38, 2202–2212. https://doi.org/10.1109/36.868878

Ferrigno, F., Gigli, G., Fanti, R., Intrieri, E., Casagli, N., 2017. GB-InSAR monitoring and observational method for landslide emergency management: The Montaguto earthflow (AV, Italy). Natural Hazards and Earth System Sciences 17, 845–860. https://doi.org/10.5194/NHESS-17-845-2017

Fiaschi, S., Mantovani, M., Frigerio, S., Pasuto, A., Floris, M., 2017. Testing the potential of Sentinel-1A TOPS interferometry for the detection and monitoring of landslides at local scale (Veneto Region, Italy). Environmental Earth Sciences 76, 1–13. https://doi.org/10.1007/S12665-017-6827-Y/FIGURES/9

Foumelis, M., Blasco, J.M.D., Desnos, Y.L., Engdahl, M., Fernández, D., Veci, L., Lu, J., Wong, C., 2018. ESA SNAP - Stamps integrated processing for Sentinel-1 persistent scatterer interferometry. International Geoscience and Remote Sensing Symposium (IGARSS) 2018-July, 1364–1367. https://doi.org/10.1109/IGARSS.2018.8519545

Froude, M.J., Petley, D.N., 2018. Global fatal landslide occurrence from 2004 to 2016. Natural Hazards and Earth System Sciences 18, 2161–2181. https://doi.org/10.5194/nhess-18-2161-2018

Fruneau, B., Achache, J., Delacourt, C., 1996. Observation and modelling of the Saint-Étienne-de-Tinée landslide using SAR interferometry. Tectonophysics 265, 181–190. https://doi.org/10.1016/S0040-1951(96)00047-9

Funk, C., Peterson, P., Landsfeld, M., Pedreros, D., Verdin, J., Shukla, S., Husak, G., Rowland, J., Harrison, L., Hoell, A., Michaelsen, J., 2015. The climate hazards infrared precipitation with stations—a new environmental record for monitoring extremes. Scientific Data 2015 2:1 2, 1–21. https://doi.org/10.1038/sdata.2015.66

Gabriel, A.K., Goldstein, R.M., Zebker, H.A., 1989. Mapping small elevation changes over large areas: Differential radar interferometry. Journal of Geophysical Research: Solid Earth 94, 9183–9191. https://doi.org/10.1029/JB094IB07P09183

García, A., Hördt, A., Fabian, M., 2010. Landslide monitoring with high resolution tilt measurements at the Dollendorfer Hardt landslide, Germany. Geomorphology 120, 16–25. https://doi.org/10.1016/J.GEOMORPH.2009.09.011

Gariano, S.L., Guzzetti, F., 2016. Landslides in a changing climate. Earth-Science Reviews. https://doi.org/10.1016/j.earscirev.2016.08.011

Geertsema, M., Highland, L., Vaugeouis, L., 2009. Environmental impact of landslides, in: Landslides - Disaster Risk Reduction. Springer Science and Business Media, LLC, pp. 589–607. https://doi.org/10.1007/978-3-540-69970-5_31

Geertsema, M., Pojar, J.J., 2007. Influence of landslides on biophysical diversity - A perspective from British Columbia. Geomorphology 89, 55–69. https://doi.org/10.1016/j.geomorph.2006.07.019

Greif, V., Vlcko, J., 2012. Monitoring of post-failure landslide deformation by the PS-InSAR technique at Lubietova in Central Slovakia. Environmental Earth Sciences 66, 1585–1595. https://doi.org/10.1007/s12665-011-0951-x

Gruber, F.E., Schaber, E., Baruck, J., Geitner, C., 2019. How and to What Extent Does Topography Control the Results of Soil Function Assessment: A Case Study From the Alps in South Tyrol (Italy). Soil Systems 2019, Vol. 3, Page 18 3, 18. https://doi.org/10.3390/SOILSYSTEMS3010018

Guo, P., Han, Z. jun, Ran, H. liu, Luo, J. hong, Wu, G., Yuan, R. mao, 2019. Co-seismic surface rupture of Papatea fault and reactivation mechanism of the Clarence landslide during the 2016 M w7.8 Kaikoura earthquake, New Zealand. Bulletin of Engineering Geology and the Environment 78, 3055–3068. https://doi.org/10.1007/S10064-018-1338-Y/FIGURES/15

Guzzetti, F., Reichenbach, P., Cardinali, M., Galli, M., Ardizzone, F., 2005. Probabilistic landslide hazard assessment at the basin scale. Geomorphology 72, 272–299. https://doi.org/10.1016/J.GEOMORPH.2005.06.002

Hamling, I.J., Hreinsdóttir, S., Clark, K., Elliott, J., Liang, C., Fielding, E., Litchfield, N., Villamor, P., Wallace, L., Wright, T.J., D'Anastasio, E., Bannister, S., Burbidge, D., Denys, P., Gentle, P., Howarth, J., Mueller, C., Palmer, N., Pearson, C., Power, W., Barnes, P., Barrell, D.J.A., van Dissen, R., Langridge, R., Little, T., Nicol, A., Pettinga, J., Rowland, J., Stirling, M., 2017. Complex multifault rupture during the 2016 Mw 7.8 Kaikōura earthquake, New Zealand. Science (1979) 356. https://doi.org/10.1126/SCIENCE.AAM7194/SUPPL_FILE/HAMLING.SM.PDF

Handwerger, A.L., Huang, M.H., Fielding, E.J., Booth, A.M., Bürgmann, R., 2019. A shift from drought to extreme rainfall drives a stable landslide to catastrophic failure. Scientific Reports 9, 1–12. https://doi.org/10.1038/s41598-018-38300-0

Handwerger, A.L., Roering, J.J., Schmidt, D.A., 2013. Controls on the seasonal deformation of slow-moving landslides. Earth and Planetary Science Letters 377–378, 239–247. https://doi.org/10.1016/J.EPSL.2013.06.047

Handwerger, A.L., Roering, J.J., Schmidt, D.A., Rempel, A.W., 2015. Kinematics of earthflows in the Northern California Coast Ranges using satellite interferometry. Geomorphology 246, 321–333. https://doi.org/10.1016/j.geomorph.2015.06.003

Hanssen, R.F., 2001. Radar Interferometry: Data Interpretation and Error Analysis, 1st ed, Remote Sensing and Digital Image Processing. Springer Netherlands, Dordrecht. https://doi.org/10.1007/0-306-47633-9

Haque, U., da Silva, P.F., Devoli, G., Pilz, J., Zhao, B., Khaloua, A., Wilopo, W., Andersen, P., Lu, P., Lee, J., Yamamoto, T., Keellings, D., Jian-Hong, W., Glass, G.E., 2019. The human cost of global warming: Deadly landslides and their triggers (1995–2014). Science of the Total Environment 682, 673–684. https://doi.org/10.1016/j.scitotenv.2019.03.415

Herrera, G., Mateos, R.M., García-Davalillo, J.C., Grandjean, G., Poyiadji, E., Maftei, R., Filipciuc, T.C., Jemec Auflič, M., Jež, J., Podolszki, L., Trigila, A., Iadanza, C., Raetzo, H., Kociu, A., Przyłucka, M., Kułak, M., Sheehy, M., Pellicer, X.M., McKeown, C., Ryan, G., Kopačková, V., Frei, M., Kuhn, D., Hermanns, R.L., Koulermou, N., Smith, C.A., Engdahl, M., Buxó, P., Gonzalez, M., Dashwood, C., Reeves, H., Cigna, F., Lik, P., Pauditš, P., Mikulėnas, V., Demir, V., Raha, M., Quental, L., Sandić, C., Fusi, B., Jensen, O.A., 2018. Landslide databases in the Geological Surveys of Europe. Landslides 15, 359–379. https://doi.org/10.1007/s10346-017-0902-z

Hilley, G.E., Bürgmann, R., Ferretti, A., Novali, F., Rocca, F., 2004. Dynamics of slow-moving landslides from permanent scatterer analysis. Science (1979) 304, 1952–1955. https://doi.org/10.1126/science.1098821

Hooper, A., Bekaert, D., Hussain, E., Spaans, K., 2018. StaMPS/MTI Manual Version 4.1b. Leeds, United Kingdom.

Hooper, A., Bekaert, D., Spaans, K., Arikan, M., 2012. Recent advances in SAR interferometry time series analysis for measuring crustal deformation. Tectonophysics 514–517, 1–13. https://doi.org/10.1016/J.TECTO.2011.10.013

Hooper, A., Segall, P., Zebker, H., 2007. Persistent scatterer interferometric synthetic aperture radar for crustal deformation analysis, with application to Volcán Alcedo, Galápagos. Journal of Geophysical Research: Solid Earth 112, 7407. https://doi.org/10.1029/2006JB004763

Hooper, A., Zebker, H., Segall, P., Kampes, B., 2004. A new method for measuring deformation on volcanoes and other natural terrains using InSAR persistent scatterers. Geophysical Research Letters 31, 1–5. https://doi.org/10.1029/2004GL021737

Hooper, A.J., 2008. A multi-temporal InSAR method incorporating both persistent scatterer and small baseline approaches. Geophysical Research Letters 35. https://doi.org/10.1029/2008GL034654

Howell, A., Nissen, E., Stahl, T., Clark, K., Kearse, J., van Dissen, R., Villamor, P., Langridge, R., Jones, K., 2020. Three-Dimensional Surface Displacements During the 2016 MW 7.8 Kaikōura Earthquake (New Zealand) From Photogrammetry-Derived Point Clouds. Journal of Geophysical Research: Solid Earth 125, e2019JB018739. https://doi.org/10.1029/2019JB018739

Huang, M.H., Fielding, E.J., Liang, C., Milillo, P., Bekaert, D., Dreger, D., Salzer, J., 2017. Coseismic deformation and triggered landslides of the 2016 Mw 6.2 Amatrice earthquake in Italy. Geophysical Research Letters 44, 1266–1274. https://doi.org/10.1002/2016GL071687

Huggel, C., Clague, J.J., Korup, O., 2012. Is climate change responsible for changing landslide activity in high mountains? Earth Surface Processes and Landforms 37, 77–91. https://doi.org/10.1002/ESP.2223

Hungr, O., Leroueil, S., Picarelli, L., 2014. The Varnes classification of landslide types, an update. Landslides 2014 11:2 11, 167–194. https://doi.org/10.1007/S10346-013-0436-Y

International Geotechnical Society's UNESCO Working Party on World Landslide Inventory (WP/WLI), 1995. A suggested method for describing the rate of movement of a landslide. Bull Inter Assoc Eng Geol 52, 75–78.

Intrieri, E., Raspini, F., Fumagalli, A., Lu, P., del Conte, S., Farina, P., Allievi, J., Ferretti, A., Casagli, N., 2018. The Maoxian landslide as seen from space: detecting precursors of failure with Sentinel-1 data. Landslides 15, 123–133. https://doi.org/10.1007/s10346-017-0915-7

Jelének, J., Kopačková-Strnadová, V., 2021. Synergic use of Sentinel-1 and Sentinel-2 data for automatic detection of earthquake-triggered landscape changes: A case study of the 2016 Kaikoura earthquake (Mw 7.8), New Zealand. Remote Sensing of Environment 265, 112634. https://doi.org/10.1016/J.RSE.2021.112634

Kaiser, A., Balfour, N., Fry, B., Holden, C., Litchfield, N., Gerstenberger, M., D'Anastasio, E., Horspool, N., McVerry, G., Ristau, J., Bannister, S., Christophersen, A., Clark, K., Power, W., Rhoades, D., Massey, C., Hamling, I., Wallace, L., Mountjoy, J., Kaneko, Y., Benites, R., van Houtte, C., Dellow, S., Wotherspoon, L., Elwood, K., Gledhill, K., 2017. The 2016 Kaikōura, New Zealand, Earthquake: Preliminary Seismological Report. Seismological Research Letters 88, 727–739. https://doi.org/10.1785/0220170018

Kalia, A.C., 2018. Classification of Landslide Activity on a Regional Scale Using Persistent Scatterer Interferometry at the Moselle Valley (Germany). Remote Sensing 2018, Vol. 10, Page 1880 10, 1880. https://doi.org/10.3390/RS10121880

Kang, Y., Lu, Z., Zhao, C., Xu, Y., Kim, J. woo, Gallegos, A.J., 2021. InSAR monitoring of creeping landslides in mountainous regions: A case study in Eldorado National Forest, California. Remote Sensing of Environment 258, 112400. https://doi.org/10.1016/J.RSE.2021.112400

Karanam, V., Motagh, M., Garg, S., Jain, K., 2021. Multi-sensor remote sensing analysis of coal fire induced land subsidence in Jharia Coalfields, Jharkhand, India. International Journal of Applied Earth Observation and Geoinformation 102, 102439. https://doi.org/10.1016/J.JAG.2021.102439

Keefer, D.K., 1984. Landslides caused by earthquakes. GSA Bulletin 95, 406–421.

Kincey, M.E., Rosser, N.J., Robinson, T.R., Densmore, A.L., Shrestha, R., Pujara, D.S., Oven, K.J., Williams, J.G., Swirad, Z.M., 2021. Evolution of Coseismic and Post-seismic Landsliding After the 2015 Mw 7.8 Gorkha Earthquake, Nepal. Journal of Geophysical Research: Earth Surface 126, e2020JF005803. https://doi.org/10.1029/2020JF005803

Korup, O., 2008. Rock type leaves topographic signature in landslide-dominated mountain ranges. Geophysical Research Letters 35. https://doi.org/10.1029/2008GL034157

Lacroix, P., Berthier, E., Maquerhua, E.T., 2015. Earthquake-driven acceleration of slow-moving landslides in the Colca valley, Peru, detected from Pléiades images. Remote Sensing of Environment 165, 148–158. https://doi.org/10.1016/j.rse.2015.05.010

Lacroix, P., Bièvre, G., Pathier, E., Kniess, U., Jongmans, D., 2018. Use of Sentinel-2 images for the detection of precursory motions before landslide failures. Remote Sensing of Environment 215, 507–516. https://doi.org/10.1016/j.rse.2018.03.042

Lacroix, P., Gavillon, T., Bouchant, C., Lavé, J., Mugnier, J.-L., Dhungel, S., Vernier, F., 2022. SAR and optical images correlation illuminates post-seismic landslide motion after the Mw 7.8 Gorkha earthquake (Nepal). Scientific Reports 2022 12:1 12, 1–13. https://doi.org/10.1038/s41598-022-10016-2

Lacroix, P., Handwerger, A.L., Bièvre, G., 2020. Life and death of slow-moving landslides. Nature Reviews Earth & Environment 1, 404–419. https://doi.org/10.1038/s43017-020-0072-8

Lacroix, P., Perfettini, H., Taipe, E., Guillier, B., 2014. Coseismic and postseismic motion of a landslide: Observations, modeling, and analogy with tectonic faults. Geophysical Research Letters 41, 6676–6680. https://doi.org/10.1002/2014GL061170

Lanari, R., Mora, O., Manunta, M., Mallorquí, J.J., Berardino, P., Sansosti, E., 2004. A small-baseline approach for investigating deformations on full-resolution differential SAR interferograms. IEEE Transactions on Geoscience and Remote Sensing 42, 1377–1386. https://doi.org/10.1109/TGRS.2004.828196

Lane, E.M., Borrero, J., Whittaker, C.N., Bind, J., Chagué-Goff, C., Goff, J., Goring, D., Hoyle, J., Mueller, C., Power, W.L., Reid, C.M., Williams, J.H., Williams, S.P., 2017. Effects of Inundation by the 14th November, 2016 Kaikōura Tsunami on Banks Peninsula, Canterbury, New Zealand. Pure and Applied Geophysics 174, 1855–1874. https://doi.org/10.1007/S00024-017-1534-X/FIGURES/17

Li, M., Zhang, L., Dong, J., Tang, M., Shi, X., Liao, M., Xu, Q., 2019. Characterization of pre- and post-failure displacements of the Huangnibazi landslide in Li County with multi-source satellite observations. Engineering Geology 257, 105140. https://doi.org/10.1016/J.ENGGEO.2019.05.017

Li, Y., Huang, J., Jiang, S.-H., Huang, F., Chang, Z., 2017. A web-based GPS system for displacement monitoring and failure mechanism analysis of reservoir landslide. Scientific Reports 2017 7:1 7, 1–13. https://doi.org/10.1038/s41598-017-17507-7

Lin, C.W., Liu, S.H., Lee, S.Y., Liu, C.C., 2006. Impacts of the Chi-Chi earthquake on subsequent rainfall-induced landslides in central Taiwan. Engineering Geology 86, 87–101. https://doi.org/10.1016/J.ENGGEO.2006.02.010

Liu, Y., Qiu, H., Yang, D., Liu, Z., Ma, S., Pei, Y., Zhang, J., Tang, B., 2022. Deformation responses of landslides to seasonal rainfall based on InSAR and wavelet analysis. Landslides 19, 199–210. https://doi.org/10.1007/S10346-021-01785-4/FIGURES/7

López-Vinielles, J., Fernández-Merodo, J.A., Ezquerro, P., García-Davalillo, J.C., Sarro, R., Reyes-Carmona, C., Barra, A., Navarro, J.A., Krishnakumar, V., Alvioli, M., Herrera, G., 2021. Combining Satellite InSAR, Slope Units and Finite Element Modeling for Stability Analysis in Mining Waste Disposal Areas. Remote Sensing 2021, Vol. 13, Page 2008 13, 2008. https://doi.org/10.3390/RS13102008

Lu, P., Bai, S., Tofani, V., Casagli, N., 2019. Landslides detection through optimized hot spot analysis on persistent scatterers and distributed scatterers. ISPRS Journal of Photogrammetry and Remote Sensing 156, 147–159. https://doi.org/10.1016/j.isprsjprs.2019.08.004

Lu, P., Casagli, N., Catani, F., Tofani, V., 2011. Persistent Scatterers Interferometry Hotspot and Cluster Analysis (PSI-HCA) for detection of extremely slow-moving landslides. http://dx.doi.org/10.1080/01431161.2010.536185 33, 466–489. https://doi.org/10.1080/01431161.2010.536185

Malinowska, A.A., Witkowski, W.T., Hejmanowski, R., Chang, L., van Leijen, F.J., Hanssen, R.F., 2019. Sinkhole occurrence monitoring over shallow abandoned coal mines with satellite-based persistent scatterer interferometry. Engineering Geology 262, 105336. https://doi.org/10.1016/J.ENGGEO.2019.105336

Mancini, F., Grassi, F., Cenni, N., 2021. A Workflow Based on SNAP–StaMPS Open-Source Tools and GNSS Data for PSI-Based Ground Deformation Using Dual-Orbit Sentinel-1 Data: Accuracy Assessment with Error Propagation Analysis. Remote Sensing 2021, Vol. 13, Page 753 13, 753. https://doi.org/10.3390/RS13040753

Manconi, A., 2021. How phase aliasing limits systematic space-borne DInSAR monitoring and failure forecast of alpine landslides. Engineering Geology 287, 106094. https://doi.org/10.1016/J.ENGGEO.2021.106094

Martino, S., Fiorucci, M., Marmoni, G.M., Casaburi, L., Antonielli, B., Mazzanti, P., 2022. Increase in landslide activity after a low-magnitude earthquake as inferred from DInSAR interferometry. Scientific Reports 2022 12:1 12, 1–19. https://doi.org/10.1038/s41598-022-06508-w

Massey, C., Townsend, D., Rathje, E., Allstadt, K.E., Lukovic, B., Kaneko, Y., Bradley, B., Wartman, J., Jibson, R.W., Petley, D.N., Horspool, N., Hamling, I., Carey, J., Cox, S., Davidson, J., Dellow, S., Godt, J.W., Holden, C., Jones, K., Kaiser, A., Little, M., Lyndsell, B., McColl, S., Morgenstern, R., Rengers, F.K., Rhoades, D., Rosser, B., Strong, D., Singeisen, C., Villeneuve, M., 2018a. Landslides Triggered by the 14 November 2016 Mw 7.8 Kaikōura Earthquake, New ZealandLandslides Triggered by the 14 November 2016 Mw 7.8 Kaikōura

Earthquake, New Zealand. Bulletin of the Seismological Society of America 108, 1630–1648. https://doi.org/10.1785/0120170305

Massey, C., Townsend, D., Rathje, E., Allstadt, K.E., Lukovic, B., Kaneko, Y., Bradley, B., Wartman, J., Jibson, R.W., Petley, D.N., Horspool, N., Hamling, I., Carey, J., Cox, S., Davidson, J., Dellow, S., Godt, J.W., Holden, C., Jones, K., Kaiser, A., Little, M., Lyndsell, B., McColl, S., Morgenstern, R., Rengers, F.K., Rhoades, D., Rosser, B., Strong, D., Singeisen, C., Villeneuve, M., 2018b. Landslides Triggered by the 14 November 2016 Mw 7.8 Kaikōura Earthquake, New Zealand. Bulletin of the Seismological Society of America 108, 1630–1648. https://doi.org/10.1785/0120170305

Massey, C.I., Townsend, D.T., Lukovic, B., Morgenstern, R., Jones, K., Rosser, B., de Vilder, S., 2020. Landslides triggered by the MW7.8 14 November 2016 Kaikōura earthquake: an update. Landslides 17, 2401–2408. https://doi.org/10.1007/S10346-020-01439-X/FIGURES/7

McColl, S.T., 2022. Landslide causes and triggers. Landslide Hazards, Risks, and Disasters 13–41. https://doi.org/10.1016/B978-0-12-818464-6.00011-1

Meisina, C., Zucca, F., Fossati, D., Ceriani, M., Allievi, J., 2006. Ground deformation monitoring by using the Permanent Scatterers Technique: The example of the Oltrepo Pavese (Lombardia, Italy). Engineering Geology 88, 240–259. https://doi.org/10.1016/J.ENGGEO.2006.09.010

MINH, D.H.T., Hanssen, R., Rocca, F., 2020. Radar Interferometry: 20 Years of Development in Time Series Techniques and Future Perspectives. Remote Sensing 2020, Vol. 12, Page 1364 12, 1364. https://doi.org/10.3390/RS12091364

Moretto, S., Bozzano, F., Mazzanti, P., 2021. The role of satellite insar for landslide forecasting: Limitations and openings. Remote Sensing 13, 3735. https://doi.org/10.3390/RS13183735/S1

Moss, J.L., 2000. Using the Global Positioning System to monitor dynamic ground deformation networks on potentially active landslides. International Journal of Applied Earth Observation and Geoinformation 2, 24–32. https://doi.org/10.1016/S0303-2434(00)85023-0

Ngunjiri, M.W., Libohova, Z., Owens, P.R., Schulze, D.G., 2020. Landform pattern recognition and classification for predicting soil types of the Uasin Gishu Plateau, Kenya. CATENA 188, 104390. https://doi.org/10.1016/J.CATENA.2019.104390

Notti, D., Herrera, G., Bianchini, S., Meisina, C., García-Davalillo, J.C., Zucca, F., 2014. A methodology for improving landslide PSI data analysis. https://doi.org/10.1080/01431161.2014.889864 35, 2186–2214. https://doi.org/10.1080/01431161.2014.889864

Nowicki Jessee, M.A., Hamburger, M.W., Ferrara, M.R., McLean, A., FitzGerald, C., 2020. A global dataset and model of earthquake-induced landslide fatalities. Landslides 17, 1363–1376. https://doi.org/10.1007/s10346-020-01356-z

Palmer, J., 2017. Creeping catastrophes: Studies of slow landslides could unmask the mechanics of a worldwide scourge. Nature 548, 384–386. https://doi.org/10.1038/548384a

Parker, R.N., Hancox, G.T., Petley, D.N., Massey, C.I., Densmore, A.L., Rosser, N.J., 2015. Spatial distributions of earthquake-induced landslides and hillslope preconditioning in the northwest South Island, New Zealand. Earth Surface Dynamics 3, 501–525. https://doi.org/10.5194/ESURF-3-501-2015

Patton, A.I., Rathburn, S.L., Capps, D.M., 2019. Landslide response to climate change in permafrost regions. Geomorphology 340, 116–128. https://doi.org/10.1016/J.GEOMORPH.2019.04.029

Pawluszek-Filipiak, K., Borkowski, A., Motagh, M., 2021. Multi-temporal landslide activity investigation by spaceborne SAR interferometry: The case study of the Polish Carpathians. Remote Sensing Applications: Society and Environment 24, 100629. https://doi.org/10.1016/J.RSASE.2021.100629

Petley, D., Dunning, S., Rosser, N., Kausar, A.B., 2010. Incipient Landslides in the Jhelum Valley, Pakistan Following the 8th October 2005 Earthquake, in: SAARC Workshop on Landslide Risk Management in South Asia. SAARC Disaster Management Centre, Thimpu, Bhutan, pp. 107–116.

Petricca, P., Bignami, C., Doglioni, C., 2021. The epicentral fingerprint of earthquakes marks the coseismically activated crustal volume. Earth-Science Reviews 218, 103667. https://doi.org/10.1016/J.EARSCIREV.2021.103667

Prats-Iraola, P., Scheiber, R., Marotti, L., Wollstadt, S., Reigber, A., 2012. TOPS interferometry with terraSAR-X. IEEE Transactions on Geoscience and Remote Sensing 50, 3179–3188. https://doi.org/10.1109/TGRS.2011.2178247

Raspini, F., Bianchini, S., Ciampalini, A., del Soldato, M., Solari, L., Novali, F., del Conte, S., Rucci, A., Ferretti, A., Casagli, N., 2018. Continuous, semi-automatic monitoring of ground deformation using Sentinel-1 satellites. Scientific Reports 2018 8:1 8, 1–11. https://doi.org/10.1038/s41598-018-25369-w

Ristau, J., 2008. Implementation of Routine Regional Moment Tensor Analysis in New Zealand. Seismological Research Letters 79, 400–415. https://doi.org/10.1785/GSSRL.79.3.400

Rizzitano, S., Cascone, E., Biondi, G., 2014. Coupling of topographic and stratigraphic effects on seismic response of slopes through 2D linear and equivalent linear analyses. Soil Dynamics and Earthquake Engineering 67, 66–84. https://doi.org/10.1016/J.SOILDYN.2014.09.003

Rosen, P.A., 2000. Synthetic aperture radar interferometry. Proceedings of the IEEE 88, 333–380. https://doi.org/10.1109/5.838084

Rosi, A., Tofani, V., Tanteri, L., Tacconi Stefanelli, C., Agostini, A., Catani, F., Casagli, N., 2018. The new landslide inventory of Tuscany (Italy) updated with PS-InSAR: geomorphological features and landslide distribution. Landslides 15, 5–19. https://doi.org/10.1007/S10346-017-0861-4/FIGURES/14

Rosser, N., Kincey, M., Oven, K., Densmore, A., Robinson, T., Pujara, D.S., Shrestha, R., Smutny, J., Gurung, K., Lama, S., Dhital, M.R., 2021. Changing significance of landslide Hazard and risk after the 2015 Mw 7.8 Gorkha, Nepal Earthquake. Progress in Disaster Science 10, 100159. https://doi.org/10.1016/J.PDISAS.2021.100159

Roy, P., Martha, T.R., Khanna, K., Jain, N., Kumar, K.V., 2022. Time and path prediction of landslides using InSAR and flow model. Remote Sensing of Environment 271, 112899. https://doi.org/10.1016/J.RSE.2022.112899

Royán, M.J., Abellán, A., Jaboyedoff, M., Vilaplana, J.M., Calvet, J., 2013. Spatio-temporal analysis of rockfall pre-failure deformation using Terrestrial LiDAR. Landslides 2013 11:4 11, 697–709. https://doi.org/10.1007/S10346-013-0442-0

Saba, S.B., van der Meijde, M., van der Werff, H., 2010. Spatiotemporal landslide detection for the 2005 Kashmir earthquake region. Geomorphology 124, 17–25. https://doi.org/10.1016/J.GEOMORPH.2010.07.026

Sara, F., Silvia, B., Sandro, M., 2014. Landslide inventory updating by means of Persistent Scatterer Interferometry (PSI): the Setta basin (Italy) case study. http://www.tandfonline.com/action/journalInformation?show=aimsScope&journalCode=tgnh20#.VsXodSCLRhE 6, 419–438. https://doi.org/10.1080/19475705.2013.866985

Schlögel, R., Doubre, C., Malet, J.P., Masson, F., 2015. Landslide deformation monitoring with ALOS/PALSAR imagery: A D-InSAR geomorphological interpretation method. Geomorphology 231, 314–330. https://doi.org/10.1016/J.GEOMORPH.2014.11.031

Shafique, M., 2020. Spatial and temporal evolution of co-seismic landslides after the 2005 Kashmir earthquake. Geomorphology 362, 107228. https://doi.org/10.1016/J.GEOMORPH.2020.107228

Shankar, H., Singh, D., Chauhan, P., 2022. Landslide deformation and temporal prediction of slope failure in Himalayan terrain using PSInSAR and Sentinel-1 data. Advances in Space Research. https://doi.org/10.1016/J.ASR.2022.04.062

Simeoni, L., Mongiovì, L., 2007. Inclinometer Monitoring of the Castelrotto Landslide in Italy. Journal of Geotechnical and Geoenvironmental Engineering 133, 653–666. https://doi.org/10.1061/(ASCE)1090-0241(2007)133:6(653)

Singeisen, C., Massey, C., Wolter, A., Kellett, R., Bloom, C., Stahl, T., Gasston, C., Jones, K., 2022. Mechanisms of rock slope failures triggered by the 2016 Mw 7.8 Kaikōura earthquake and implications for landslide susceptibility. Geomorphology 415, 108386. https://doi.org/10.1016/J.GEOMORPH.2022.108386

Skolnik, M.I., 1962. Introduction to radar systems, 1st edition. ed. McGraw-Hill book company.

Solari, L., Bianchini, S., Franceschini, R., Barra, A., Monserrat, O., Thuegaz, P., Bertolo, D., Crosetto, M., Catani, F., 2020a. Satellite interferometric data for landslide intensity evaluation in mountainous regions. International Journal of Applied Earth Observation and Geoinformation 87, 102028. https://doi.org/10.1016/J.JAG.2019.102028

Solari, L., del Soldato, M., Raspini, F., Barra, A., Bianchini, S., Confuorto, P., Casagli, N., Crosetto, M., 2020b. Review of Satellite Interferometry for Landslide Detection in Italy. Remote Sensing 2020, Vol. 12, Page 1351 12, 1351. https://doi.org/10.3390/RS12081351

Squarzoni, G., Bayer, B., Franceschini, S., Simoni, A., 2020. Pre- and post-failure dynamics of landslides in the Northern Apennines revealed by space-borne synthetic aperture radar interferometry (InSAR). Geomorphology 369, 107353. https://doi.org/10.1016/j.geomorph.2020.107353

Strozzi, T., Luckman, A., Murray, T., Wegmüller, U., Werner, C.L., 2002. Glacier motion estimation using SAR offset-tracking procedures. IEEE Transactions on Geoscience and Remote Sensing 40, 2384–2391. https://doi.org/10.1109/TGRS.2002.805079

Stumpf, A., Malet, J.P., Allemand, P., Pierrot-Deseilligny, M., Skupinski, G., 2015. Ground-based multi-view photogrammetry for the monitoring of landslide deformation and erosion. Geomorphology 231, 130–145. https://doi.org/10.1016/J.GEOMORPH.2014.10.039

Stumpf, A., Malet, J.P., Allemand, P., Ulrich, P., 2014. Surface reconstruction and landslide displacement measurements with Pléiades satellite images. ISPRS Journal of Photogrammetry and Remote Sensing 95, 1–12. https://doi.org/10.1016/j.isprsjprs.2014.05.008

Stumpf, A., Malet, J.P., Delacourt, C., 2017. Correlation of satellite image time-series for the detection and monitoring of slow-moving landslides. Remote Sensing of Environment 189, 40–55. https://doi.org/10.1016/j.rse.2016.11.007

Tang, C., van Westen, C.J., Tanyas, H., Jetten, V.G., 2016. Analysing post-earthquake landslide activity using multi-temporal landslide inventories near the epicentral area of the 2008 Wenchuan earthquake. Natural Hazards and Earth System Sciences 16, 2641–2655. https://doi.org/10.5194/NHESS-16-2641-2016

Tantianuparp, P., Shi, X., Zhang, L., Balz, T., Liao, M., 2013. Characterization of Landslide Deformations in Three Gorges Area Using Multiple InSAR Data Stacks. Remote Sensing 2013, Vol. 5, Pages 2704-2719 5, 2704–2719. https://doi.org/10.3390/RS5062704

Tanyaş, H., Görüm, T., Fadel, I., Yıldırım, C., Lombardo, L., 2022. An open dataset for landslides triggered by the 2016 Mw 7.8 Kaikōura earthquake, New Zealand. Landslides 2022 19:6 19, 1405–1420. https://doi.org/10.1007/S10346-022-01869-9

Tanyaş, H., Kirschbaum, D., Görüm, T., van Westen, C.J., Lombardo, L., 2021a. New Insight into Post-seismic Landslide Evolution Processes in the Tropics. Frontiers in Earth Science 9, 551. https://doi.org/10.3389/FEART.2021.700546/BIBTEX

Tanyaş, H., Kirschbaum, D., Görüm, T., van Westen, C.J., Tang, C., Lombardo, L., 2021b. A closer look at factors governing landslide recovery time in post-seismic periods. Geomorphology 391, 107912. https://doi.org/10.1016/J.GEOMORPH.2021.107912

Tanyaş, H., Lombardo, L., 2019. Variation in landslide-affected area under the control of ground motion and topography. Engineering Geology 260, 105229. https://doi.org/10.1016/J.ENGGEO.2019.105229

Tanyaş, H., van Westen, C.J., Allstadt, K.E., Anna Nowicki Jessee, M., Görüm, T., Jibson, R.W., Godt, J.W., Sato, H.P., Schmitt, R.G., Marc, O., Hovius, N., 2017. Presentation and Analysis of a Worldwide Database of Earthquake-Induced Landslide Inventories. Journal of Geophysical Research: Earth Surface 122, 1991–2015. https://doi.org/10.1002/2017JF004236

Teshebaeva, K., Echtler, H., Bookhagen, B., Strecker, M., 2019. Deep-seated gravitational slope deformation (DSGSD) and slow-moving landslides in the southern Tien Shan Mountains: new insights from InSAR, tectonic and geomorphic analysis. Earth Surface Processes and Landforms 44, 2333–2348. https://doi.org/10.1002/ESP.4648

Tofani, V., Ventisette, C. del, Moretti, S., Casagli, N., 2014. Integration of Remote Sensing Techniques for Intensity Zonation within a Landslide Area: A Case Study in the Northern Apennines, Italy. Remote Sensing 2014, Vol. 6, Pages 907-924 6, 907–924. https://doi.org/10.3390/RS6020907

Ulrich, T., Gabriel, A.A., Ampuero, J.P., Xu, W., 2019. Dynamic viability of the 2016 Mw 7.8 Kaikōura earthquake cascade on weak crustal faults. Nature Communications 2019 10:1 10, 1–16. https://doi.org/10.1038/s41467-019-09125-w van Natijne, A.L., Bogaard, T.A., van Leijen, F.J., Hanssen, R.F., Lindenbergh, R.C., 2022. World-wide InSAR sensitivity index for landslide deformation tracking. International Journal of Applied Earth Observation and Geoinformation 111, 102829. https://doi.org/10.1016/J.JAG.2022.102829

Vermeer, J.L., Quigley, M.C., Duffy, B.G., Langridge, R.M., Pettinga, J.R., 2021. Structure and kinematics of active faulting in the Hope-Kelly and Alpine Fault intersection zone, South Island, New Zealand. Tectonophysics 813, 228928. https://doi.org/10.1016/J.TECTO.2021.228928

Wang, L ;, Qiu, H ;, Zhou, W ;, Zhu, Y ;, Liu, Z ;, Ma, S ;, Yang, D ;, Wang, Luyao, Qiu, Haijun, Zhou, Wenqi, Zhu, Yaru, Liu, Zijing, Ma, Shuyue, Yang, Dongdong, Tang, B., 2022. The Post-Failure Spatiotemporal Deformation of Certain Translational Landslides May Follow the Pre-Failure Pattern. Remote Sensing 2022, Vol. 14, Page 2333 14, 2333. https://doi.org/10.3390/RS14102333

Wang, T., Wei, S., Shi, X., Qiu, Q., Li, L., Peng, D., Weldon, R.J., Barbot, S., 2018. The 2016 Kaikōura earthquake: Simultaneous rupture of the subduction interface and overlying faults. Earth and Planetary Science Letters 482, 44–51. https://doi.org/10.1016/J.EPSL.2017.10.056

Wang, X., Mao, H., 2022. Spatio-temporal evolution of post-seismic landslides and debris flows: 2017 M s 7.0 Jiuzhaigou earthquake. Environmental Science and Pollution Research 29, 15681–15702. https://doi.org/10.1007/S11356-021-16789-9/TABLES/5

Wasowski, J., Bovenga, F., 2014a. Investigating landslides and unstable slopes with satellite Multi Temporal Interferometry: Current issues and future perspectives. Engineering Geology. https://doi.org/10.1016/j.enggeo.2014.03.003

Wasowski, J., Bovenga, F., 2014b. Investigating landslides and unstable slopes with satellite Multi Temporal Interferometry: Current issues and future perspectives. Engineering Geology. https://doi.org/10.1016/j.enggeo.2014.03.003

Werner, C., Wegmüller, U., Strozzi, T., Wiesmann, A., 2003. Interferometric Point Target Analysis for Deformation Mapping. International Geoscience and Remote Sensing Symposium (IGARSS) 7, 4362–4364. https://doi.org/10.1109/IGARSS.2003.1295516

Wright, T.J., Parsons, B.E., Lu, Z., 2004. Toward mapping surface deformation in three dimensions using InSAR. Geophysical Research Letters 31, 1607. https://doi.org/10.1029/2003GL018827

Xia, Z., Motagh, M., Li, T., Roessner, S., 2022. The June 2020 Aniangzhai landslide in Sichuan Province, Southwest China: slope instability analysis from radar and optical satellite remote sensing data. Landslides 19, 313–329. https://doi.org/10.1007/S10346-021-01777-4/FIGURES/12

Xiong, Z., Feng, G., Feng, Z., Miao, L., Wang, Y., Yang, D., Luo, S., 2020. Pre- and post-failure spatial-temporal deformation pattern of the Baige landslide retrieved from multiple radar and optical satellite images. Engineering Geology 279, 105880. https://doi.org/10.1016/J.ENGGEO.2020.105880

Xu, Y., Schulz, W.H., Lu, Z., Kim, J., Baxtrom, K., 2021. Geologic controls of slow-moving landslides near the US West Coast. Landslides 18, 3353–3365. https://doi.org/10.1007/S10346-021-01732-3/FIGURES/8

Yang, W., Qi, W., Wang, M., Zhang, J., Zhang, Y., 2017. Spatial and temporal analyses of post-seismic landslide changes near the epicentre of the Wenchuan earthquake. Geomorphology 276, 8–15. https://doi.org/10.1016/J.GEOMORPH.2016.10.010

Yi, Z., Xingmin, M., Allesandro, N., Tom, D., Guan, C., Colm, J., Yuanxi, L., Xiaojun, S., 2022. Characterization of pre-failure deformation and evolution of a large earthflow using InSAR monitoring and optical image interpretation. Landslides 19, 35–50. https://doi.org/10.1007/S10346-021-01744-Z/FIGURES/13

Zebker, H.A., Villasenor, J., 1992. Decorrelation in interferometric radar echoes. IEEE Transactions on Geoscience and Remote Sensing 30, 950–959. https://doi.org/10.1109/36.175330

Zhao, C., Kang, Y., Zhang, Q., Lu, Z., Li, B., 2018. Landslide Identification and Monitoring along the Jinsha River Catchment (Wudongde Reservoir Area), China, Using the InSAR Method. Remote Sensing 2018, Vol. 10, Page 993 10, 993. https://doi.org/10.3390/RS10070993